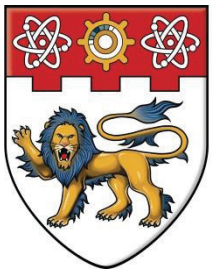

NANYANG TECHNOLOGICAL UNIVERSITY

# DEVELOPMENT OF MICROFORMING FRICTION TEST AND STUDY OF FRICTION SIZE-EFFECT DURING MICROFORMING


MUHAMMAD TAUREZA

SCHOOL OF MECHANICAL AND AEROSPACE ENGINEERING


2013

# DEVELOPMENT OF MICROFORMING FRICTION TEST AND STUDY OF FRICTION SIZE-EFFECT DURING MICROFORMING

**MUHAMMAD TAUREZA**

School of Mechanical and Aerospace Engineering

A thesis submitted to the Nanyang Technological University
in partial fulfilment of the requirement for the degree of
Doctor of Philosophy

**2013**

**Summary**

In metal forming, lubrication and the quality of the surface finish of the tooling are carefully designed in order to control the friction. Generally, high friction in metal forming should be avoided as it results in excessive tool wear, elevated process load requirement and damaged product. However, studies have shown that due to the reduced size in microforming setup, there is a shift in friction behaviour, called the friction size-effect. Because of this shift, the knowledge of friction in metal forming such as the typical friction coefficient for certain material pairs and performance of lubricants is not applicable to microforming.

Friction size-effect is therefore chosen as the core of the current studies. The investigation on friction in microforming has been conducted in the past using generic friction tests commonly known for conventional size metal forming. Realizing that fabrication and handling of micro-specimens is a difficult, time-consuming yet integral aspect in performing conventional metal forming friction test, a microforming-specific T-Shape test (or microforming T-Shape test) was developed and is presented as the key contribution of this thesis. This friction test was designed for ease of use with micro-specimens yet still offers great flexibility in allowing lubricant or certain surface finish to be evaluated.

Using the modified T-Shape test, the performance of various lubricants were characterised in order to fully appraise the performance of the test and it was concluded that there is a microforming-specific phenomenon of the loss of lubricant effectiveness. In general, when a liquid or a stable liquid-based lubricant is used in microforming, its efficacy of reducing friction ceases when the contact pressure exceeds a certain value. This limit of lubricant effectiveness was further proposed as

an addendum to the lubricant pocket explanation and this lubricant effectiveness limit can be used in determining the performance of lubricants.

Moreover, experiments using copper have shown that the loss of lubricant effectiveness can deteriorate and as a result, lubricants may not produce friction reduction at all. In order to address this problem, tribological surface textures were considered as a non-traditional friction control solution for microforming. Past studies on surface textures have only covered their use for low pressure contact and no clear description of the friction-reducing mechanism has been given. This thesis presents the current state in the simulation work of integrating tribological surface textures to a microforming process and its effectiveness in reducing overall friction without the use of lubricant. The focus of the simulation work is given to high pressure use which is characteristic of metal forming process.

Ultimately, past experimental results on indentation size effect (ISE) is also discussed in this thesis and is reconstructed into a Depth-dependent Stress-Strain relation (DSS) to explain the shift in material flow behaviour in microforming as well as to propose a simulation approach to incorporate the concept of material length scale without the numerical complexity of having gradient dependent simulation.

**Keywords**: Friction test; Microforming; Size-effect; Strain gradient; Surface texture.

**Acknowledgement**

I would like to particularly mention the following people and their contributions to the completion of this thesis:

- Dr Sylvie Castagne, my university supervisor of this course of Ph.D. for the great attention to details to point out all the imperfections of every work produced so far and for challenging me to always be better throughout the course of the research.
- Co-supervisor from SIMTech Dr Xu Song for the exchange of ideas on some engineering solutions related to the research and for his spirited can do attitude. Dr Xu Song has been a terrific supervisor and career coach to me.
- Former co-supervisors Dr Chao Voon Samuel Lim of Monash University and Dr Yingyot Aue-u-lan of TGGS Bangkok for the insights on many invaluable discussions.

I would also like to sincerely thank family members for their morale support, my parents Zainul Arifin Djajaputra and Setyatik Sholihah, my brother Rizky Delfianto, my wife Nirma Octania Aryanty for the encouragement and comfort, fellow and former fellow students in NTU especially Muhammad Jamil, Chathura Withanage, Jiao Lishi, Lin Danping, and Liu Dan for making work a bit more cheerful, as well as other countless colleagues in NTU and SIMTech. I wish you all the best in your future endeavours.

## Table of Contents

## List of Figures

## List of Tables

## Acronyms and Notations

| Acronym | Definition |
|---|---|
| FE | Finite element |
| DSS | Depth-dependent stress-strain (relation) |
| ISE | Indentation size effect |
| **Notation** | **Definition** |
| $b$ | Burgers vector |
| $C_{1...3}$ | Constants related to microforming T-Shape calibration curves |
| $d$ | Grain size |
| $d_c$ | Contact diameter (indentation) |
| $D$ | Ball diameter (indentation) |
| $f$ | Flange height of workpiece (T-Shape test) |
| $f(m)$ | Function related to microforming T-Shape calibration curves |
| $f_{pz}$ | Coefficient related to plastic zone growth |
| $F_s$ | Friction force |
| $G$ | Shear modulus |
| $h$ | Indentation depth |
| $h^*$ | Constant related to material length scale |
| $H$ | Hardness (at particular depth) |
| $H_0$ | Hardness (bulk) |
| $k$ | Shear strength (Yield stress at pure shear) |
| $k_{HP}$ | Hall-Petch strengthening coefficient |
| $m$ | Constant friction factor |

| | |
|---|---|
| $N$ | Normal force |
| $p$ | Normal pressure |
| $PI$ | Performance Index (T-Shape test) |
| $P_{trans}$ | Limit pressure of lubricant effectiveness |
| $t$ | Total height at mid-length of workpiece (T-Shape test) |
| $T$ | Temperature |
| $Y$ | Threshold hardness |
| $\alpha_{RC}$ | Fraction of real contact area |
| $\alpha_T$ | Taylor coefficient |
| $\beta$ | Coefficient related to dislocation coupling |
| $\delta$ | Total height difference in microforming T-Shape test |
| $\delta_0$ | Total height difference in original T-Shape test |
| $\varepsilon$ | Strain |
| $\dot{\varepsilon}$ | Strain rate |
| $\mu$ | Coulomb friction coefficient |
| $\mu_{WB}$ | General friction coefficient |
| $\rho_G$ | Geometrically necessary dislocation density |
| $\rho_S$ | Statistically stored dislocation density |
| $\sigma$ | Stress |
| $\sigma_y$ | Yield stress (uniaxial) |
| $\sigma_0$ | Starting stress for dislocation movement |
| $\tau$ | Friction stress |
| $\tau_0$ | Material friction stress |

# CHAPTER 1 INTRODUCTION

## 1.1 Background

Along with technological development in non-intrusive surgical equipment, precision tools, electronics and IT, there is increasing demand to produce small components in large volumes. For metallic parts, this demand used to be catered by micro-machining and MEMS based processes of lithography. However, the manufacturing of these small parts has been gradually taken over by metal forming processes as these processes are cheaper, capable of producing better quality products (better mechanical properties) and have higher production rate.

In sub-millimetre regime, phenomena called the size-effects may occur in metal forming. Size effect is defined by the changes in materials and process behaviour owing to the change in parts size. Due to these size effects, the knowledge from the conventional metal forming cannot be directly applied to sub-millimetre metal forming, referred to as microforming [1]. As a result, there has been massive research and development going on in the field of microforming. Figure 1 presents a selection of typical components targeted by microforming.

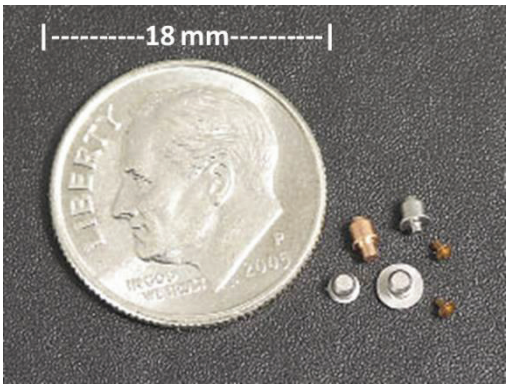


Figure 1: Example of products produced by microforming

Some of these size effects include changes in metal flow when the flow path size becomes comparable to the grain size, changes in process load requirement, as well as changes in friction [1-5]. Based on these findings, models such as lubricant pockets and surface grains are proposed.

In metal forming, excessive friction can impair the product (fracture and poor surface finish), worsen tool wear and increase process load tremendously. Therefore, lubricant is generally used. However, in microforming, the use of lubricant is not economically effective because of the large surface area and the difficulty of cleaning the lubricant in the tiny features of the tool. Moreover, studies in lubricated microforming [3, 5] show the trend of increasing friction as the part size reduces.

Understanding that there are plenty of factors affecting friction in metal forming, vast studies are needed in order to better understand their influence to friction in microforming. However, microforming friction investigations in the past have used friction test apparatus which were originally designed for conventional size metal forming. These apparatus were not good enough for the current study as they are not suitable for use in microforming. Therefore, there is a need to design a new friction test setup specifically for use in microforming which allows for closer investigation.

Lastly, following recent restrictions in Europe and Japan with regards to the use of lubricant as potentially hazardous substances [6], the research in metal forming started to look into the possibility to (a) eliminate hazardous chemicals from lubricants, and (b) reduction of waste (e.g. reducing tool wear, using minimal quantity lubrication and reusing lubricant). However, as the lubrication effectiveness is reduced in microforming, a more drastic approach of tribological surface texturing becomes much more important. Even though the improvement resulted by tribological surface

texturing has been abundantly reported, there has not been clear conclusion of the true behaviour when surface textures are introduced or which textures should be introduced to minimize friction. Also, it was noted with great importance that the application of tribological surface textures so far is limited to low pressure contact to reduce wear and tear between repetitively moving parts whereas the application for high pressure contact such as for bulk metal forming tooling has not been explored.

Investigations on surface textures as friction control and on friction in general have been done mainly using experiments. Although experiments are excellent in producing data for processes, experiments on friction are unable to adequately explain the role of surface textures during contact because friction in nature is a convolution of many physical phenomena, e.g. adhesion, asperity ploughing.

The use of Finite Element (FE) simulation is able to provide prediction and explanation on friction and more importantly it allows the dissection of the physical phenomena contributing to friction. Hence, the modelling of microforming friction behaviour was identified as another section in this study in which significant contribution can be made to the field of microforming and metal forming in general. Specifically, FE will be used to explain the mechanisms of friction control using surface textures and explore the influence of strain gradient on friction.

## 1.2 Objectives and Scope of the Work

This Ph.D. research aims to develop a friction testing apparatus designed specifically for microforming and to investigate the friction size-effect occurring in microforming. In order to achieve these goals, the following scope of work was outlined:

a. Design of a friction test which is representative of a typical metal forming process for investigation of microforming behaviour which fulfil a set of criteria for use in microforming research and can also be adopted by the industries.
b. Investigation on the effect of using select types of lubricants and the corresponding friction behaviour during friction test in the aim to examine the lubrication behaviour as well as appraise the newly developed microforming friction test design.
c. Investigation on the effects of introducing tribological surface textures for high pressure contact through FE simulation and experimental validation.
d. Introduction of the concept of material length scale in FE simulation to examine the behaviour attributed to strain gradient as have been observed through previous studies without having to fully perform gradient dependent or crystal plasticity simulation.

## 1.3 Organization of the Thesis

The thesis begins with the statements of motivation and objectives for the study. Chapter 2 of this thesis presents the state-of-the-art understanding on microforming, the size effects documented in microforming and their possible sources, as well as general information on friction and differentiation between friction models. It also elaborates on past results on tribological surface textures which can be categorised as pore (circular) textures, groove textures and directionally ground surfaces. The research gaps in which this study aims to fulfil is also stated in Chapter 2. Chapter 3 presents the experiment and simulation methods related to the study. Chapter 4 presents the results on the development of the new friction test for microforming as well as the results on friction investigations involving solid, liquid and drying

lubricants. Chapter 5 presents FE simulation results related to the use of surface textures in microforming. Chapter 6 proposes the depth-dependent stress-strain (DSS) simulation approach which is an alternative to gradient dependent or crystal plasticity simulation which can be used in microforming simulation. More specific review on past investigations which are critical in achieving the objectives of the Ph.D. is presented in the individual result chapters (i.e. Chapter 4 through Chapter 6). This thesis subsequently finishes with conclusion of the study, the summary of achievements of the study, and recommendations on possible future works.

# CHAPTER 2 LITERATURE REVIEW

## 2.1 Metal Forming and Microforming

### *2.1.1 Metal forming*

Metallic materials are largely used in structural applications as they have excellent mechanical properties. Metallic components may be required to have certain shape, size, tolerance and properties, and hence the problem of designing suitable manufacturing plan has to be taken very seriously.

Many manufacturing processes have been developed to produce metallic components and assemblies. Altan et al. [7] explained the role of metal forming among manufacturing processes as follows:

1. Primary shaping processes to cast processable geometry from molten state. These processes generally create ingots from impure incoming materials.
2. Metal forming processes to produce near net shapes or even net shapes from the primary shapes by means of plastic deformation.
3. Machining processes to produce net shapes by means of material removal.
4. Metal treatment processes such as heat treatment and surface hardening. These processes do not change the shape of the parts, but only change the appearance and/or the properties.
5. Joining processes, which include metallurgical joining such as welding, as well as mechanical joining using mechanical fasteners.

In order to produce the net shapes, metal forming is preferred because of the high throughput, excellent tolerance, and superior mechanical properties (from strain

hardening) [8]. However, metal forming is not suitable for small batch production as the machine investment (press and moulds) is higher. Metal forming processes are usually designed with CAD/CAM [9, 10] with the help from FE code such as Deform 2D and 3D [11-14] and their mould production generally involves machining to shape (with oversize specified), heat treatment and finishing with electro-discharge machining [15] or high speed machining [16] to the precise dimensions especially for complex geometry. These multi-step process results in expensive mould cost.

Metal forming processes are divided into two broad categories:

1. Bulk (or massive) metal forming, which are characterized by the large plastic deformation, resulting in significant change of shape from the stock shape to the end result. In bulk metal forming, the plastic (permanent) deformation is much larger than the elastic deformation. Hence, the elastic recovery after the process is negligible. Bulk metal forming processes include forging and extrusion.

2. Sheet metal forming, which are characterized by the workpiece in sheet form. In addition, sheet metal forming processes generally preserve the cross section of the sheet, i.e. severe thinning is sometimes expected but generally undesirable, and in contrast to bulk metal forming, the amount of elastic deformation is significant and elastic recovery (springback) is usually expected. Sheet metal forming processes include bending and deep drawing.

Due to limited ductility of certain materials, metal forming may not be able to produce net shapes directly from the primary shapes such as bars and sheets. To alleviate this problem, metal forming can use what is termed by “preform,” i.e. a near

net shape part with suitable material distribution. This preform can be produced from another metal forming process.

Jeswiet et al. [17] provides an overview of metal forming researches up to the year 2008.

### *2.1.2 Microforming and size effects*

Since the 1990s, the trend of producing smaller metallic components started to appear with the introduction of smaller and feature packed gadgets and minimally-intrusive surgical robotics tools. These components started to be manufactured through precision machining and MEMS-based processes such as photolithography. At the present, industries such as IT, technological hardware and process automation for micro-processes have benefited from the development of miniaturization techniques. Increasing demand over the years has sparked the interest for this production to be taken over by metal forming. However, as discovered in studies at smaller size [1, 4], metal forming experiments show changing behaviour which is attributed to the size of the setup, called the "size effects". These changing behaviours are not directly attributed to physical or chemical mechanisms which occur only in miniaturized processes. Instead, they are attributed to mechanisms which can be considered *negligible* in conventional processes [18]. The term "microforming" was then defined as a field of research on metal forming when the parts have at least two dimensions less than one millimetre [1] and the negligible mechanisms become significant. It should not be confused with the state-of-the-art of nanoforming in which material flow is studied to accurately produce extremely small surface features (hallmark or symbols) on very small surfaces [19]. The state-of-the-art in microforming has been reviewed by Fu and Chan [20].

#### *2.1.2.1 Janssen's classification of size effects*

Janssen [21], based on uniaxial straining of thin sheets, generally categorized size effects as follows:

1. *Microstructural effects*. Deformation in metals at low temperature (e.g. room temperature) is mainly attributed to dislocation creep [22]. In general, the dislocation movement allows material to be microscopically (and subsequently macroscopically) deformed. While dislocations can move consistently as long as it overcomes the energy required within one crystal structure, or a grain, this dislocation movement is hindered when there is grain boundary. In general, the proportion of grain boundary inside the material, or in other word the smaller the individual grains, the higher the energy needed to create further deformation. This is known as the Hall-Petch effect which is observed for flow stress [23]. In Equation 1.1, $\sigma_y$ and $d$ denote yield stress and average grain size, respectively, and $k_{HP}$ is the strengthening coefficient which can be either a constant [22] or a function [24]. However, there is a limit for this grain boundary strengthening. The smaller the grains, the larger the proportion of the grain boundary and hence the more atoms are at these grain boundaries. This occurs generally when the grain size is in the nanometres. The proportionally large number of atoms at the boundary allows sliding of atoms not inside the grain (or dislocation creep) but outside the grain allowing sliding between *atomic planes.* This alternate deformation mechanism was further called grain boundary sliding which further softens the material with decreasing grain size [25, 26] or also called the inverse Hall-Petch effect. Various other microstructural- and physical-based material model involving grain size have been summarized by Bariani et al. [27]. Not only

does it influence the property of the material, grain size also influences the possible surface finish of the product. The effect of *orange peel* has been observed in conventional size metal forming when using coarse grain material. Orange peel is the uneven finish associated with the grains at the surface having anisotropic property and the effect is even stronger when the components become smaller.

$$\sigma_y = \sigma_0 + \frac{k_{HP}}{\sqrt{d}} \quad 1.1$$

2. *Grain statistics effect*. Metal consists of crystals or grains which individually are anisotropic (they produce different response to load depending on the loading direction). However, the grains inside a component can have different orientations from one another, and for example in large cast components, the overall mechanical properties can be isotropic as the different grain orientations negate each other. As smaller components consist of smaller number of grains, statistically they are more prone to anisotropy. Consequently, when experimenting with very small components, frequently it is not always possible to assume the component as having homogeneous and isotropic properties and as a result, there have been works in the field of simulation to consider the properties of the grains individually, or crystal plasticity FE simulation [26, 28, 29].

3. *Strain gradient effect*. The example of this effect is the microbend test by Stölken and Evans [30] during which it was found that on thinner foil, the required normalized bending moment is larger in order to produce the same strain level. This effect is caused by the lattice curvature and may act as noise during mechanical test. The development in gradient dependent plasticity simulation has strived to understand and predict the effect of this strain gradient using FE

simulation [31, 32]. Janssen et al. suggested that strain gradient effect can be avoided by having homogeneous deformation throughout the workpiece during the mechanical test [21]. However, as non-homogeneous deformation is always expected in metal forming, this strain gradient effect has to be considered in designing microforming process.

4. *Boundary effects*. Surface grains are generally softer in comparison to grains located farther inside the material (or bulk grains) [1]. The smaller the specimen, the fewer grains there are across the dimensions and consequently, the properties of the surface grains become more important. In other word, smaller specimens have larger proportion of softer surface grains which, in turn, reduces their overall flow stress [21, 33, 34].

5. *Geometrical effects*. It was discovered that the geometry of the cross section in uniaxial straining influences the flow stress. In the examination, two specimens with the same cross sectional area but different shapes (circular and rectangular) were tested. Although the drop in flow stress is also observed in accordance to boundary size effect, the critical number of grains across the dimension is not the same for the two specimens [35]. However, this geometrical effect can be seen as a boundary size effect as the circular and rectangular cross sections have different surface to bulk grain ratio.

Janssen et al. [21] considered the case of tensile testing and therefore emphasized on the material properties, but not the contact behaviour between the material tested and the tooling.

#### *2.1.2.2 Vollertsen's classification of size effects (2006)*

From the perspective of microforming, Vollertsen [36] reviewed that size effects can be attributed to the following sources:

1. *Pure volume effects*. Smaller volume translates to fewer defects, generally in the form of dislocations. As source of new dislocation (Frank – Read source) is limited by the volume of the workpiece, the deformation behaviour may also be affected by the decrease in size.

2. *Ratio of surface area to volume (S/V) effects*. Given the same shape (a cube for example), the S/V is higher in smaller components. The change in S/V influences processes which are dominated by surface effects such as heating and cooling. When the edges of the cube are halved, its volume becomes 1/8 of the original and its surface area becomes 1/4 of the original. This results in faster temperature raise and drop in smaller component. This can also be related to Janssen's boundary size effect [21] as the change of S/V ratio also changes the proportion of surface and bulk grains.

3. *Forces relation size effect*. Forces acting between workpiece and tooling may play more important role in the processes. In conventional metal forming, these forces (e.g. surface tension using lubricant) may be small compared to the process load. As process load reduces, the importance of these peripheral forces may elevate. This can influence the design of microforming setup such as the requirement for auxiliary tooling to handle the workpiece as the surface tension between the tool, the workpiece and the lubricant becomes large enough to create unwanted movement of workpiece during process.

4. *Grain size to dimension effects* (see Figure 2). In order to perfectly scale down a process, for example as the specimen size is scaled by a factor λ, the grain size should also be scaled by a factor λ. Scaling the grain size is not always possible (because the fabrication of fine- and nano-grained material is expensive) and is not always desirable (because changing grain size will drastically influence property of the final product).

5. *Surface roughness to dimension effects*. Similarly, an ideal miniaturization by a factor λ should be accompanied with reducing the surface roughness by the factor λ. However, there is always an issue regarding surface structure scalability (SSS) issue hindering ideal miniaturization [36]. This can manifest as the change in distribution of contacting asperities and subsequently friction.

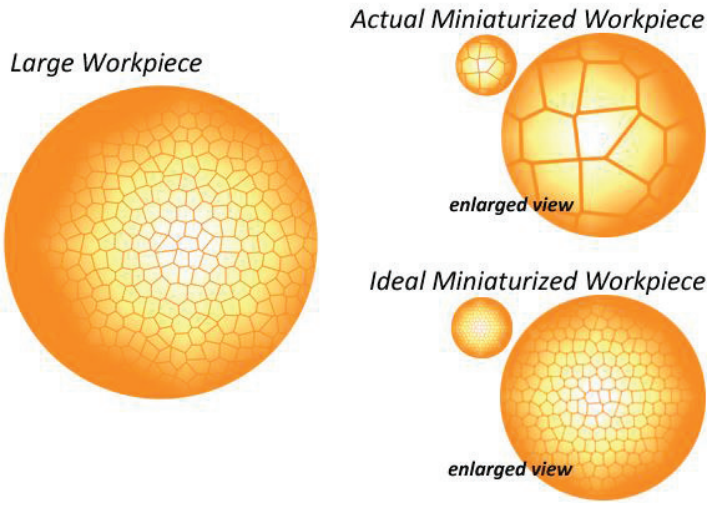


Figure 2: Ideal and actual miniaturization

### *2.1.2.3 Vollertsen's classification of size effects (2008)*

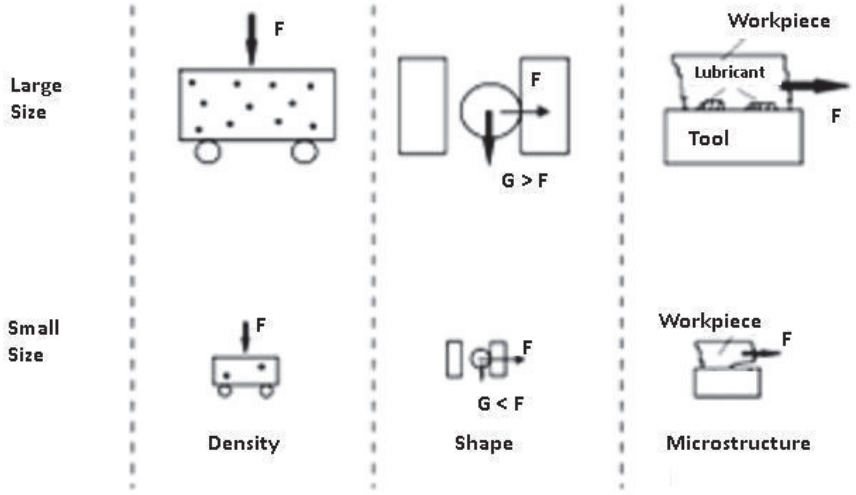


Figure 3: Categories of size effects [37]

A more recent and general term of categories of size effects was introduced by differentiating **density effect** (such as defect density variation from specimen to specimen), **shape effect** (volume of a part is proportional to the third power of its size, and surface area is only proportional to the second power), and the **structure effect** (such as inability to scale grain size by the same factor as the part size) [37]. Figure 3 illustrates these three effects in relation to behaviour in downscaled setup.

### *2.1.2.4 New size effect classification*

In order to summarize the sources of size effects, the following classes of sources of size effects was introduced in this thesis:

1. *Material sources*, which include the microstructural effects such as the grain size and hence the proportion of grain boundary, the ability to produce new

dislocations, etc. This class of sources takes effect irrespective of the size of the component.

2. *Miniaturization sources*, which include the effects attributed to non-conventional scaling such as the number of grain size across the dimension and the comparison between the component size and the surface roughness. This class of sources does not exist if the miniaturization is ideal (see Figure 2). Results from Fu and co-workers [38, 39] suggested that even when the grain size is changed, as long as proportion of grains and grain boundaries is kept constant in the case of ideal miniaturization, material property size effect would not occur.

3. *Size sources*, which include the relation of the components during the process with the equipment such as the increasing effect of lubricant surface tension. This class of source becomes stronger with miniaturization regardless of whether the miniaturization is ideal.

#### *2.1.2.5 Size effects observed in microforming*

These size effects in microforming experiments are investigated by Geiger et al. [1, 3, 4] and all were derived from miniaturization sources, and the various studies generally showed that:

1. *Flow stress is reduced with downscaling (open die forming).*

The reduced flow stress was explained by the theory of surface layer model. The grains located at the surface during upsetting are less restricted compared to the grains located deeper inside the material. These surface grains exhibit less hardening and resistance during deformation thus having lower flow stress. The few layers of grains located near the surface can be considered as surface grains, the rest being bulk

grains. As the microstructure remains relatively the same during the miniaturization, the proportion of surface grains increases as the specimen size gets smaller. With the lowering flow stress, the process load requirement gets smaller (relative to the setup size) as the specimen size is reduced for processes with free surface. However, while this effect applies in open die forming, results on micro-extrusion (closed die forming) showed that in miniaturized process, the shear deformation from the friction can intrude inside the component, creating higher strain (and hence hardening) in the centre of the component [40], increasing flow stress. For process prediction, simulation model has also been developed to include the surface layer model [39]. On the other hand, Wang et al. has developed a coupled surface layer model in which the surface grains were divided into two parts, free surface grains and constraint surface grains [41] as illustrated in Figure 4. In Figure 4, t/d represents the number of grains across the part size or thickness, with t and d denote part thickness and grain size, respectively. The coupled surface layer model proposes that there are counter-acting mechanisms and as a result, the material size effect is highly dependent on the deformation geometry.

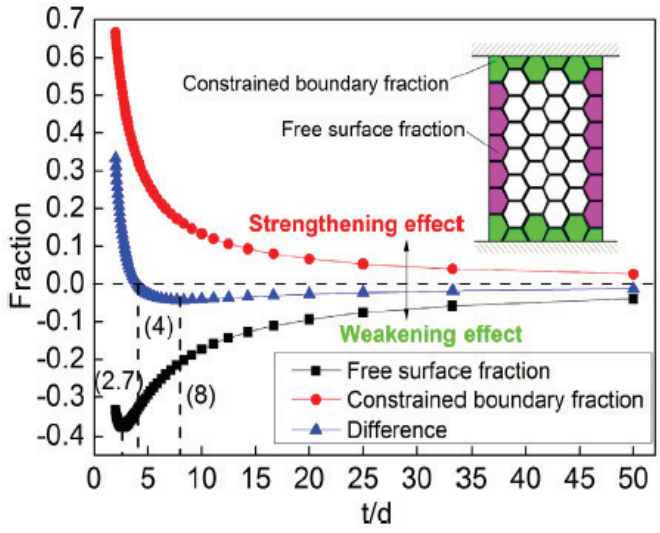


Figure 4: Coupled surface layer model [41]

2. *Process scatter increases with downscaling.*

As smaller specimen consists of fewer grains across the dimensions, the orientation of the individual grains becomes more influential as the number of grains is not enough to provide homogeneity in the material. Anisotropy from specimen to specimen translates to process scatter, i.e. the same process parameter may yield different behaviour depending on how the grains in any given specimen are distributed. In order to reduce the scatter, one possible way is to raise the processing temperature to activate more slip system.

Different findings were found regarding the effect of warm forming to the process scatter. On titanium alloy, it was found that elevated temperature enables better formability, but has no effect on the process scatter in microforming titanium [42]. However, other researches revealed that elevated temperature reduces process scatter to a statistically significant extent [43, 44].

3. *Friction increases with downscaling.*

This increase in friction can be explained using the theory mechanical-rheological model of lubricant pockets. Contact surface can be divided into three distinct areas: real contact area, closed lubricant pockets, and open lubricant pockets (Figure 5). The equivalent representation of surfaces using closed and open voids has also been introduced [45].

Surface roughness in the specimen can be illustrated with asperities, and the distribution of asperities can be considered as *roughness peaks and valleys*. Assuming similar surface roughness, specimen with smaller size would have less roughness peaks and valleys. In lubricated contact, a roughness valley bounded by roughness

peaks holds the lubricant in place, thus the load is shared between the roughness peaks and the pressurized lubricant, lowering the friction. This is called closed lubricant pocket (CLP).

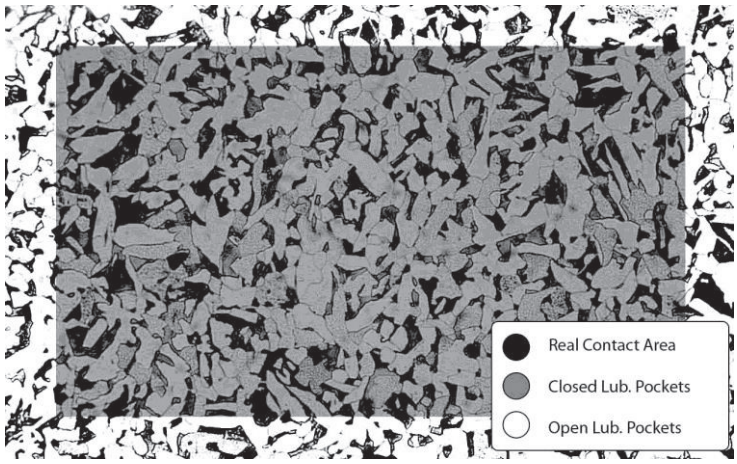


Figure 5: Illustration of typical workpiece contact

In contrast, when the roughness valley is not completely surrounded by roughness peaks, the lubricant leaks out during loading, creating relatively higher friction. This is called open lubricant pocket (OLP) and is usually located near the edge of the contact area. Roughness valleys near the edges of the contact area are less likely to be completely surrounded by roughness peaks. Hence, as the specimen becomes smaller, the ratio of OLP/CLP becomes higher, thus the friction is increased. Another explanation for the ineffectiveness of lubricant is explained by Baek et al. [46] that the feature size in microformed part is within the same scale as the lubricant thickness. Baek et al. [46] further suggested that the lubricant effectiveness can be retained if the natural lubricant thickness is reduced with the example of using self-assembled monolayers (SAM) and solid lubricants (Teflon, diamond-like carbon (DLC)). Recent works by Hu et al. and Wang et al. confirmed the effectiveness on

using DLC to reduce friction in microforming through micro deep drawing experiment [47] and strip drawing [48].

According to the work by Geiger et al. [1] with double cup extrusion test as shown in Figure 6, the lowest friction observed was achieved with the largest workpiece (4 mm diameter) which corresponds to friction factor (*m*, to be discussed later) value of 0.02. This value of friction factor is higher for smaller workpiece which agrees with the lubricant pocket model. However, as it is noted from the same work, when workpiece of 1 mm is used in the experiment, the observed friction factor is not constant with relative stroke. There is a significant increase of observed friction factor, *m*, from approximately 0.14 when the workpiece was subjected to 30% relative stroke, to approximately 0.3 when the relative stroke reaches 80%. This suggests an additional explanation to the lubricant pocket model.

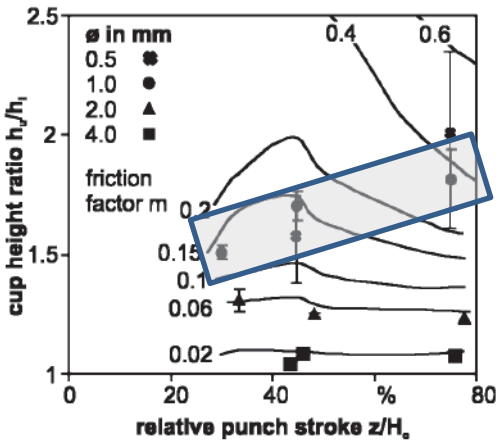


Figure 6: Friction increase with miniaturization [1]

4. *Grain orientation effect increases with downscaling.*

In bulk metal forming, the metal flow is largely influenced by the friction condition. However, as the path of metal flow gets smaller, the size of the grains becomes

comparable to the flow path, and generally grains prefer flowing in larger flow path, as shown by experiments using forward rod – backward can extrusion [49]. Grains with different orientation are also responsible to uneven metal flow in microforming as each individual grain has anisotropic response [50]. When strained, this anisotropic response becomes significant as the difference in deformation becomes comparable to the feature size on the part.

### *2.1.3 Summary on microforming and size effects*

Generally, the classification of sources of size effects provides an excellent approach to understand size effects. In previous investigations, the critical size effects for microforming were mostly derived from miniaturization sources or more specifically the *non-ideal miniaturization* for both *grain size* and *roughness*. The overall sources of size effects were acknowledged as summarized in Table 1. The increasing friction with miniaturization is generally observed in lubricated experiments and has been explained by the lubricant pocket model. As shown in Figure 6, the increase of friction is exhibited when using smaller workpiece (<1 mm diameter) which is in agreement with the lubricant pocket model. However, when this size of workpiece was used, the observed *m* is no longer constant.

An attempt to simulate lubricant leak by modelling the individual pocket in FE simulation has been presented by Dubar et al. [51]. However, the study does not predict the flow of lubricant leak well as the idealized lubricant pocket geometry used in the simulation does not correspond to the irregularly shaped lubricant pockets on the real surface. The work in this thesis aims to explore further on this explanation. More specifically, experimental and simulation study will be presented to provide

more complete explanation to lubricant pocket model. The use of solid lubricants with smaller natural lubricant thickness is also looked into in the current study.

Table 1: Classification of size effects in microforming

| Sources | Description & Example of effects |
|---|---|
| **Material Source** | |
| Grain size | Grain size influences the overall material property. E.g. higher flow stress with smaller grain size |
| **Miniaturization Sources** | |
| Non ideal grain size scaling | Part size scaled without grain size scaling; decrease in number of grains across dimension. E.g. softening of free surface grains, hardening of constrained surface grains |
| Non ideal roughness scaling | Part size scaled without roughness scaling; decrease in number of asperities and lubricant pocket. E.g. reduction of lubricant effectiveness |
| **Size Source** | |
| Part size | Part size influences force relations; lubricant surface tension becomes significant; affects specimen handling and de-moulding of specimen. |

## 2.2 Friction and Friction Control Using Surface Textures

### *2.2.1 Description of friction in metal forming*

#### *2.2.1.1 Friction models*

Friction is the resistance that one body encounters when moving over another. This resistance is a form of conversion of kinetic energy to heat energy. In a system such as passenger car, the energy to overcome frictions in engine, transmission system and tyres accounts for up to 1/3 of the fuel consumption [52]. On the other hand in metal forming system, this form of energy conversion results in excessive heating and shearing of tool and workpiece surfaces which then produce unwanted damage to products or excessive tool wear.

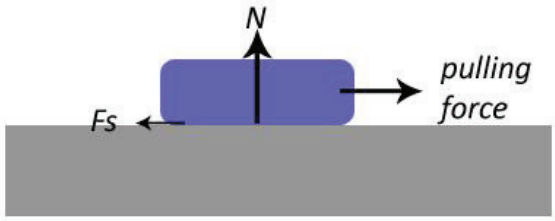


Figure 7: The simplest friction model, block on flat surface

1. *Coulomb Friction***.** Since the loads required to perform metal forming processes are usually large, the friction forces acting between the tooling and the workpiece are substantial. Friction force in the simplest case (Coulomb friction) is described by the force required to move a body along a flat surface as illustrated in Figure 7, and is governed by Equation 1.2:

$$F_s = \mu N \qquad 1.2$$

$\mu$ is called the *Coulomb coefficient of friction (COF)* [53], a proportionality constant which relates the friction force and the normal force between the body and the flat surface. In metal forming, friction is usually introduced as interfacial shear stress $\tau$, and consequently written as normalized variables given as Equation 1.3:

$$\tau = \mu p \qquad 1.3$$

This is the governing equation of the classical *Coulomb friction* or *sliding friction*. The new variable $p$ is the normal pressure, in order to normalize the equation with the contact area. The interfacial shear stress (or the frictional shear stress) is proportional to the normal pressure.

2. *Constant Shear Friction***.** However, given the possibility to have very large normal pressure, the frictional shear stress in metal forming may exceed the required stress to deform the material itself. If this happens, the surface of the workpiece in contact with the die remains stationary or sticks –thus referred to as *sticking friction* [54]. In this sticking friction, the frictional shear stress is constant, and is proportional to the shear strength of the material $k$ by a factor $m$ (Equation 1.4).

$$\tau = m k \qquad 1.4$$

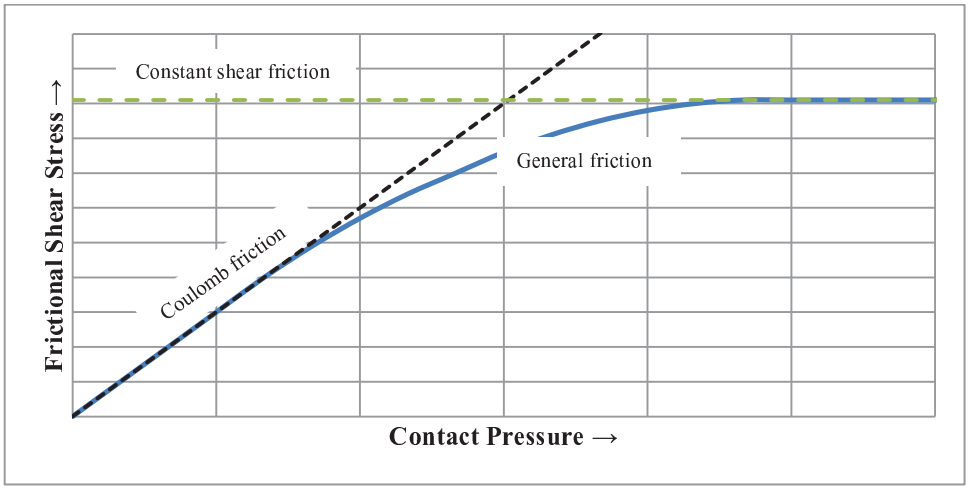


Figure 8: Friction models in metal forming

3. *General Friction*. In metal forming, the friction condition at the interface between two materials significantly affects plastic flow, changes the contact surfaces and alters process load requirement. The general friction model for metal forming was coined by Orowan [55] and improved by Wanheim et al. [56] and Bay [57], and is known as the Wanheim/Bay model as illustrated in Figure 8. This model of friction was proposed for bulk metal forming, governed by Equation 1.5:

$$\tau = \mu_{WB}\alpha_{RC}k \qquad 1.5$$

The Bay model includes the factor $\alpha_{RC}$ which is defined by the real contact area (asperities contact) divided by the nominal contact area, and the frictional shear stress is proportional to the shear strength of the material, *k*. In addition, Bay introduced the effect of surface roughness in the form of asperities angle (or slope) on the development of slip lines. The friction model (see Figure 8) shows that friction follows Coulomb law at low normal pressure.

The frictional stress can be described as a function of normalized normal pressure ($p/\sigma_y$) as illustrated in Figure 9. The model describes friction as proportional to normal pressure at low pressure and becomes constant at high pressure, adjoined by material dependent proportionality limits ($p^*, \tau^*$ in Equations 1.6 through 1.9). The proportionality limits are defined considering the development of slip lines using zero angle asperity (flat surface) [57, 58].

$$\left(\frac{\tau}{k}\right) = \left(\frac{\tau^*}{k}\right)\frac{\left(\frac{p}{\sigma_y}\right)}{\left(\frac{p^*}{\sigma_y}\right)} \quad \text{for} \quad \left(\frac{p}{\sigma_y}\right) \leq \left(\frac{p^*}{\sigma_y}\right) \tag{1.6}$$

$$\left(\frac{\tau}{k}\right) = \left(\frac{\tau^*}{k}\right) + \left(\mu_{WB} - \left(\frac{\tau^*}{k}\right)\right)\left(1 - \exp\frac{\left(\left(\frac{p^*}{\sigma_y}\right) - \left(\frac{p}{\sigma_y}\right)\right)\left(\frac{\tau^*}{k}\right)}{\left(\mu_{WB} - \left(\frac{\tau^*}{k}\right)\right)\left(\frac{p^*}{\sigma_y}\right)}\right) \quad \text{otherwise} \tag{1.7}$$

$$\left(\frac{\tau^*}{k}\right) = 1 - \sqrt{1 - \mu_{WB}} \tag{1.8}$$

$$\left(\frac{p^*}{\sigma_y}\right) = \frac{1 + \left(\pi/2\right) + \arccos\mu_{WB} + \sqrt{1 - {\mu_{WB}}^2}}{\sqrt{3}\left(1 + \sqrt{1 - \mu_{WB}}\right)} \tag{1.9}$$

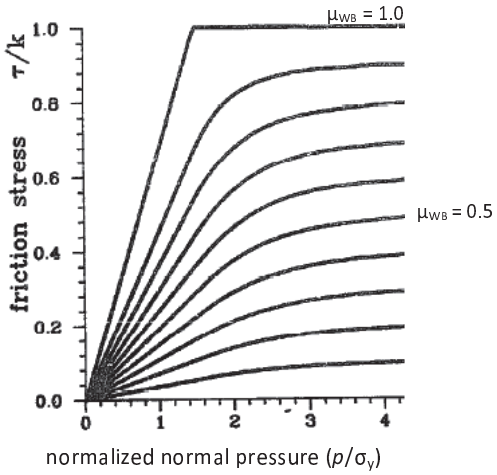


Figure 9: General friction model at various friction coefficients [56]

4. *Adhesion Friction.* Generally, friction can be distinguished by adhesion and ploughing (or abrasion) frictions [59, 60]. Adhesion friction is attributed to the bonding of real contact surfaces (as asperities) due to physical and chemical interactions, which is called micro welding. Abrasion friction is attributed to the shearing of the workpiece (the softer material) by the asperities of the tooling (the harder material).

The adhesion friction theory was introduced by Bowden and Tabor assuming that friction was attributed to the adhesion between asperities of the workpiece with asperities from the tooling [61]. Adhesion friction is usually modelled by using rough workpiece and smooth tool (RW/ST) as illustrated in Figure 10. During the loading, the asperities of the rough workpiece experience plastic deformation, and further deform to take the shape of the smooth tool, and increase the real contact area.

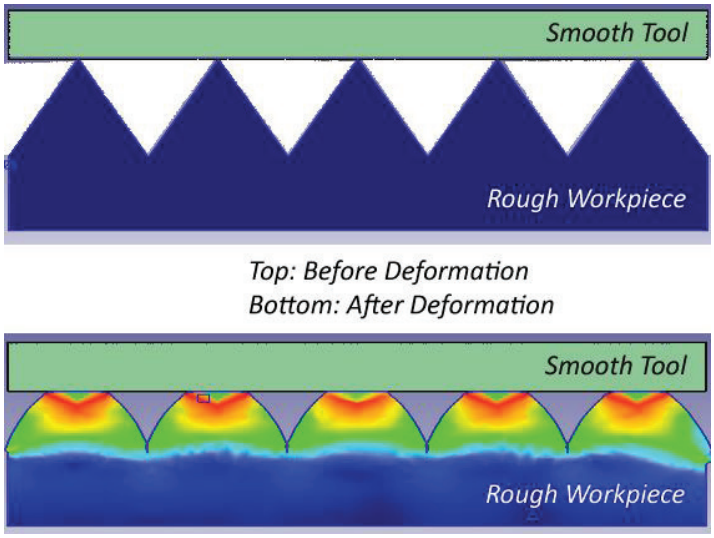


Figure 10: Representation of smooth tool – rough workpiece model

The portion of real contact area as compared to the overall area (or apparent area) increases as loading continues, until all the apparent area are in contact (100% real contact area). Therefore, the higher the loading, the higher is the friction since the contact area increases, which is in accordance to the classical Coulomb law. However, Coulomb law does not explain what happens when the loading is further increased when the area is already 100% in contact.

5. *Ploughing Friction*. Alternatively, friction can also be modelled using ploughing or abrasion friction (SW/RT) as represented in Figure 11. In ploughing friction, the rough tool ploughs through the softer workpiece. The frictional shear stress is then proportional to the shear strength of the material. The more resistant the material is to shearing, the higher the frictional shear stress, which is consistent with the shear friction.

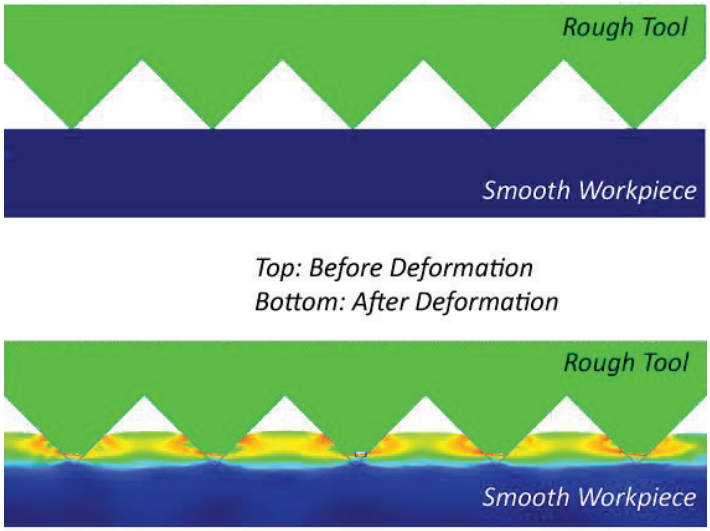


Figure 11: Representation of rough tool – smooth workpiece model

Realizing that both workpiece and tooling can never be microscopically flat, a more complex dual asperities (RW/RT) interaction which is combination of adhesion and ploughing friction has also been modelled.

#### *2.2.1.2 Lubrication regimes*

The most common way of reducing friction is to introduce lubrication on the interface. Four main regimes of lubrication in metal forming were introduced by Wilson [62] as follows:

1. *Thick Film Lubrication*, in which the thickness of the lubricant is much higher (> 10 times) than the root mean square (rms) roughness such that the two surfaces are never in contact and lubricant can be seen as continuous entity on the interface. Thus, contact force in this lubrication is carried entirely by the lubricant.

2. *Thin Film Lubrication*, exists when the lubricant thickness is between 3 and 10 times the rms roughness. In this case contacts between asperities are negligible.

The difference that was raised in thin film lubrication is that the surface roughness may affect lubrication process. In other literature [63], thick and thin film lubrication are regarded as "full film lubrication."

3. *Boundary Lubrication*, exists when lubricant is present in very limited amount. The contact forces between the two surfaces are carried by the asperities only, with the lubricant merely adhering to the two surfaces and not performing any load bearing function. Significant wear may happen at this lubrication condition, and surface roughening (from wear and galling) may occur as well.

4. *Mixed Lubrication*, exists when boundary lubrication and thin film lubrication take place simultaneously at different locations. In mixed lubrication, the contact force is carried partly by the lubricant, and partly by the asperities.

Illustrations of the different lubrication regimes are provided in Figure 12. When lubricant is present on the interface, the definition of friction is no longer based on adhesion and ploughing. There is a third factor of lubricant behaviour. Friction then becomes a more complex phenomenon as lubricant behaviour can be a function of viscosity, sliding speed, contact pressure, surface topography and material's mechanical properties [64-66].

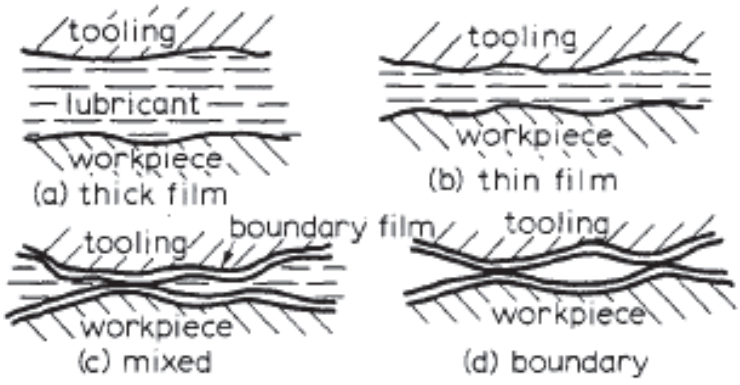


Figure 12: Different regimes of lubrication in metal forming [62]

### *2.2.2 Friction control using surface textures*

Tribological surface textures are highly defined surface features introduced on the surface with the objective of friction control. These textures are commonly fabricated using processes such as laser machining, lithography, abrasive jet machining or patterning using hard tool. For the textures produced by laser machining, especially using long pulse lasers, e.g. nanosecond lasers, severe bulging at the rim of the textures caused by solidification of molten metal are commonly observed. However, a recent study has determined that bulging may not have detrimental effect and overall, textured surface, even with bulging at the rims, still produces lower friction than its untextured counterpart [67].

As discussed in studies on size effects, tribological surface texturing should be considered in microforming since the lubricant effectiveness is reduced appreciably by reducing part size as miniaturization derived size effect. The demand of surface textures in microforming is that the textures can be fabricated on the dies and they lower friction appreciably, do not pose significant negative effect (for example to part

surface finish), and that the textures can be retained after repeated cycles to reduce cost of die maintenance.

Extensive results on various metals and ceramics have been published on friction control using surface textures, or tribological surface texturing, for both lubricated [68] and unlubricated [69]. The application of surface texturing in microforming has been attempted by Brinksmeier et al. [70] through experimentation with the strip drawing test (Figure 13) and Eriksen et al. with the strip reduction test [71]. Through the strip drawing test, it was observed that lowest friction is observed not using the smoothest or roughest sample but rather there is an optimum finish and it is worth noting that the textures used by Brinksmeier et al. is not considered highly defined texture but rather careful machining to produce controlled machining lines/pitches. Moreover, this investigation on microforming is limited to those based on sheet metal forming and the application to bulk metal forming with higher typical contact pressure has been limited to its implication to tool life [72, 73]. In general, the studies on optimized surface for microforming have only been associated with the effect of surface roughness (not highly defined textures).

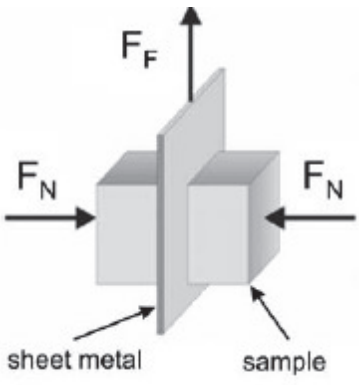


Figure 13: Schematic of strip drawing test [70]

Suh et al. [74] and Tian et al. [75] found that in the case of no lubrication, appropriate surface texturing can reduce the friction by means of trapping wear particles and thus enhancing contact life. Study by Suh [74] shows that for properly undulated bearing, the friction can be reduced to be as low as using boundary lubrication. For the case of boundary lubrication, textures can act as lubricant trap such that lubricant can stay longer at the interface [76, 77]. For the case of full film lubrication, appropriate textures can act to improve the hydrodynamic behaviour of the lubricant [78-80].

Suh et al. [74] also states that the objective of having textured surface is for its usability at elevated temperature as some liquid lubricants are prone to oxidation and evaporation at high temperature. The results of this study also assert that adhesion friction is not the primary mechanism of friction in sliding surfaces as the chemical compatibility of the surface does not affect the friction in the study using textured surface.

However, in contrary to the friction reduction mechanisms proposed, i.e. lubricant entrapment for lubricated contact and wear particle entrapment for unlubricated contact, other investigations have shown that there is a possible secondary explanation to the role of surface textures. In experiments by Borghi et al. [69] and Suh et al. [74], friction reduction has been observed in early stage of sliding contact. The result from Borghi et al. is presented in Figure 14.

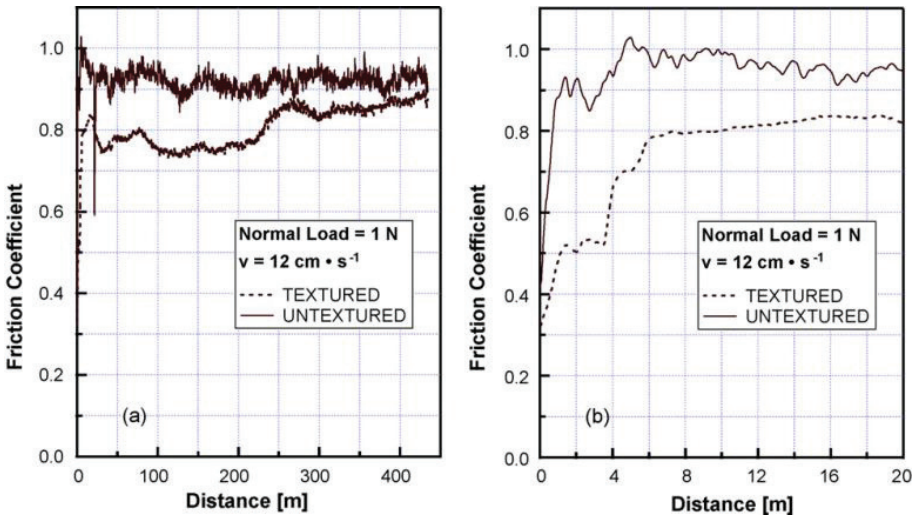


Figure 14: Friction reduction in unlubricated contact [69]

According to the delamination theory of wear [81], wear particles or wear sheets are not directly generated when two surfaces slide across each other. In contrast, there are development stages in the generation of wear sheets, starting with the nucleation of sub-surface voids, coalescence of sub-surface voids to generate sub-surface cracks, and concluded with the complete delamination of the surface above the sub-surface cracks when the size of the cracks reaches a critical value. This sub-surface cracks have been documented by Suh as presented in Figure 15. If the friction reduction with surface textures in unlubricated contact is only attributed to entrapment of wear particle, the friction reduction would not have started early in the sliding.

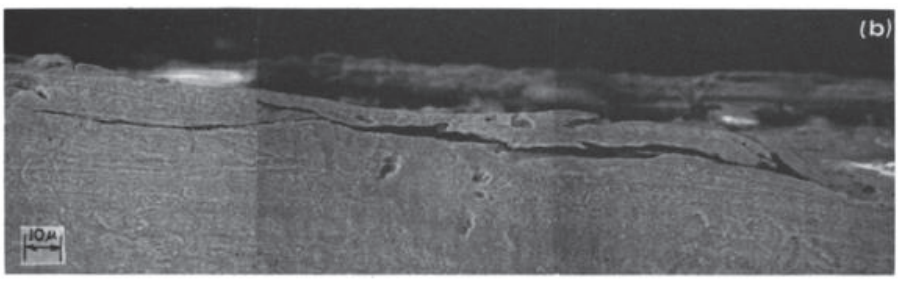


Figure 15: Crack formation in copper sample [81]

Similarly, investigations using lubricated contact have also suggested a secondary explanation to the role of surface textures. Schreck and zum Gahr [68] presented experimental results of steel to steel contact with the textured surface producing lower friction than polished surface even when the setup is completely immersed in distilled water (see Figure 16). If the role of surface textures were only to trap lubricant, the textured surface should not produce lower friction as lubricant is always available at the contact in such configuration.

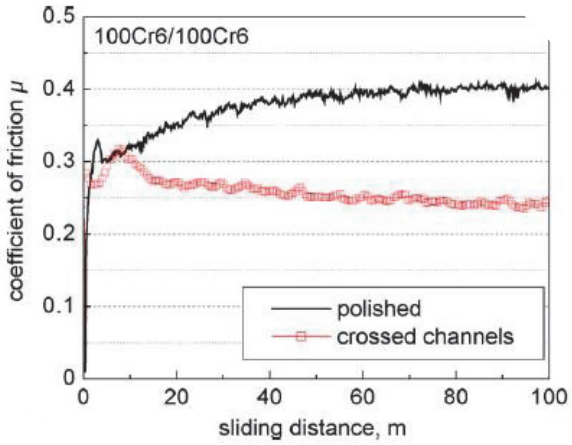


Figure 16: Friction reduction in immersed contact [68]

Koszela et al. [82] also discovered that surface textures which is designed optimally in terms of size and density can reduce wear rate in the running in state of new sliding components.

#### *2.2.2.1 Pore textures*

Different surface textures have been studied in various researches. Pores or holes [77-79, 83] have been identified as beneficial textures with the trend of reducing friction as pore size to contact area ratio increases (larger pore) [83] and these textures were created by either abrasive jet machining or laser machining. However, introducing too many pores (higher surface area fraction) can impair the texture beneficial effect [78,

79, 83] by increasing the friction and/or promoting wear. Uehara et al. [77] proposed that too many pores results in increased contact pressure (because of less load bearing area) which further increases friction. Figure 17 presents the examples of tribologically textured surface using pore textures. While there is an attempt to create pores of different geometries on one surface [84], the current study is focused on periodic textures.

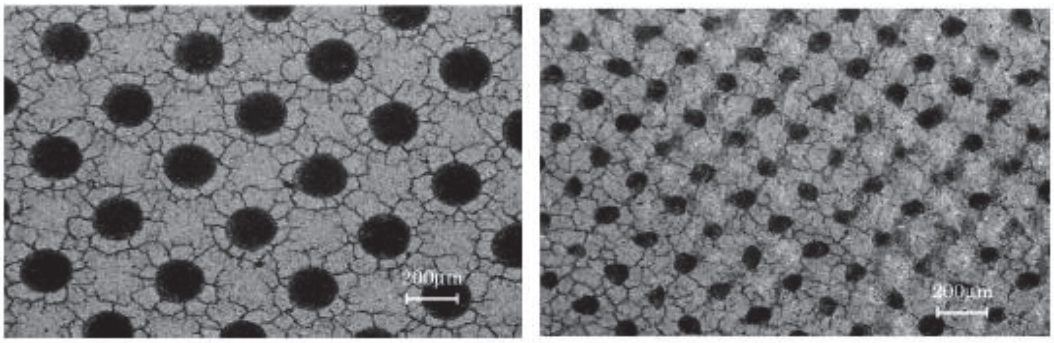


Figure 17: Example of pores textures [79]

The idea that should be highlighted for pore-textured surface is that the friction is higher when the pore density is increased. That is because more pores do not help in making the surface lubrication even better, and yet the increased contact pressure brings in negative influence. Almost all studies involving pore textures report lowest friction at lowest pore density tested. Notable exception was reported by Li et al. [77, 85] in which nickel composite with three pore densities of 1.8%, 7.1%, and 11.2% (of total area) were tested for their friction behaviour. Under lubrication with molybdenum disulphide ($MoS_2$) powder, the specimen with 7.1% pore density exhibits lowest friction reading. This suggests that there may be a changing behaviour if one were to switch between untextured surface and textured surfaces with different densities.

Uehara et al. [77] proposed a friction model for contact involving tribologically textured surfaces by considering the effect of oil supply and contact pressure, as illustrated in Figure 18. When surface textures are introduced, the textures act as lubricant reservoir so that more lubricant can stay within the contact region instead of getting wiped away. Textures such as grooves may also act as tiny channels for lubricant to flow back to the contact region after it gets wiped away. This results in reduced friction. However, increasing the density of textures even further reduces the load bearing area, increasing contact pressure and friction subsequently.

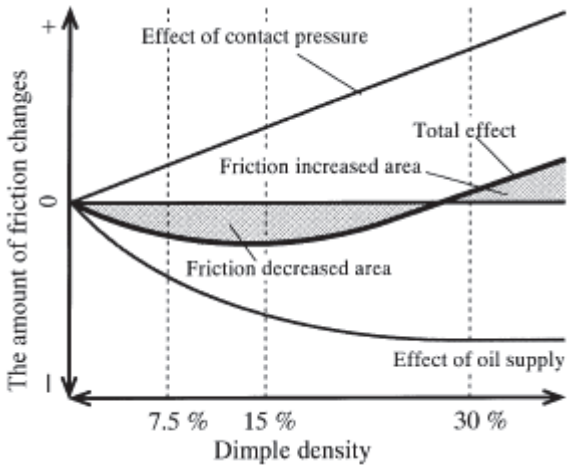


Figure 18: Effect of Pore (Dimple) Surface Textures [77]

#### *2.2.2.2 Grooves and rectangular recess*

Pettersson [63, 86] used grooves and crosshatches patterns on steel using diamond master textured surface. The master textured surface was produced by CVD process of diamond on previously etched silicon backing. Figure 19 presents the example of textures used by Pettersson [86].

Using reciprocally sliding ball on textured flat using grooves and rectangular recess textures of different sizes (and same texture density), it was found that small-sized and well oriented textures are exhibiting beneficial behaviour of reducing friction and wear. Small-sized and well oriented textures are thought to provide better re-lubrication of the contact surface, and in turn reduce the friction. This influence is stronger when the amount lubricant is very little.

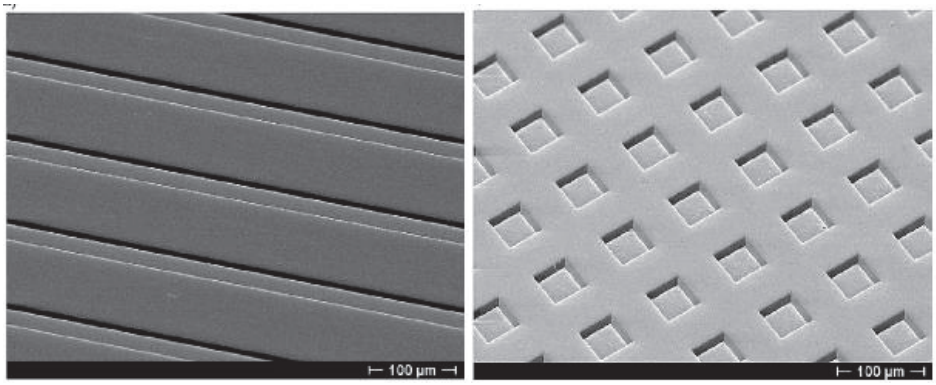


Figure 19: Example of grooves and squares textures [86]

When more lubricant is added (but still in boundary lubrication regime), interestingly the friction was reported to be higher, and the choice of textures becomes less influential towards the friction.

The increased friction using more lubricant is speculated to be attributed to the viscous property of the lubricant. The load used in studies by Pettersson [86] was kept low (5 N for 10 mm steel ball on flat surface) to avoid accidental fracture on the brittle silicon surface. At low normal load, and with friction coefficient of only 0.05 – 0.10, the actual tangential load (attributed as friction) was only 0.25 – 0.5 N, and thus the viscous attribute of the lubricant, including the surface tension may have affected the results.

In a different study, Pettersson [87] examined the influence of groove and crosshatch patterns on roller-piston movement. The results show that although the textures do not reduce friction appreciably, they reduce the magnitude of reading scatter. Appropriate lubrication should reduce the stick-slip behaviour. In other word, the reduced scatter may be due to the improved lubrication upon introducing surface textures.

#### *2.2.2.3 Directional grinding*

Menezes [88-91] uses directional grinding and polishing to examine the performance of directionally ground surface as surface textures on various materials. It was found that both for the case of unlubricated and lubricated conditions, the values of surface roughness do not affect the measured friction. This studies use three different grinding directionalities: perpendicular to sliding direction, parallel to sliding direction, and grinding in figure of "8", as well as randomly polished surface as reference. It was found that both unlubricated and lubricated conditions, textures perpendicular to sliding direction produce highest friction reading. Others produce appreciably lower friction.

Randomly polished surfaces produce lowest friction for both dry and lubricated conditions. However for dry condition, this low friction value increases as the surface wears, and in the long run all surfaces produce the same measured friction for dry condition as all textures were worn away [91]. In dry conditions, the results from directional grinding were not able to produce the results expected from tribological surface texturing.

The use of lubricant was reported to help the textures to prevail after repeated sliding. In experiments using Al-4Mg pin sliding on 080M40 (AISI 1040) steel, it was

reported that all textures were lost after repetitive sliding without lubrication, but not in cases with lubrication. Randomly polished surfaces show lowest friction as compared to other directionality.

It was then concluded, since randomly polished surfaces (without directionality) generally produce lowest friction, that tribological surface texturing using directional grinding was not useful. The explanation for this can be derived back from the intention of having surface textures in the first place, to trap lubricant and/or wear particles, in which case the ground surfaces will never be deep enough to function.

### *2.2.3 Summary*

Friction can generally be attributed to adhesion and ploughing interactions which cannot be uniquely isolated in experiments. Friction models such as Coulomb friction, constant shear friction and general friction have been introduced and they can be directly used in simulation or experiment. These friction models can be used to quantify the magnitude of friction in systems for practicality without having to consider the amount of adhesion or ploughing for every specific case of contact.

In the case of tribological surface texturing, with the exception of using directionally ground surfaces, surface textures can be utilized as friction control when provided in small amount. However, when present in excess, surface textures produce negative effect. Excessive surface texturing increases the local contact pressure since the same loading needs to be carried by smaller contact area. Uehara [77] (Figure 18) speculated that in lubricated condition, there is an optimum amount of surface texture to be introduced to minimize friction. Even though the study was done using pore textures, the behaviour may extend to other textures. These surface textures may

function by trapping wear particles when the contact is dry or unlubricated, or by trapping lubricant within the contacting region when lubricant is present. However, past experiments have suggested that there may be a secondary mechanism of friction control as suggested by Schreck and Zum Gahr [68] as well as Borghi et al. [69]. The surface textures reviewed in this chapter and elaborated in Chapter 5 are defined as geometrically deterministic surface features with sizes range between 40 and 200 μm such that in the context of microforming, the surface to surface contacts always cover at least a few textures.

Simulation study on surface texture is therefore chosen to provide the explanation on the friction control mechanism using surface textures. Simulation is chosen as it enables the investigation of various contact properties such as the strength of the contacting materials and it allows closer examination on the physical mechanism as experiment will be unable to separate the various interlinked factors contributing to friction (both adhesion and ploughing). The work also aims to examine whether surface textures can be used to provide friction control for bulk microforming.

## 2.3 Friction Test in Metal Forming Design

In metal forming design, researchers use generic friction tests such as double cup extrusion test or ring compression test, with the help of simple FE prediction, in order to approximate the amount of friction that takes place when metal forming engineers need to use new materials or different lubrication. These friction tests use specific geometry that is sensitive to friction. The idea behind friction tests is that the finish geometry (or the load reading) from the test will change depending on the process conditions (mainly materials and interface friction).

Numerous friction tests for metal forming have been developed with different geometries and method of characterisations. In conducting the tests, users are usually required to match their experimental results with known calibration curves which can be produced by either theoretical derivation [92] or simulation methods [93, 94]. In general these calibration curves are not universal. Hence new calibration curves are needed when a new material is used.

### *2.3.1 Criteria for microforming friction tests*

Friction investigation in microforming is in need of such a friction test. Previously, friction researches in microforming have been conducted using friction tests which have been developed for conventional size metal forming. As these tests are scaled down, fabrication of tooling for the friction test can be deemed impractical and unreliable as the production of miniature intricate tooling with precision is both labour- and cost-extensive [95]. In the same fashion, fabrication of specimen, handling and examining the results of the test also become major difficulties.

A suitable test for microforming should have good friction sensitivity and consider the following criteria.

#### *2.3.1.1 Scalability*

In accordance with the definition of microforming [1] and tooling fabrication constraints [95], friction test for microforming should be able to scale easily to micro sizes. In addition, the geometry of the tooling must allow users to produce, modify and characterise the contact surface conditions, e.g. surface finish, tool wear, galling marks. Hence, it is favourable that the test does not have internal surfaces. Finally, it

is desirable that the workpiece geometry is simple to allow inexpensive workpiece preparation.

#### *2.3.1.2 Characterisation approach*

Interpretation of results in friction test for microforming must not be affected by material size effects. Dieter et al. [96] showed that flow stress of a material in microforming is affected by the part size and its relation to grain size. In a different work, Engel et al. [2] proposed an empirical surface layer model in a bid to explain the mechanism of how forming load is not always proportional to the workpiece size when components are miniaturised to sub millimetre in dimension. The model differentiates mechanical properties of the surface region from the bulk region. Hence, although friction influences forming load, a change in forming load does not necessarily mean a change in friction. Consequently, the interpretation of friction test for microforming should not rely solely on forming load.

#### *2.3.1.3 Handling*

Due to the handling difficulty in microforming in general, even bulk microforming processes have been using sheet metal as the larger sheet can be fed with relative ease, such as the micro-forging/extrusion process [97] and the micro progressive forming [98]. This further gives rise to the process called sheet-bulk metal forming (SBMF) for conventional size forming which has been developed in recent years by Merklein and co-workers [99-101]. As the current study for microforming is focused on bulk microforming, the test must be designed for easy setup and manipulation despite the small workpiece (not sheet metal). This requirement includes the design of tooling features to self-locate the workpiece prior to friction test and avoid the need for

auxiliary equipment. In addition, the geometry of the test should allow controlled and even lubrication.

#### *2.3.1.4 Contact pressure at interface and material plastic deformation*

In order to recreate the contact conditions in bulk metal forming, the friction test should produce contact pressure well beyond the yield stress of the material. Petersen et al. [102] suggested that contact pressure determines contact behaviour which eventually influences friction based on slip line field analysis. The strain during the test and the tooling configuration are main contributors to the contact pressure at the interface. Finally, large permanent deformation of workpiece must be produced during the test to simulate actual metal forming processes more accurately.

### *2.3.2 Availability of friction tests*

The currently available friction tests (Table 2) and their suitability for implementation in microforming is further discussed:

Table 2: Available friction tests for metal forming

| | | |
|---|---|---|
| 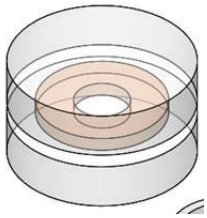 **Ring compression test** | 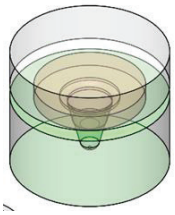 Spike forging | 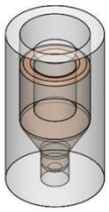 Backward-can forward-rod extrusion |
| 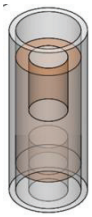 **Double cup extrusion** | 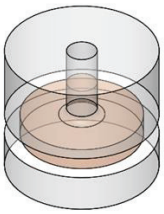 Open die backward extrusion test | 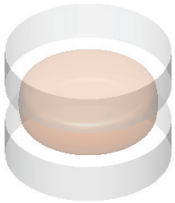 Cylinder compression |
|  **Forward extrusion** |  T-Shape test | 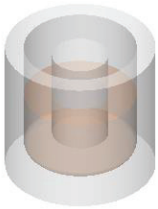 Tip test |

### *2.3.2.1 Ring compression test*

Ring compression test (RCT, also called ring test) uses a ring-shaped workpiece compressed between flat dies. The interfacial friction between the tooling and workpiece creates preference in metal flow direction. Hence by examining the geometry of finish specimen, users can conclude the magnitude of friction occurring during the test. Male and Cockcroft [103] proposed this test in 1964 and produced an example of calibration for RCT based on different Coulomb friction coefficients with workpiece geometry ratios of outer diameter to inner diameter to height of 6-3-2 (6:3:2). In the examination using constant friction factors, it was also established by Danckert and Wanheim [92] that the calibration approach –theoretical consideration

or simulation algorithm, and the strain hardening of the material influence the calibration curves. Several studies reviewed in the same manuscript [92] suggested that the geometry ratio of 6:3:2 has been used extensively and is hence regarded as the unofficial standard for RCT. The influence of material strain hardening on distribution of contact pressure and friction is also documented by Tan et al. [93] using RCT with different ring geometries. Ultimately, although RCT has also been used in simulation based friction investigation in microforming [104], extensive usage in microforming experiment is not desirable since RCT: 1) involves difficult and expensive ring workpiece fabrication, and 2) does not produce the desired contact pressure due to its open die setup.

#### *2.3.2.2 Spike forging*

Spike forging (SF) geometry was first used in a FE analysis [105] and was also used in non-isothermal forging simulation [106]. Although it is not originally designed for friction testing, SF was proposed by Isogawa et al. [107] as friction test for forging as it produces higher contact pressure and larger permanent deformation of the workpiece in comparison with RCT. Users are able to quantify the magnitude of friction in SF by measuring either the spike height, the forging load, or the ejecting load needed to remove the forged workpiece. Optimum workpiece aspect ratio (length to diameter) of 0.5 was proposed as it results in balanced extrusion and upsetting deformation as well as most severe metal flow [108]. This aspect ratio also results in the highest spike height sensitivity to friction. However, the pre-test preparation of SF requires placement of workpiece to be concentric to the die which is deemed difficult for implementation in microforming without auxiliary equipment.

#### *2.3.2.3 Backward-can forward-rod extrusion*

Backward-can forward-rod extrusion (BCFRE) was introduced by Kuzman et al. [109] to replicate the metal flow behaviour in bulk metal forming. BCFRE was used in microforming analysis to investigate the changing behaviour of metal flow when the flow channel size is comparable to the grain size [1]. Nevertheless its extensive implementation for microforming is made difficult due to the BCFRE's reliance to internal contact surface. Internal contact surfaces are generally difficult to fabricate and characterise. They also do not support controlled lubrication.

#### *2.3.2.4 Double cup extrusion*

Double cup extrusion (DCE, also called double forward-backward extrusion) was introduced by Buschhausen and co-workers [110] and has become a popular test for bulk metal forming. Its use in microforming friction investigation has been presented by Geiger at al [1]. The same study documented the trend of increasing friction with miniaturization. Tan et al. [111] and Schrader et al. [94] also concluded that DCE results are influenced not only by material properties (initial state and hardening) but also by the detail geometry of the tooling. Because of its similar construction to BCFRE, DCE is also considered impractical for use in microforming because of the presence of internal surfaces.

#### *2.3.2.5 Open die backward extrusion test*

Sofuoglu and Gedikli [112] proposed the open die backward extrusion test (ODBET) as an alternative to RCT for friction examination. It is designed primarily to allow high permanent deformation of the workpiece. In OBDET, friction affects the amount of backward extrusion. Users can quantify the magnitude of friction during the test through measurement of the height of the extruded material. Similar construction has

also been called micro pin forming in a more recent research [113] to investigate the friction and metal flow behaviour in microforming. The drawback of ODBET or micro pin forming for microforming investigation is its reliance on internal surface for the backward extrusion channel.

#### *2.3.2.6 Cylinder compression*

Ebrahimi and Najafizadeh [114] proposed that the barrelling or bulging during cylinder compression (CC, also called barrelling test) can be examined to quantify friction. In CC, higher friction results in more severe barrelling and the magnitude of friction can be deduced by recording the differential development of diameter of the cylinder at die interface and at mid-height during the compression. However, its implementation for microforming investigation is limited because as workpiece continues to miniaturise, the small barrelling can become too minute so that diameter measurements become increasingly difficult.

#### *2.3.2.7 Forward extrusion*

Forward extrusion (FX) was introduced by Krishnan and co-workers [115]. As widely understood, friction in metal forming influences both forming load and the preferential direction for metal flow. Therefore, in the case of most friction tests, the friction can be characterised by examining the forming load, or the final geometry of the workpiece, or both. However, unlike other friction tests for metal forming, FX uses fixed metal flow and relies solely on forming load to determine the amount of friction during the test. This sole reliance on forming load is the main drawback for FX as the forming load is also known to be influenced by material size effects.

#### *2.3.2.8 T-Shape test*

T-Shape geometry [116] was designed to produce high contact pressure and permanent deformation of the workpiece to simulate an actual cold forging process. Friction in T-Shape test gives rise to metal flow competition between upsetting and extrusion directions. As the change in friction gives rise to differential in metal flow pattern, the forming load at the same stroke position will be determined by the friction. T-Shape test was considered to be unsuitable for microforming friction investigation as the characterisation uses measurement of the forming load.

#### *2.3.2.9 Tip test*

Backward extrusion test or also known as tip test (TT) [117] combines the processes of upsetting and backward extrusion. The geometry is similar to an earlier bucket test introduced in 1992 [118]. Due to the constraint of the die, TT is a friction test with largely fixed metal flow and its characterisation relies on measurement of forming load development during test and is therefore unsuitable for microforming.

### *2.3.3 Summary*

Friction test is essential in design of metal forming process as its result can be used to predict the process behaviour which leads to appropriate die design, lubricant selection, damage prediction, etc. Similarly, microforming friction investigation needs a well-suited friction test design. There are many friction tests which can be used for microforming investigation. However, there is no suitable test which can be directly used in microforming (see Table 3) and therefore a development of a new friction test for microforming is required.

Table 3: Suitability of various friction tests for microforming

| Friction Test | Scalability | Characterization approach | Handling | Contact pressure & Plastic deformation |
|---|---|---|---|---|
| Ring compression test | O | O | X | X |
| Spike forging | X | O | X | O |
| Backward can-forward rod extrusion | X | O | O | O |
| Double cup extrusion | X | O | O | O |
| Open die backward extrusion test | X | O | X | O |
| Tip test | X | X | X | O |
| Cylinder compression | O | X | O | X |
| Forward extrusion | X | X | O | O |
| T-Shape Test | X | O | O | O |

Remarks: O – Suitable , X – Not Suitable

# CHAPTER 3 MATERIALS AND METHODS

## 3.1 Description of Works

Due to the various work conducted, both simulation and experimental, the materials and method will be presented in sections with respect to the work for which they are used. Preliminary introduction of materials and method used in the course of the Ph.D. is presented in the current chapter while more specific and detailed justifications of the methods are presented in the corresponding result chapters.

## 3.2 Properties of Materials in Friction Test Simulation

FE analysis codes Deform 2D and Deform 3D will be used in the design of the friction test for microforming. These FE codes are powerful simulation systems designed specifically to examine two- and three-dimensional material flow during complex metal forming processes.

These codes were chosen for this friction test design as they are especially optimized for metal forming design with the enhanced automatic remeshing, solution mapping throughout the process, as well as automated contact determination for multiple deforming bodies.

The evaluation of the friction test can be done using the simulation when at least the mechanical (flow stress) and interaction (friction) properties are supplied for the simulation. For this purpose, upsetting of cylindrical ETP Copper was conducted prior to the investigation. The specimen diameter was chosen to be 1.0±0.01 mm and height of 1.5±0.01 mm in order to provide the mechanical properties of the material at the limit size of microforming. This specimen was fabricated from a 3.2 mm diameter

rod. The rod was then machined using centreless grinding to achieve the desired 1.0 mm diameter.

The mechanical tester Instron 5569 with load cell of 5 kN (accurate to 12.5 N (0.025% of maximum load)) was used for this investigation. Teflon sheet was supplied above and under the workpiece during the test to minimize friction interference to the results. Figure 20 presents the mechanical properties obtained from the upsetting test.

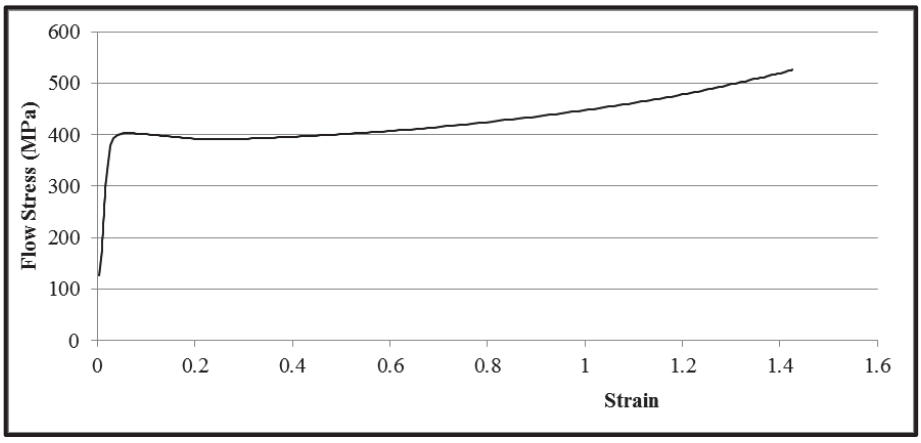


Figure 20: Stress v Strain of upset specimen (used in 2D simulation)

Considering that the mechanical testing system and the Teflon sheet may not be perfectly rigid, the raw data from the experiment was subject to several correction steps in order to correctly set the zero stroke and to compensate for elastic deflection of the setup. This data refinement procedure is presented in Appendix B.

The refined data will be used throughout the 2D simulation study in the design for the friction test for microforming. The constant shear friction factor, *m*, will be used throughout the simulation as this friction model is more generally used for metal forming simulations [1, 110, 114, 116, 119]. The 2D simulation is aimed specifically

to investigate the effect of material properties variation and to establish geometric tolerance for the experimental tooling.

Once the die design and the tolerance are established, the friction test will then be used to perform friction investigation. The setup will be designed and fabricated to fit into the Schmidt servo press 420 with rated 4.2 kN loading capacity (Figure 21).


Figure 21: Schmidt ServoPress 420 equipment

For the experiment, it is important that the test is designed to be performed without pre-machining of specimen in order to reduce test cost. In that regard, a new batch of materials was sourced for the experiment. During this investigation, materials in wire form of 1 mm diameter are chosen. The robustness of the setup will be tested as the procedure for the friction test is to avoid the use of non-generic equipment from specimen preparation to characterization.

Alongside the experiment, 3D simulation will be performed to provide the test's calibration curves to determine the magnitude of the prevailing friction. With wire material, the common methodology to characterize its mechanical property is through

tensile test. However, wire material's mechanical response under tension and compression may be different. Therefore, the material properties supplied with the Deform 3D are used instead. Such examples for standard aluminium and copper are provided in Figure 22. Although these material properties may still not be representative of the experiment materials, as it will be shown in Chapter 4, there is no significant effect of the mechanical properties to the microforming T-Shape test result.

Due to numerous physical phenomena occurring during metal forming, the following assumptions are considered in simulations throughout Chapter 4:

- Material is considered as continuum, isotropic and homogeneous.
- Standard contact formulation of penalty method in Deform is used. Real surface with asperities is simplified with smooth surface and constant shear friction factor.
- Geometric assumption of plane strain is used in the 2D simulation.
- These non-simulated behaviours are considered to have no or insignificant effect on the results: heat generation due to friction, material delamination (wear and galling).

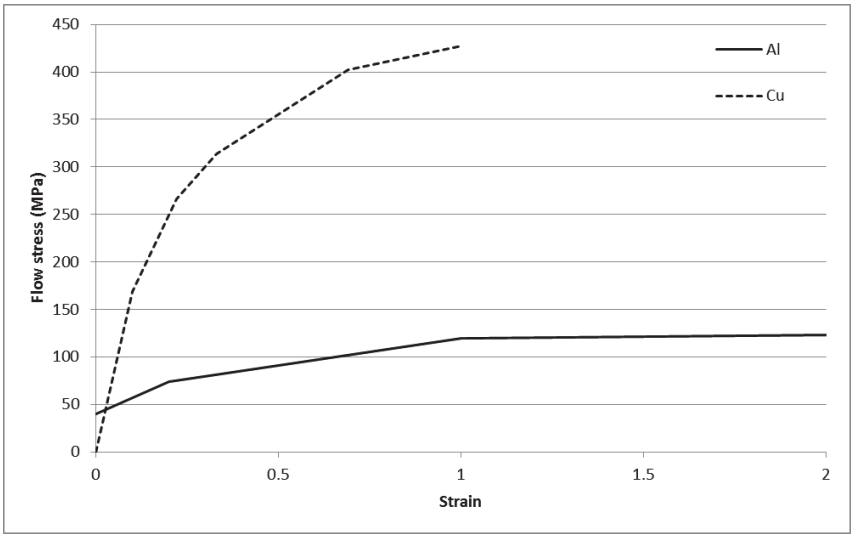


Figure 22: Material properties used in 3D simulation

## 3.3 Surface Textures for Friction Control

FE analysis code Abaqus will be used in this part of the study. Abaqus is a complete multiphysics simulation code which supports various material models, interaction models, etc. without the use of user subroutines.

This analysis code will be used to examine the mechanism of friction control occurring when surface textures are present. Three-dimensional textures (pore and two-directional grooves) will be examined in the current study.

Using Abaqus, the simulation inputs the material model, the friction behaviour for the flat surface and texture geometry in order to produce a new texture-dependent friction definition. The acquired friction behaviour can further be used directly in metal forming process simulation in order to simulate the process with surface textures introduced without introducing the texture geometry in the simulation to reduce computational cost. The friction behaviours for both the input given and output

extracted are in the form of pressure-dependent Coulomb friction coefficient. The schematic of the simulation is presented in Figure 23.

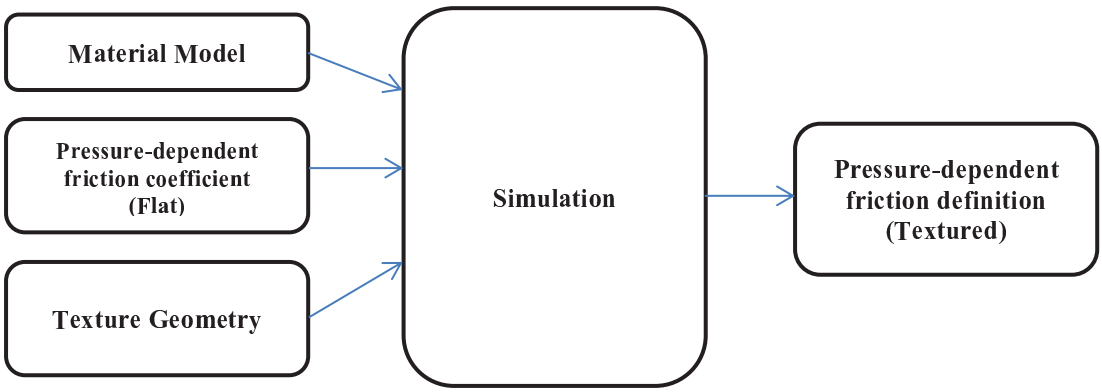


Figure 23: Simulation scheme (input and output)

The following assumptions are considered in simulations throughout Chapter 5 on surface texture simulation:

- Material is considered as continuum, isotropic and homogeneous.
- Standard contact formulation of penalty method in Abaqus is used. Real surface with asperities is simplified by using smooth surface and pressure dependent friction coefficient (see Figure 23).
- These non-simulated behaviours are considered to have no or insignificant effect on the results: heat generation due to friction, material delamination (wear and galling).

These textures will be examined using 3D simulation and the 3D mesh shown in Figure 24. As there is no available consensus on producing representative mesh for periodic contact simulation, the three-dimensional mesh used was chosen as such to provide the necessary details across the x- and z- axis for the periodic length of the textures of 100 x 100 μm with the thickness of the mesh 15 μm. Periodic boundary

condition is set such that any movement of each node on the -X face is equally experienced by the mirroring node on the +X face. Therefore, any stress from the sliding contact (both normal (y-direction) and shear (x-direction)) is shared equally by the two faces as if there were textures on the right hand side of the +X face and on the left hand side of the -X face creating periodic stress field on the workpiece. On the other hand, the periodic textures along the z-direction will have cancelling effect on the periodic simulation mesh and hence it is sufficient to prescribe -Z and +Z faces with zero z-direction movement.

In the simulation of surface textures, the material property definition used for the workpiece is based on elastic-plastic material property with yield strength of 178 MPa and post-yield stress-strain relation as presented in Figure 25.

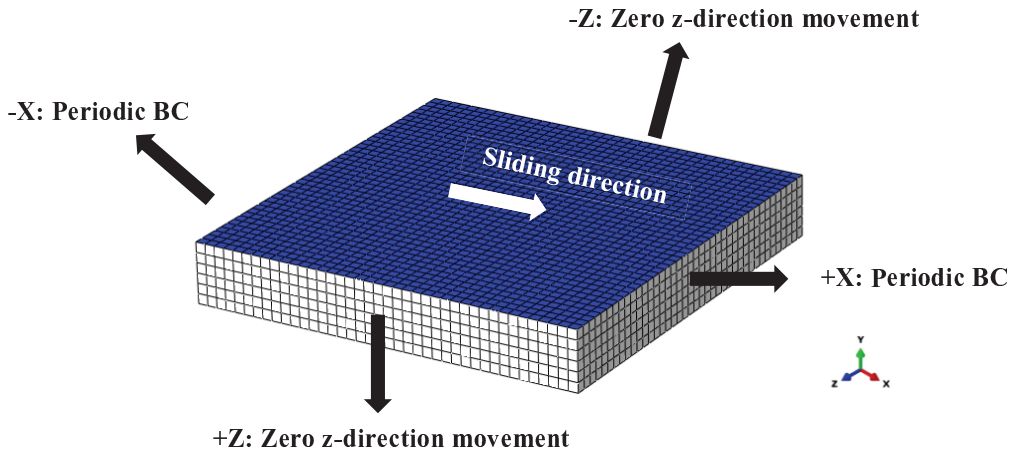


Figure 24: Three-dimensional friction simulation mesh (workpiece)

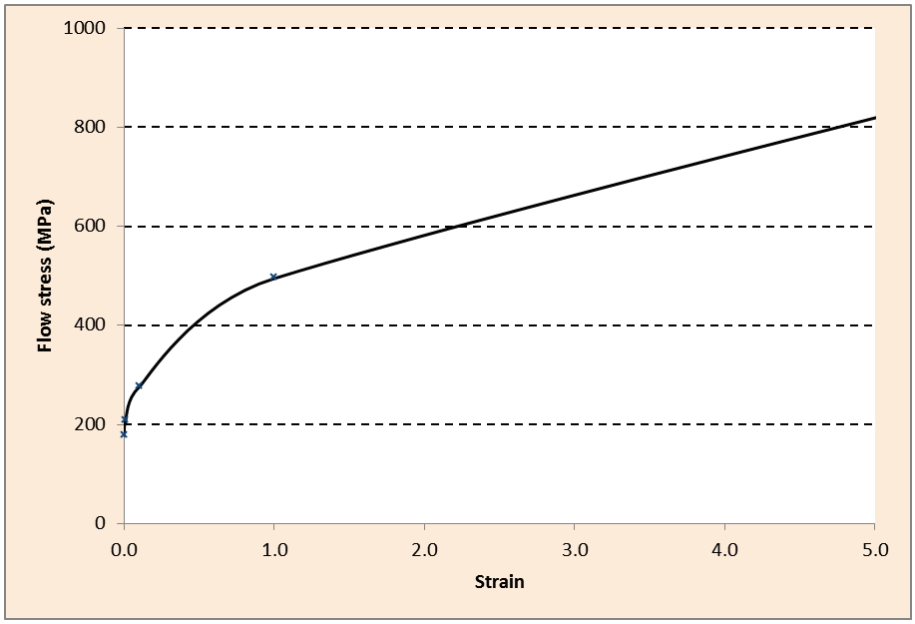


Figure 25: Stress-strain relation used in surface texture simulation

In the simulation, the textures are treated as fully periodic as such it is possible to simulate only the unit texture. The periodicity of the texture will further be implemented through three-directional tie constraints throughout the sides of the mesh to ensure that any loading is translated periodically.

## 3.4 Depth-dependent Stress-Strain Relation

FE analysis code Abaqus and the material property from Figure 25 will also be used in this part of the study. However, as the DSS relation requires depth-dependent material property defined in the mesh, mesh with higher thickness to width ratio was needed in order to capture the effect of the 'hardness layers' in the simulation. The mesh used will be presented in Chapter 6.

The following assumptions are considered in simulations throughout Chapter 6 on depth-dependent stress-strain simulation:

- Material is considered as continuum, isotropic and depth-dependent.
- Standard contact formulation of penalty method in Abaqus is used. Real surface with asperities is prescribed directly in the model.
- No additional friction behaviour is introduced to the model; ploughing is the only friction mode.
- These non-simulated behaviours are considered to have no or insignificant effect on the results: heat generation due to friction, material delamination (wear and galling).

# CHAPTER 4 FRICTION TEST FOR MICROFORMING

## 4.1 Background

Currently, there is no setup designed specifically to study the friction behaviour in microforming. Studies have been done using friction tests established to examine friction behaviour at larger size such as demonstrated by Geiger et al. [1]. As these tests are scaled down, fabrication of tooling for the friction test can be deemed impractical and unreliable as the production of miniature intricate tooling with precision is both labour- and cost-extensive [95]. In the same fashion, fabrication of specimen, handling and examining the results of the test also become major difficulties. This chapter proposes a friction test setup designed specifically for microforming applications. The conception of this test will be useful as quick tool to examine the amount of friction involved in specific workpiece-tooling interaction, including the influence of the interface (lubricant, surface features, etc.). This set-up is aimed to serve as an industrial solution of studying friction behaviour in microforming. In addition, the test can be used to perform more rigorous research on friction behaviour in microforming.

## 4.2 Development of New T-Shape Test

### *4.2.1 Plane strain T-Shape test*

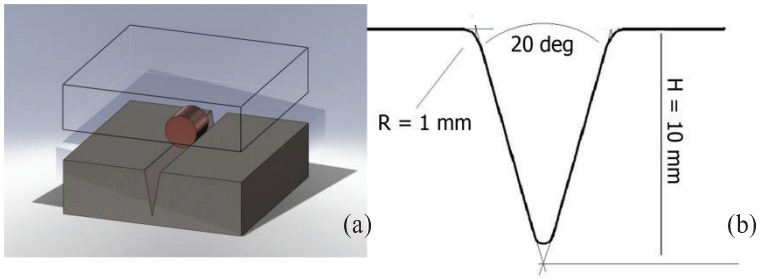


Figure 26: (a) Illustration of setup, and (b) Die geometry of T-Shape test

The T-Shape test [116] (Figure 26) was originally proposed as friction test for cold forging application because it was claimed to have the following advantages:

1. Sensitivity of load-stroke curve and the shape of the finished workpiece to friction,
2. High contact pressure and large surface expansion,
3. Unlike DCET, only radial surface is in contact with punch and die,
4. Due to the simple geometry, the handling of miniaturized specimen is easier, the die can be manufactured more quickly and less costly, and oil lubrication can be done more easily for evaluation of lubricants.

The T-Shape test is proposed as a suitable friction test for microforming application because of the simple geometry of the workpiece (a cylinder) for easy fabrication, the high surface expansion, and also the self-aligning nature of the workpiece into the die which reduces handling difficulty.

However, the original 1:1 cylinder aspect ratio poses handling and fabrication problem when the original T-Shape test diameter of 7 mm is scaled down to 1 mm.

Consequently, the T-Shape test for microforming is proposed to have higher length to diameter ratio, in this case it was set to length of 5 mm and diameter of 1 mm to aid handling of workpiece and allow greater tolerance on the length of specimen to avoid the need for precision tool for sample preparation. This workpiece size is still within the context of microforming as it has two dimensions measuring 1 mm. Although the length of 5 mm is maintained throughout the current study, the workpiece aspect ratio may be increased further to simplify the FE modelling (e.g. length/diameter equal to or higher than 10 as illustrated in Figure 27 (a)) as the high length/diameter value restrains the material flow lengthwise, thus plane strain assumption can be made.

The problem with the characterisation approach in the original T-Shape design lies with the measurement –measurement of protrusion height for a particular load. It is understood from microforming investigation and strain gradient plasticity that the mechanical properties of the surface region can be different from that of the bulk region. That means, even if there is no change in friction, the same normalized load will give different normalized protrusion height depending on the proportion of surface grains and bulk grains.

Instead, the protrusion height should be measured against the process stroke (or punch displacement). In practice, however, the measurement of stroke is impractical because the stroke is small in comparison to the machine travel (precision limit) and also the equipment undergoes elastic deflection under loading (rigidity limit).

The T-Shape test is considered a bulk (or massive) metal forming and hence elastic recovery upon unloading is usually negligible. Therefore, the test can be characterised by comparing the “total height” and the “flange height”. These terms are illustrated in Figure 27 (b). With this characterisation approach, flange height is an alternative way

to express the stroke without having to compensate elastic deflection of the equipment.

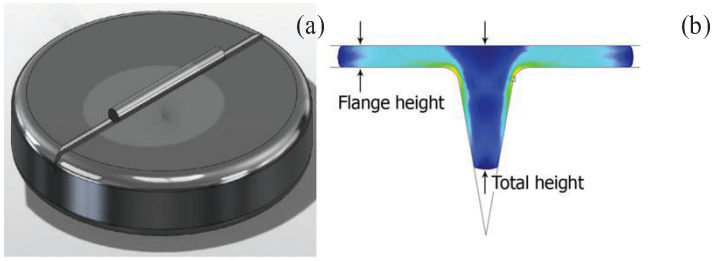


Figure 27: (a) Plane strain T-Shape, and (b) T-Shape geometry

The sensitivity of the original T-Shape test die was evaluated using DEFORM 2D in plane strain simulation. Despite the aspect ratio of 5, plane strain simulation was performed to minimize calculation time in the early stage of development. It is understood through initial simulations that the friction sensitivity increases with higher workpiece aspect ratio. Therefore, the plane strain simulation is treated as the best-case scenario with adequate accuracy.

The stress-strain curve of the ETP Copper has been provided in Figure 20. This data was then used as input for the DEFORM 2D simulation, using rigid bodies for the dies, and plastic material model with around 2000 elements for the workpiece. The simulation results using the original T-Shape geometry and without considering the size effects are shown in Figure 28. The simulations were performed across a range of constant shear friction factors between $m = 0$ and $m = 0.3$.

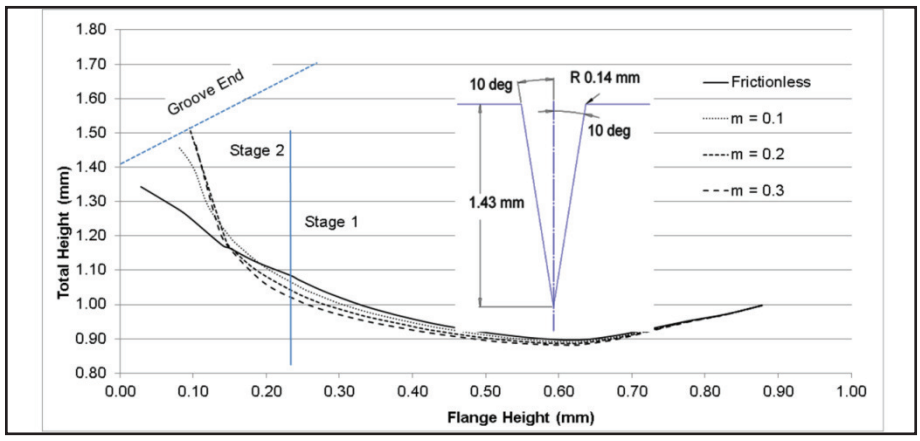


Figure 28: Evaluation of original T-Shape die. Insert: Die geometry

The die is scaled down in this simulation to keep the relative size of the workpiece and die constant. As the test progresses, the distance between the top and bottom dies reduces. This distance further becomes the flange height as the flange will be trapped between the dies. Therefore, examining Figure 28 from right to left, it is shown that during the initial stage of the test, between flange height 0.89 and 0.60 mm, the total height decreases. The total height then starts to increase slowly between flange height 0.60 and 0.23 mm. This shows that in Stage 1, the material prefers to flow as the flange instead of into the die groove because of the friction at the die groove. The metal flow is therefore called protrusion-limited and consequently, the protrusion and subsequently *total height is lower for high friction simulation in Stage 1*. During the subsequent stage, or Stage 2, the large amount of material pile up between the flat portion of the die and the punch creates friction which restrains subsequent the material flow towards the flanges, forcing the material now to flow into the die making the Stage 2 flange-limited and in contrast to Stage 1, *total height is higher for high friction simulation in Stage 2*.

Observing Figure 28, clear separation of behaviour from the different friction coefficient can only be seen starting from flange height 0.15 mm (0.05 mm to 0.15 mm flange height, for 1 mm workpiece) or later at the flange-limited Stage 2. Moreover, only negligible distinction can be made between friction coefficient 0.1 and higher. Therefore, the die design for the plane strain T-Shape test was modified.

### *4.2.2 Two-slope T-Shape die (T-Shape A)*

Upon examining the FE simulation, it is understood that the clear distinction of material flow produced from the different friction coefficients can only be realized at Stage 2 and that Stage 1 should be minimized to increase the distinction. It was found that wider groove opening allows more material to flow into the die and reduce unwanted outward material flow, i.e. making the test more flange-limited overall. This geometry modification has been documented by Taureza et al. in 2010 [120].

The evaluation of the two-slope die design is presented in Figure 29. The wider groove opening in the two-slope design allows Stage 1 to be suppressed and give better distinction between the friction coefficients at Stage 2. In addition, the die design produces more separation between the friction curves. The only limitation is the limited stroke since the material flow reaches the bottom of the groove, and further stroke will not produce further protrusion.

In the simulation with the T-Shape A geometry especially for frictionless condition, there is a notable trend of hesitation (increase-decrease, highlighted by the dotted rectangle) in total height for both Stage 1 and Stage 2 in the test. As the test is a competition between upsetting and extrusion flows, the directionality of material flow is highly dependent on the amount of friction hindering both flows. However, in the

absence of friction, this material flow direction is attributed solely to how much strain hardening is experienced at the front of the upsetting and extrusion flow. The material flow preference may therefore shift repeatedly due to the very similar strain pattern at the flow fronts.

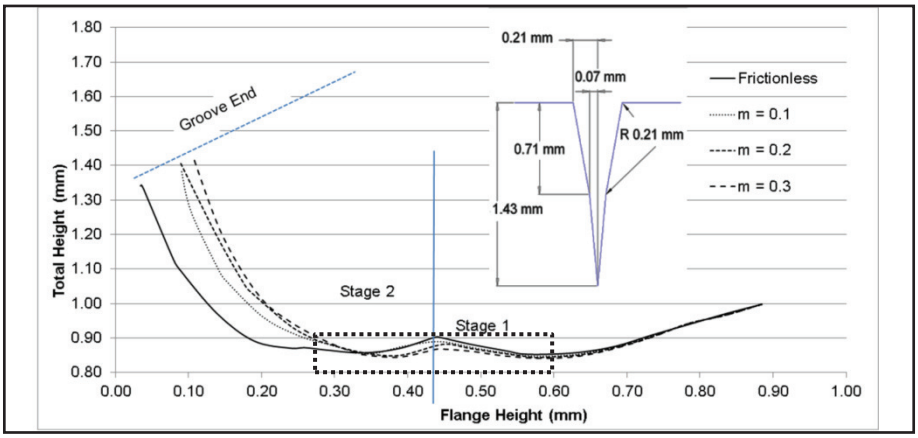


Figure 29: Evaluation of T-Shape A. Insert: Die geometry

### *4.2.3 Die with vertical wall (T-Shape B)*

To avoid having limited protrusion as the material reaches the bottom of the groove, a vertical groove wall was further proposed. By changing to vertical wall, the distinction between different friction curves was further increased, as illustrated in Figure 30. Since the top portion of the groove remains similar to the T-Shape A, the behaviour of the material flow remains similar in Stage 1. In Stage 2, the vertical groove allows more protrusion to take place, and create distinction between material flow behaviour associated with the magnitude of friction.

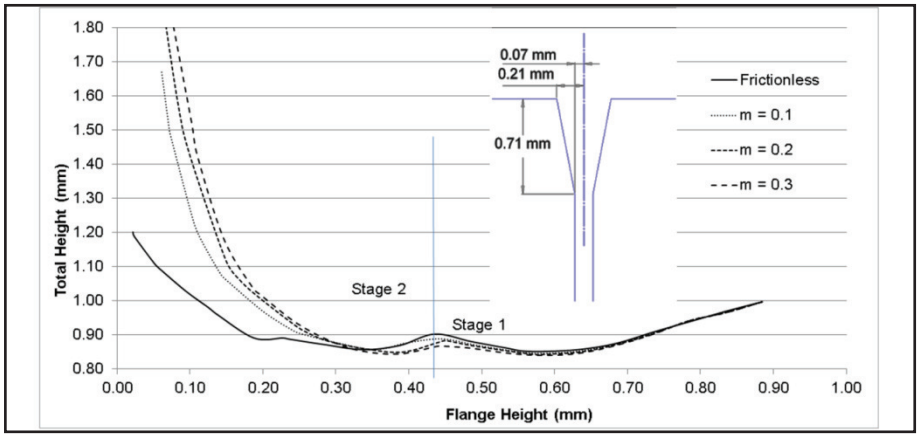


Figure 30: Evaluation of T-Shape B. Insert: Die geometry

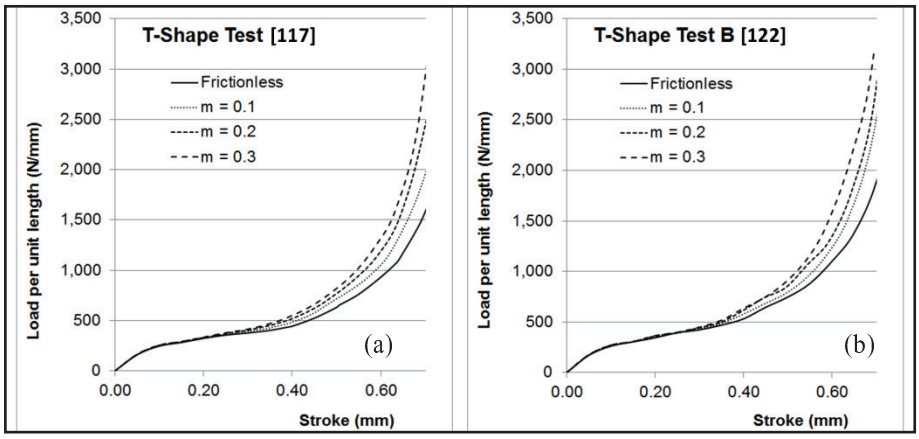


Figure 31: Process load comparison: (a) Original T-Shape die (b) T-Shape B [121]

The process load was also evaluated and compared between T-Shape B and the original T-Shape die, as shown in Figure 31. The process load is increased by up to 18% for frictionless condition, and even higher for when friction exists. Although this means higher press machine requirement for the test, the distinction between process loads from different friction coefficients are also increased; this is desirable.

From these results, it was decided that T-Shape B geometry would be most suitable for microforming friction test, and will be referred to in the following sections as microforming T-Shape test. This setup was then fabricated to evaluate the actual performance of the T-Shape test in distinguishing different friction conditions.

## 4.3 Design of the microforming T-Shape Test

### *4.3.1 Test setup*

For the experiment, the microforming T-Shape test assembly was fitted on Schmidt Servo Press 420. The assembly was fabricated using Hitachi Steel SLD Magic. SLD Magic is developed to give a good hardenability for cold working applications as well as machinability closer to free machining steel.

The assembly consisting of four components was proposed. The forming die was designed as split dies. This design eases fabrication and control of surface finish and surface treatment (e.g. texturing, coating, heat treatment), eases removal of finished workpiece without introducing unwanted additional strain, as well as allows post-test investigation (e.g. residual lubricant film, wear scar, galling).

The split dies are compression fitted using screws as illustrated in Figure 32 to compensate the pressure exerted during loading and avoid elastic deflection (see Figure 33). The assembly in Figure 32 consists of the two die halves (left) and the die container with multiple screws to provide the compression fit (centre) which combine as shown (right).

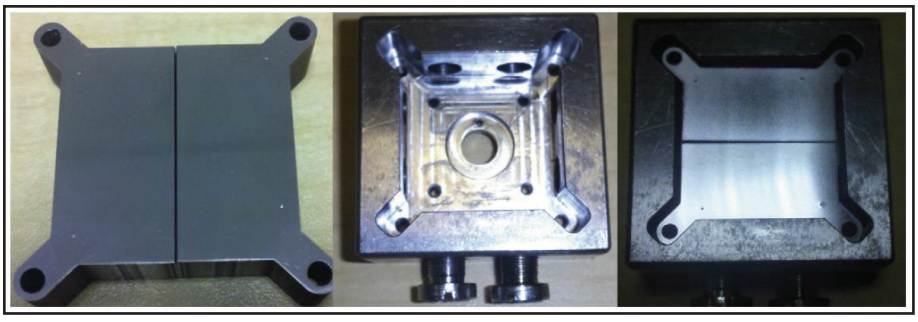

Figure 32: Illustration of T-Shape assembly

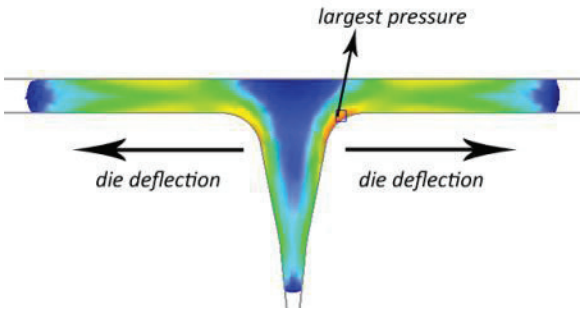


Figure 33: Illustration on die deflection

The microforming T-Shape test apparatus was originally designed with compression fitting cone (Figure 34 (a)) which contains the conical T-Shape dies (Figure 34 (b)) so as to provide easier loading mechanism with only one fastener in the apparatus. However, this design was not found to be robust because: a) it requires very high degree of precision in producing the angle of the cone for both the dies and the container to provide the compression fit, and b) the large circumferential compression fitting face requires large force to produce the same amount of fitting pressure.

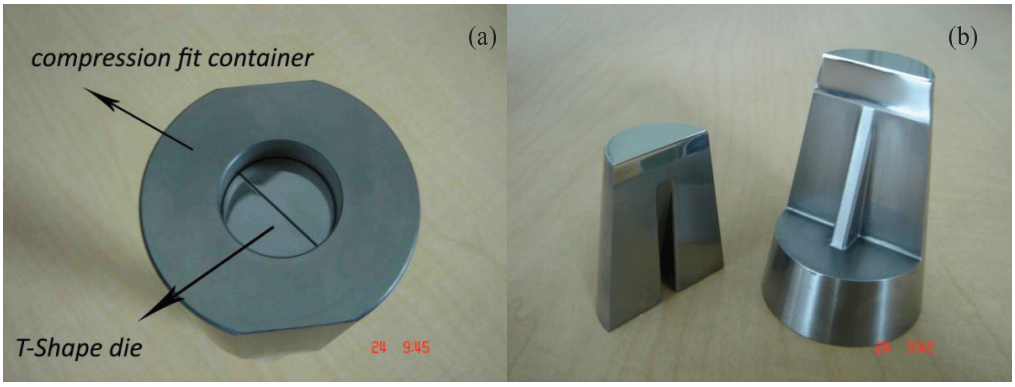


Figure 34: Compression fitting cone originally used

### *4.3.2 Ideal case*

Two die geometries would be highlighted in this section: the original T-Shape die [116] geometry (scaled to work with 1 mm specimen) and microforming T-Shape test.

Measurements (see Figure 27 (b)) can be done at several stroke position (and thus flange height) and the corresponding total heights can be measured directly. The data pairs (total height and flange height) obtained from the experiment are then treated as discrete data points for comparison with the simulation results.

Figure 35 shows the calibration curves obtained from simulation for the original T-Shape design with workpiece size of 1 mm. The calibration curves were produced for friction factor 0.3 and lower. This range of friction factor is considered as the target friction factor for metal forming. The calibration curves were drawn only for flange height smaller than 0.30 mm in order to highlight the Stage 2 of the test. Flange height of 0.11 mm was determined to be the ideal measurement point as it is the region with highest resolving capability, i.e. the flange height which produces largest separation between the calibration curves (see Figure 35 and Figure 36).

In order to better explain the resolving capabilities of both the original T-Shape test and the microforming T-Shape test, several temporary variables are introduced. It can be seen from Figure 35 that the total height, *t*, developed during the test can be represented as a function of friction factor, *m*, and flange height, *f*. If all specimens were to be characterized at exactly 0.11 mm, the total height during the test can be simplified to be just a function of *m*. The variable $t_m^*$ is introduced as the total height using the original T-Shape test geometry at ideal measurement point and with friction factor, *m*.

It is desirable that the change in *m* during the test is translated into a large change in $t^*$ which corresponds to higher friction sensitivity. For this reason, another variable $\delta_{m_1}^{m_2}$ may be introduced as governed in Equation 3.1 which is defined as the separation

distance between *t* from two *m* values. The complete tabulation is presented in Table 4 and Table 5.

$$\delta_{m_1}^{m_2} = \left| t_{m_1}^* - t_{m_2}^* \right| \qquad 3.1$$

However, at flange height 0.11 mm, the test can only distinguish friction factor *m* up to 0.2. Because of the design, the development of total height was also limited by the groove depth (dotted line marked Groove End).

Similar plot is drawn for microforming T-Shape test (Figure 36). With the microforming T-Shape design, the region with the highest resolving capability is at flange height of 0.08 mm. The total heights obtained by the original and microforming T-Shape test at different friction levels are summarised in Table 4. It can be seen from Table 4 that the microforming T-Shape test is able to produce a larger spread of total heights from the various levels of friction factor. This larger spread translates into larger separations between the curves which are essential since it will determine what metrology equipment should be used in the experiment. The test with wider separation between the curves is therefore deemed more friction-sensitive. For the microforming T-Shape test, the variables $\delta_{m_1}^{m_2}$ and $t_m^*$ are replaced by $\delta'^{m_2}_{m_1}$ and $t'^*_m$, respectively but the formula remains similar (Equation 3.2). The complete tabulation is presented in Table 4 and Table 5.

$$\delta'^{m_2}_{m_1} = \left| t'^*_{m_1} - t'^*_{m_2} \right| \qquad 3.2$$

The last temporary variable of Performance Index ($PI_{m_1}^{m_2}$), which is defined as the improvement brought on by the change in test geometry is governed by Equation 3.3 and the full tabulation is presented in Table 5.

$$PI_{m_1}^{m_2} = \frac{\delta'^{m_2}_{m_1}}{\delta^{m_2}_{m_1}} * 100\% \qquad 3.3$$

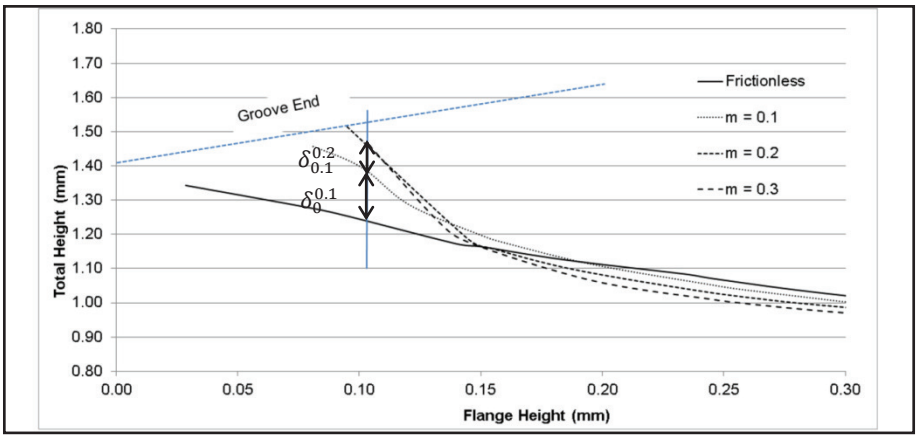


Figure 35: Friction curves for the original T-Shape test

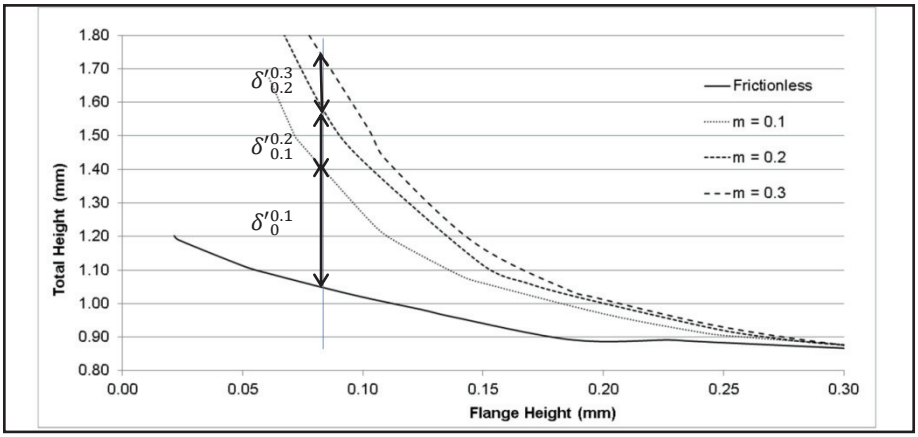


Figure 36: Friction curves for microforming T-Shape test

Table 4: Total heights at various friction levels

| Friction Factor | Total Height[1] Original T-Shape ($t^*_m$) | Total Height[2] µforming T-Shape ($t'^*_m$) |
|---|---|---|
| Frictionless ($m$ = 0) | 1.23 mm | 1.05 mm |
| $m$ = 0.1 | 1.38 mm | 1.40 mm |
| $m$ = 0.2 | 1.45 mm | 1.56 mm |
| $m$ = 0.3 | 1.45 mm | 1.73 mm |
| | [1] Measured at flange height 0.11 mm | [2] Measured at flange height 0.08 mm |

Table 5: Performance Index of microforming T-Shape test

| Comparison Between: | Separation Original T-Shape[1] ($\delta^{m_2}_{m_1}$) | Separation µforming T-Shape[2] ($\delta'^{m_2}_{m_1}$) | Performance Index $PI^{m_2}_{m_1}$ |
|---|---|---|---|
| $m_1$ = 0 AND $m_2$ = 0.1 | 0.15 mm | 0.35 mm | 233% |
| $m_1$ = 0.1 AND $m_2$ = 0.2 | 0.07 mm | 0.16 mm | 229% |
| $m_1$ = 0.2 AND $m_2$ = 0.3 | 0 | 0.17 mm | ∞ |
| | [1] Measured at flange height 0.11 mm | [2] Measured at flange height 0.08 mm | |

In the actual experiment using microforming T-Shape test, the geometry measurement of the tested specimen does not have to be measured exactly at the flange height 0.08 mm. Instead, it is advisable to have at least 3 specimens for each friction condition and have the specimens to be pressed to different flange heights (in the range between 0.05 mm and 0.20 mm) and then compared against the friction curves from the simulation.

## 4.4 Effects of Deviation in Material Properties and Die Geometry

### *4.4.1 Deviation in material properties*

In order to fully examine the suitability of the modified T-Shape test as microforming friction test, a series of more thorough simulations was done considering the effects of possible scatter in material properties as well as die inaccuracy. The objective of this examination is to determine whether the influence of the variation in material properties shows any significance in comparison with the change in experimental results due to changing friction conditions. The mechanical properties of 90% and 110% flow stress from Figure 20 were considered as possible variation of mechanical properties.

Figure 37 presents the metal flow and forming load predictions from simulation using the three different mechanical properties in microforming T-Shape test. For each mechanical property, two friction conditions were simulated –frictionless and friction factor, $m = 0.3$. In the microforming T-Shape test, the forming load (see Figure 37 (a)) is directly affected by the mechanical property of the workpiece. However, the preference of metal flow direction is non-responsive to 10% change of mechanical properties as illustrated in Figure 37 (b) in which the distinction in calibration curves is only apparent when the friction is changed.

Ultimately, despite the possible mechanical properties variation from one workpiece to another, users of T-Shape test would have the confidence and capability to distinguish friction effect from material effect in the test results. However, when testing new material and hence the mechanical properties from the new material is beyond the 10% properties deviation, unless the friction test is proven non-sensitive to

the change of material properties, new calibration curves should be produced especially for materials with high strain hardening property as strain hardening significantly alters strain and contact pressure distributions [92].

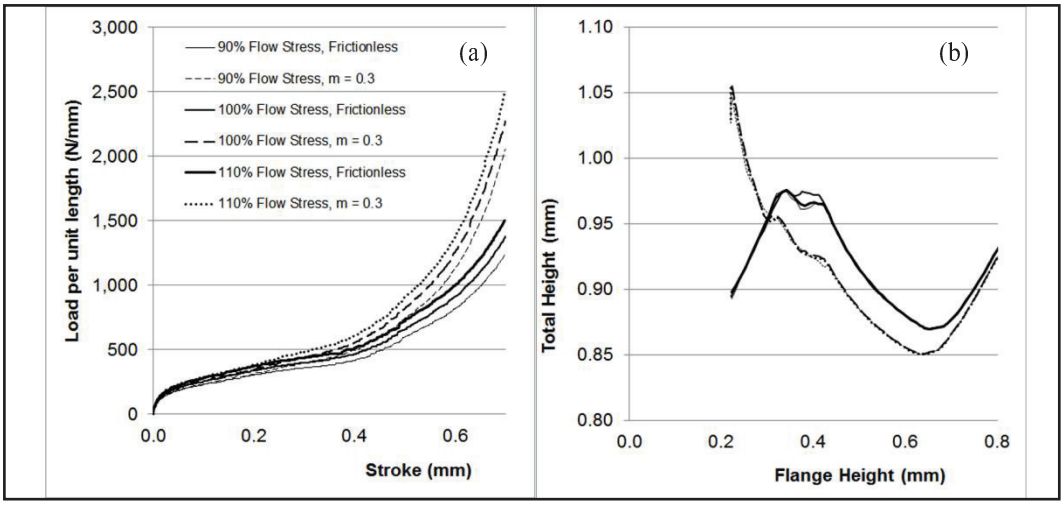


Figure 37: Effect of material properties to T-Shape test

### *4.4.2 Deviation in die geometry*

The geometry of microforming T-Shape test has been proposed for microforming friction investigation and it has been indicated by simulation to produce improved friction sensitivity (Table 5) and it is able to distinguish friction effect from material variation effect (Figure 37). However, it is equally important to examine the test's sensitivity to deviation in die geometry. This step is important in determining the allowable non-conformity in die fabrication. Generally, when tooling geometry is produced within a specific tolerance, the deviation of results because of the geometry deviation should be insignificant or non-existent. In short, the deviation of the results due to geometry deviation should be smaller than the accuracy of the measurement tool and the process scatter.

Ideally, T-Shape design uses 0.21 mm of half-die opening (D) (see insert of Figure 30), and 0.1 mm corner radius (r). However, it is necessary to define acceptable tolerance for the die design. More simulations were run to examine the influence of tooling inaccuracy use the typical tolerances of ± 0.01 mm and 0.05 mm (10 and 50 μm respectively, see Table 6). Moreover, larger value of r was also used to illustrate the behaviour when the corners of the tooling are over-polished.

Table 6: Nomenclature of different simulation settings (Tooling inaccuracy)

| | | D (mm) | | | | |
|---|---|---|---|---|---|---|
| | | -0.05 (0.15) | -0.01 (0.20) | 0.21 | +0.01 (0.22) | +0.05 (0.26) |
| r (mm) | 0.1 | **D--** | **D-** | **N** | **D+** | **D++** |
| | 0.2 | N.A. | N.A. | **r+** | N.A. | N.A. |

Generally, larger tolerance is desirable to reduce the difficulty of tooling fabrication to reduce fabrication cost. However, large inaccuracy would result in ineffectiveness of the friction test as shown in Figure 38.

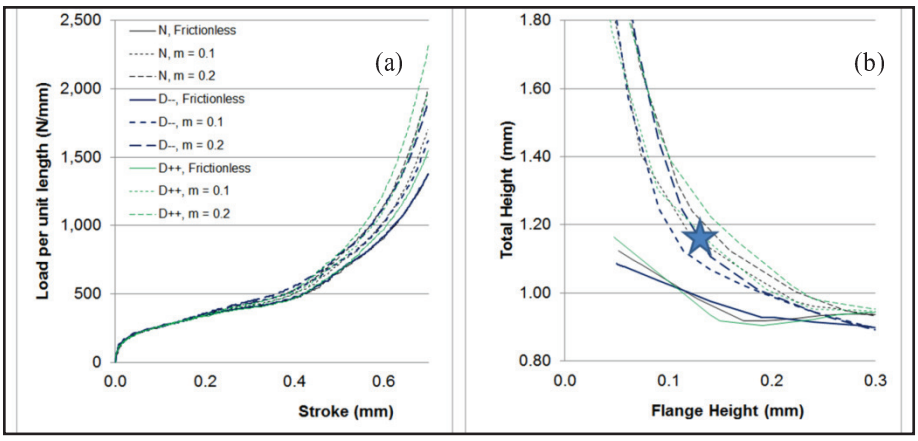


Figure 38: Effect of D to microforming T-Shape test (larger tolerances)

Tolerances of ±0.05 mm were considered unsuitable as they strongly affect the test results. Although the load for the case of D-- does not deviate as significantly as D++ (from the case of N, Figure 38 (a)), the geometry development during the test is influenced strongly for both D++ and D-- (see Figure 38 (b)). In addition, the curves in Figure 38 (b) have overlaps and crossovers, as marked with star, especially between friction factors of 0.1 and 0.2. Overlaps and crossovers are undesirable as these points may cause misinterpretation of results.

Simulations with 0.05 mm tolerance suggest that the fabrication of the test setup should use even tighter tolerance. Thus, more simulations were performed using ±0.01 mm (10 μm) tolerances (Figure 39). Figure 39 illustrates the behaviour of the test using 0.01 mm tolerances.

At 0.01 mm tolerances, the loads do not deviate significantly as shown in Figure 39 (a). In addition, the influence of tolerances to the geometry evolution is only restricted at the Stage 1 of the T-Shape test, and the curves converge within the measurement window (small flange height, see Figure 39 (b)). Hence 0.01 mm tolerance is deemed to be the suitable tolerance value for fabrication.

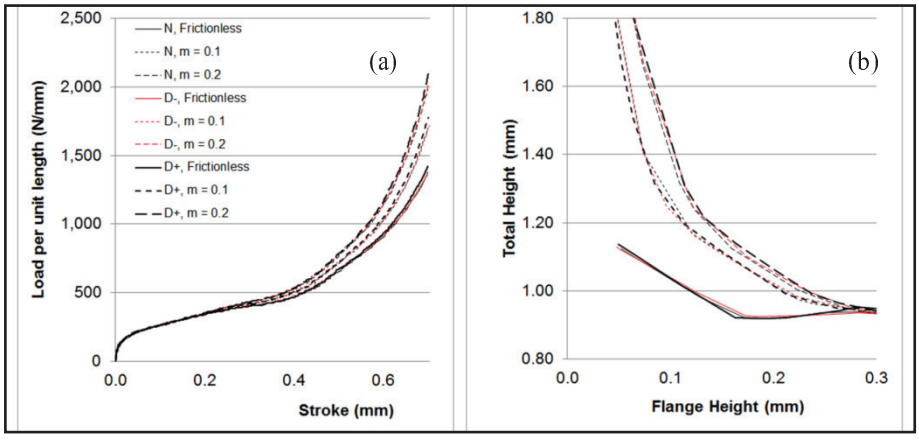


Figure 39: Effect of D to microforming T-Shape test (smaller tolerances)

The reproduction of accurate corner radius also requires extra attention. Over-polishing would result in larger corner radius than expected, and is more significant as specimen size becomes smaller.

The simulation results show that the effect of changing the corner radius can change the test behaviour significantly (see Figure 40). Thus it is important to keep the tolerance of the corner radius very tight (possibly to 0.01 mm) to guarantee the performance of the test setup.

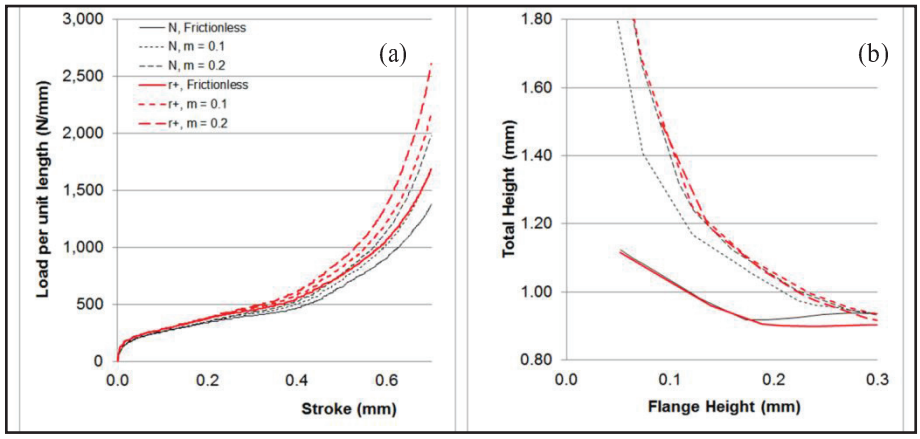


Figure 40: Effect of r to T-Shape test

## 4.5 Experiments with Different Materials

Experiments were conducted on Schmidt Servo Press 420. The workpiece materials were produced by cutting from 1 mm diameter reel of 99.5% as drawn Al wire, 99.99% annealed Ag wire and as drawn ETP Cu wire. The three materials were selected as they have common crystal structures and therefore can be considered to have similar deformation patterns. In addition, these materials have been identified to have industrial value for micro manufacturing, i.e. lightweight structures, crafts and jewellery, and electronic, respectively.

As the workpiece being used has the aspect ratio of 5, it is more appropriate to present the experimental results alongside quarter-workpiece Deform 3D implicit simulation (approximately 30,000 elements) since plane strain assumption would not be accurate when comparing simulation and experimental results. Friction sensitivity simulations were performed to produce the calibration curves. Symmetry boundary conditions as illustrated in Figure 41 were prescribed on the symmetry planes as the four quarters of the workpiece are assumed to deform uniformly and the resource saved can be used to allow finer meshing to capture higher deformation details. During the simulation, the die is fixed as a rigid body and the also rigid punch is prescribed with a movement to -Y direction to compress the specimen and let the specimen develop the total height which depends highly on friction.

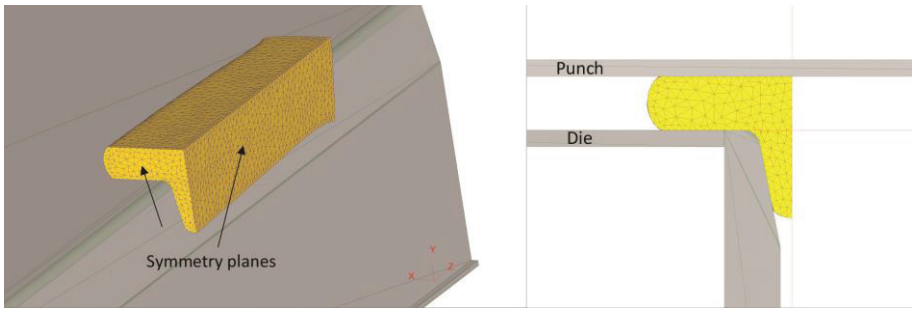


Figure 41: 3D quarter-workpiece T-Shape test simulation at 0.6 mm stroke

The multi-material experiment was conducted to examine its effectiveness in distinguishing friction conditions for changing workpiece material. This experiment also looked for secondary evidence of high friction such as galling, which is the presence of transfer layer of workpiece material to the tooling surface. In the experiment, the measurement of the total height was taken at the mid-length of the cylindrical specimen.

It was also discovered that despite the change in material from Al to Cu (material properties presented in Figure 22), the calibration curves generated through the 3D simulation are identical. This supports the salient point in T-Shape test –the non-responsiveness of the calibration curves to some extent of mechanical properties variation. Such material property non-sensitivity is a preferred virtue of a friction test, which is also demonstrated by the ring compression test commonly used in the metal forming industry practice. Consequently, there is also no need to supply accurately the stress-strain relation for Ag and the calibration curves are assumed to be universal for metal.

As it is inconvenient to create calibration curves for all values of friction factors, the current calibration curves are limited to increment of 0.2 (i.e. 0.2, 0.4, 0.6 and 0.8). However, intermediate values of appropriate friction factors can be well estimated by adapting the available constant-m calibration curves to the regression function proposed here (Equations 3.4 and 3.5). In the equations, $t$, $f$ and $m$ refer to the total height, flange height (both in mm) and constant shear friction factor, respectively. Meanwhile, $f(m)$ is a function of $m$ (Equation 3.5) introduced merely for more readable presentation. Exponential Equation 3.4 is chosen as the regression function as the correlation between the variables $t$, $f$ and $m$ exhibits exponential relationship.

The constants were determined from the available calibration curves as C1 = 0.6435, C2 = -0.1872 and C3 = -0.1973. The chosen constants resulted in correlation coefficient $R^2$ value of 0.9985, 0.9985, 0.9989 and 0.9977 for $m$ value 0.2, 0.4, 0.6 and 0.8, respectively, which indicated very good agreement between the simulation result and the fitting from the regression equation. Overall, the known range of

achievable friction factors in metal forming, i.e. 0 to 1.0 based on pioneering work by Hartley et al. (1979) and Bay (1987), is well represented and fitted by the function.

$$t = C_1 f^{f(m)} \quad 3.4$$

$$f(m) = C_2 + C_3 m \quad 3.5$$

Using Al workpiece (Figure 42) and Equations 3.4 and 3.5, the T-Shape test returned the friction factor, *m*, of 0.910. This value is in agreement with Figure 42 in which the modus of the data points from the experiment lies upward of the friction calibration curve *m* = 0.8. This high friction factor was supported by the presence of galling mark on the T-Shape die after the experiment (Figure 43). During the development of sheet galling test, Bernick et al. [122] concluded that high static and dynamic friction stress are usual indicator for galling. Although exceptions have been observed [123], galling generally increases friction as it worsens the tooling surface.

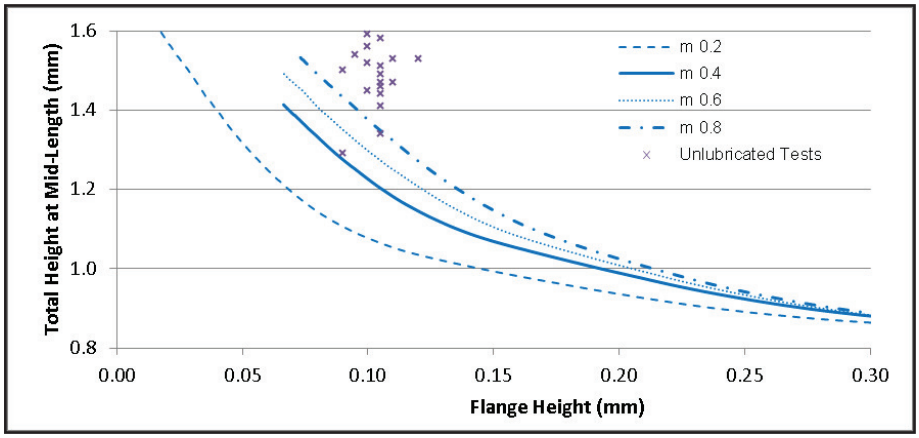


Figure 42: Unlubricated Al experiment results

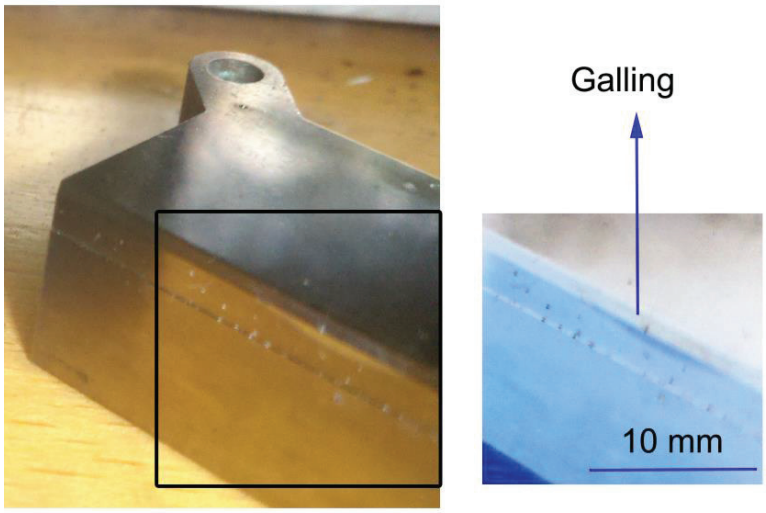


Figure 43: Positive and negative images of the die galling

The work by Schedin [124] supports that galling is a frequent occurrence in Al sheet forming. The galling of Al compound is known to become more severe when Aluminium oxide is present. Aluminium (III) oxide compound is known to form spontaneously at room temperature on pure Al surface and hence the dull appearance of Al piece. The aluminium is the only material which produces galling in the experiment and it is consistent with the experiment results using Ag which returned lower friction factor value of 0.370 as presented in Figure 44.

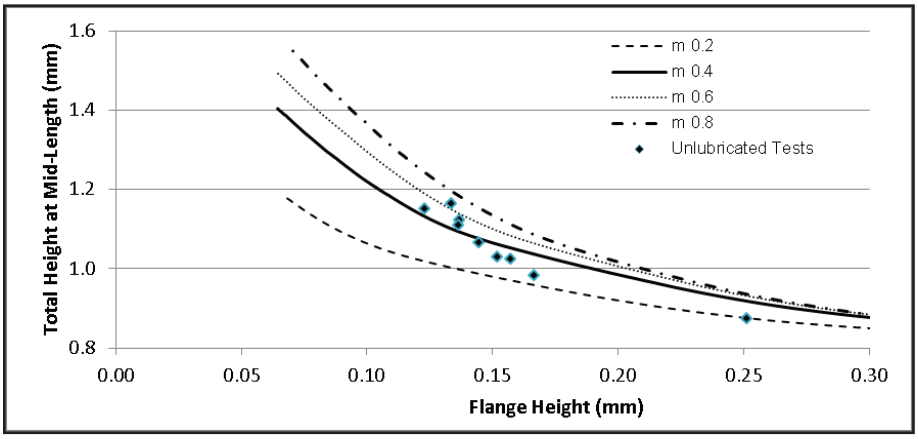


Figure 44: Unlubricated Ag experiment results

The Cu experiment resulted in friction factor $m$ = 0.473. In metal forming processes, the shear strains due to deformation inevitably drive the development and evolution of crystallographic texture. Similarly in the current investigation, the texture of the specimen before and after the T-Shape test was analysed to identify the deformation mechanism of the test. Axisymmetrically deformed FCC metals would produce <111> + <100> fibre texture at the centre region of the wire associated with the homogeneous deformation, and a circular texture from the shear deformation. The experimental results are in good agreement with fibre texture on <111> plane and <200> plane, as well as weak circular texture on <220> plane for the copper specimen before the T-Shape test (Figure 45). Figure 46 shows that there was no significant texture change during the T shape test deformation. This is mainly due to the majorly plane strain deformation mode which is characteristics of this test.

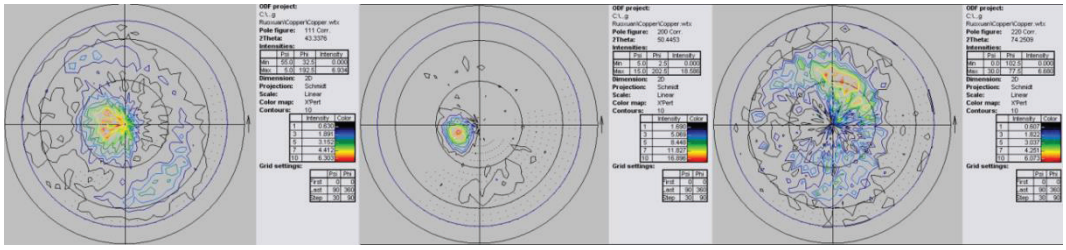

Figure 45: Pole figures pre-experiment for <111>, <200> and <220> planes

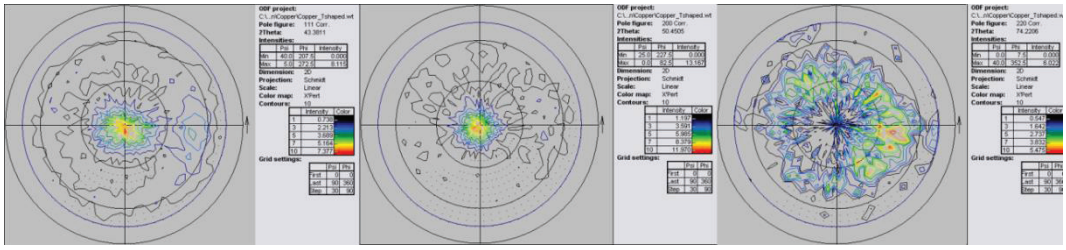

Figure 46: Pole figures post-experiment for <111>, <200> and <220> planes

It was also noted that galling was not visible from naked-eye observation for Ag and Cu workpiece. The multi-material examination using T-Shape test provides the evidence that T-Shape test is able to distinguish friction conditions and when friction is high, galling was observed to further support the test's findings.

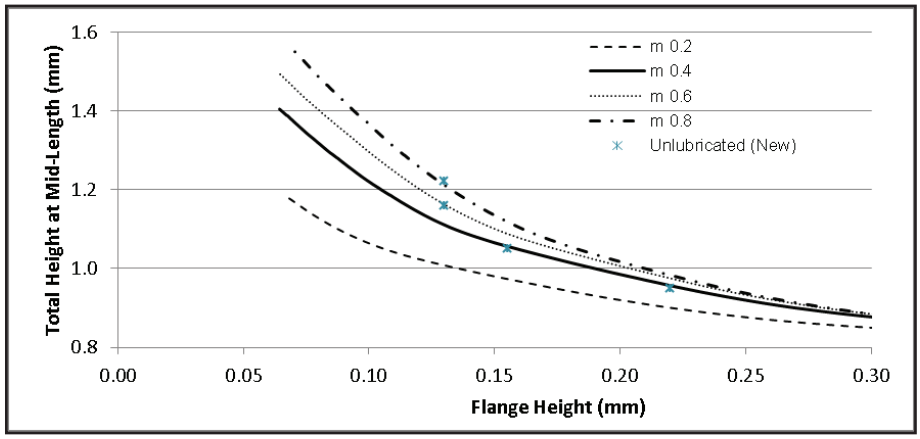


Figure 47: Unlubricated Cu experiment results

## 4.6 Experiment with Different Lubricants

Further experimentation was conducted using multiple lubricants to further promote the use of the T-Shape test for friction investigation in microforming. Specifically, the experiment was aimed to explore the friction size effect and its implications when different types of lubricants were used.

All the lubricants were designed for metallic contacts such as machining, sheet forming and forging. The lubricant evaluation was done only for copper and aluminium material as these materials are of high demand in microforming industry and they provide contrast in friction behaviours in the unlubricated studies, i.e. higher friction ($m$ = 0.910) by aluminium and lower friction ($m$ = 0.473) by copper. The lubricants used (both commercially available and prototype) can generally be categorised into three groups based on the method of application: a) Aerosol spray, b)

Liquid applied directly to the surface and c) Liquid supplied to surface followed by (non)-heated drying to expose the dried lubricant film (see Table 7). The split die of the T-Shape test allows lubricants to be coated with greater consistency when it is desired.

In the current experiment, the lubricants were supplied in abundance to ensure complete coating of the surfaces prior to deformation. The lubricated experiments were conducted in the same way as the unlubricated experiments in order to acquire specimens with various flange heights between 0.05 mm and 0.30 mm. The data points from the total height and flange height measurements were superimposed on the friction calibration curves as well as in the mathematical function to obtain their friction coefficients.

Table 7: Lubricants used in multi-lubricant experiment

| Name | Application | Composition or Intended use |
|---|---|---|
| *D1X (Prototype)* | *Dried Film* | *Water (81%), wax (8%), sodium stearate* |
| *D2X (Prototype)* | *Dried Film* | *Water (62%), isophthalic acid (18%), wax (8%), graphite* |
| D3 (Commercial) | Dried Film | Sheet metal forming (warm), water-based lubricant |
| L1 (Commercial) | Liquid | Machining, water-based lubricant |
| L2 (Commercial) | Liquid | Forging, oil-based lubricant |
| *L3X (Prototype)* | *Liquid* | *Vegetable oil (85%), surfactants (15%)* |
| L4 (Commercial) | Liquid | Sheet metal forming, oil-based lubricant |
| A1 (Commercial) | Aerosol Spray | Graphite |
| A2 (Commercial) | Aerosol Spray | $MoS_2$ |
| A3 (Commercial) | Aerosol Spray | PTFE |

### *4.6.1 Aerosol spray lubricants*

Figure 48 presents the results from aluminium experiments using aerosol spray lubricants. Out of the three spray lubricants, A3 performed the best ($m$ = 0.375) followed by A2 ($m$ = 0.546) and A1 ($m$ = 0.694). All $m$ values were calculated using Equations 3.4 and 3.5. This result is confirmed by the work by Gong and Guo with diamond-like carbon lubricant in which solid lubricants are more effective in reducing friction than liquid lubricants which are prone to friction size effect [125].

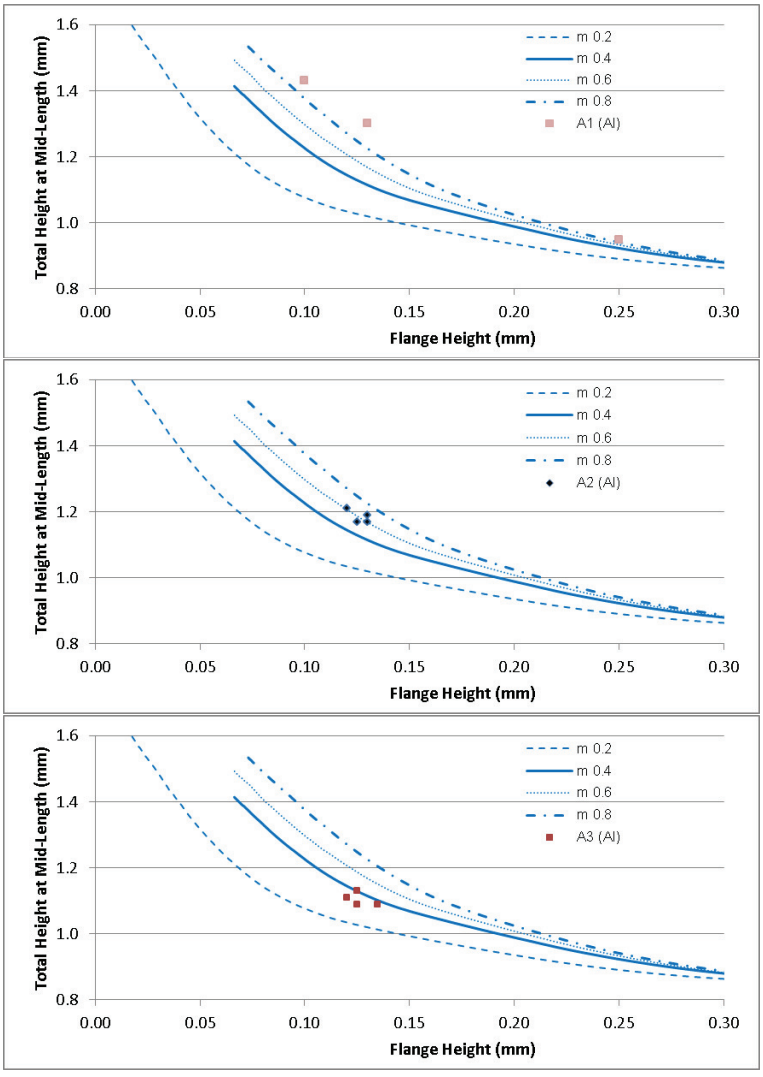


Figure 48: Aluminium experiment with aerosol spray lubricants

However, the resulting friction reduction was not the same when the workpiece material is replaced by copper, in which the lubrication performance of all lubricants was relatively similar ($m$ = 0.514 – 0.517) as shown in Figure 49. Moreover, with copper material, the addition of aerosol spray to the setup did not result in significant friction reduction but a small friction increment in comparison to the unlubricated experiment which suggested a friction factor of 0.473.

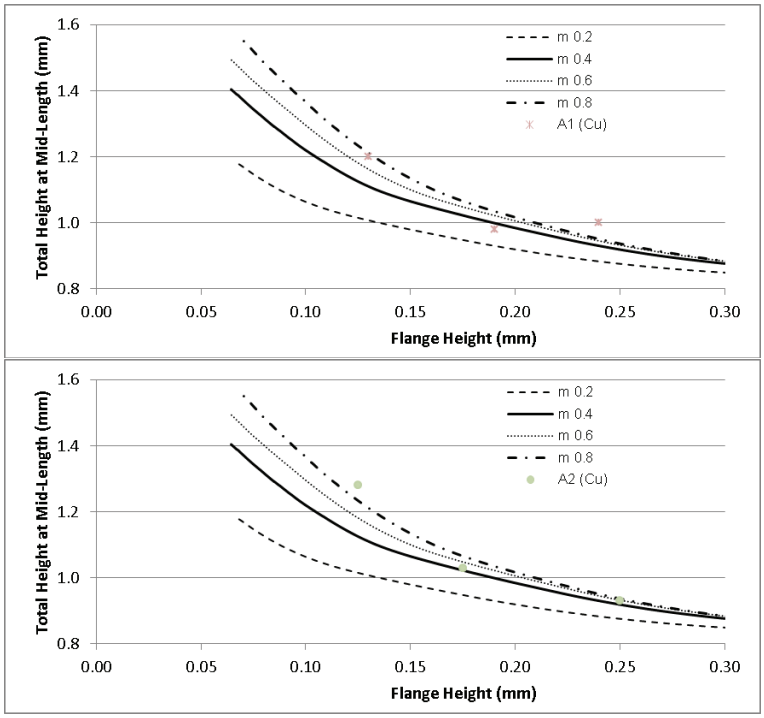


Figure 49: Copper experiment with aerosol spray lubricants

Therefore, in general it was concluded that for copper specimen, aerosol spray lubricants have no significant sign of effectiveness, i.e. the addition of lubricant for the test does not lower the friction factor *in microforming*. Such reduced lubricant effectiveness has been documented in previous studies and explained by the lubricant pocket model, the results from the current study further indicated that the friction reducing performance of lubricants can even be negligible. This supports that the upper limit of friction in microforming, as proposed by [126] is the dry/unlubricated

friction. Aerosol spray lubricants are capable of reducing friction in the case of aluminium material to some extent in microforming. However, the lowest friction achievable with the current experiment is limited to $m$ = 0.4 while in lubricated conventional metal forming process the $m$ value can be reduced to below 0.2.

### *4.6.2 Liquid lubricants*

When liquid lubricants were used in the experiment with aluminium, the results, except with L2, showed that the behaviour during the tests did not follow conventional $m$-based calibration curves (see Figure 50). Similar behaviour was observed in the experiment with copper although the trend is not as significant as presented in Figure 51. More importantly, the experiment with copper did not produce significant friction reduction with all types of lubricants.[1]

Throughout the range of flange height analysed, all the liquid lubricants showed strong linear relationship between flange height and calculated friction factor for aluminium material (see Figure 52). In general, as the flange height decreases (and deformation progresses), the friction factor calculated is increasing linearly. In contrast, the friction reduction for copper material using liquid lubricants is marginal and there is no significant correlation between the flange height and calculated friction factor (Figure 53).

[1] The lubricant L1 needs to be diluted in water prior to application. In this experiment, two grades of lubricant were formulated from L1 stock, a 10% solution and a 70% solution.

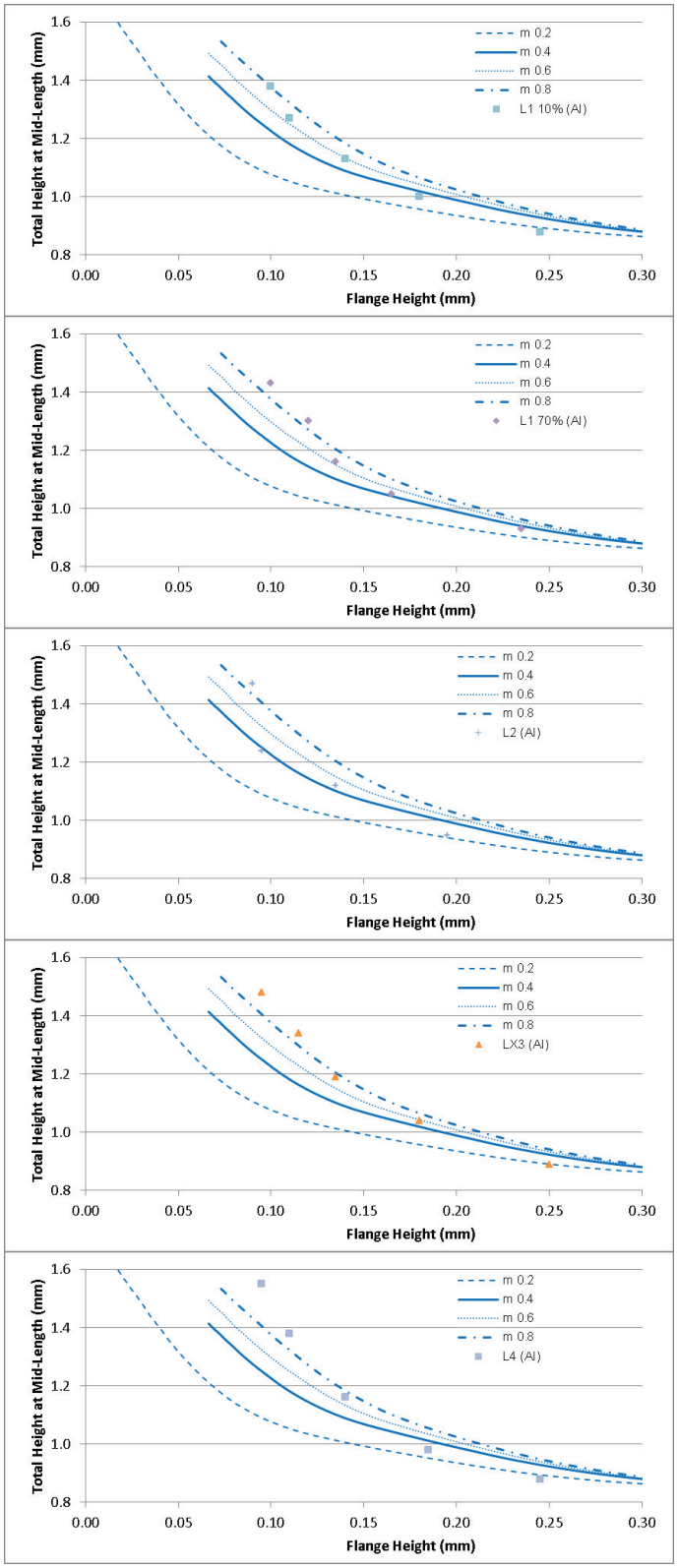


Figure 50: Aluminium experiment with liquid lubricants

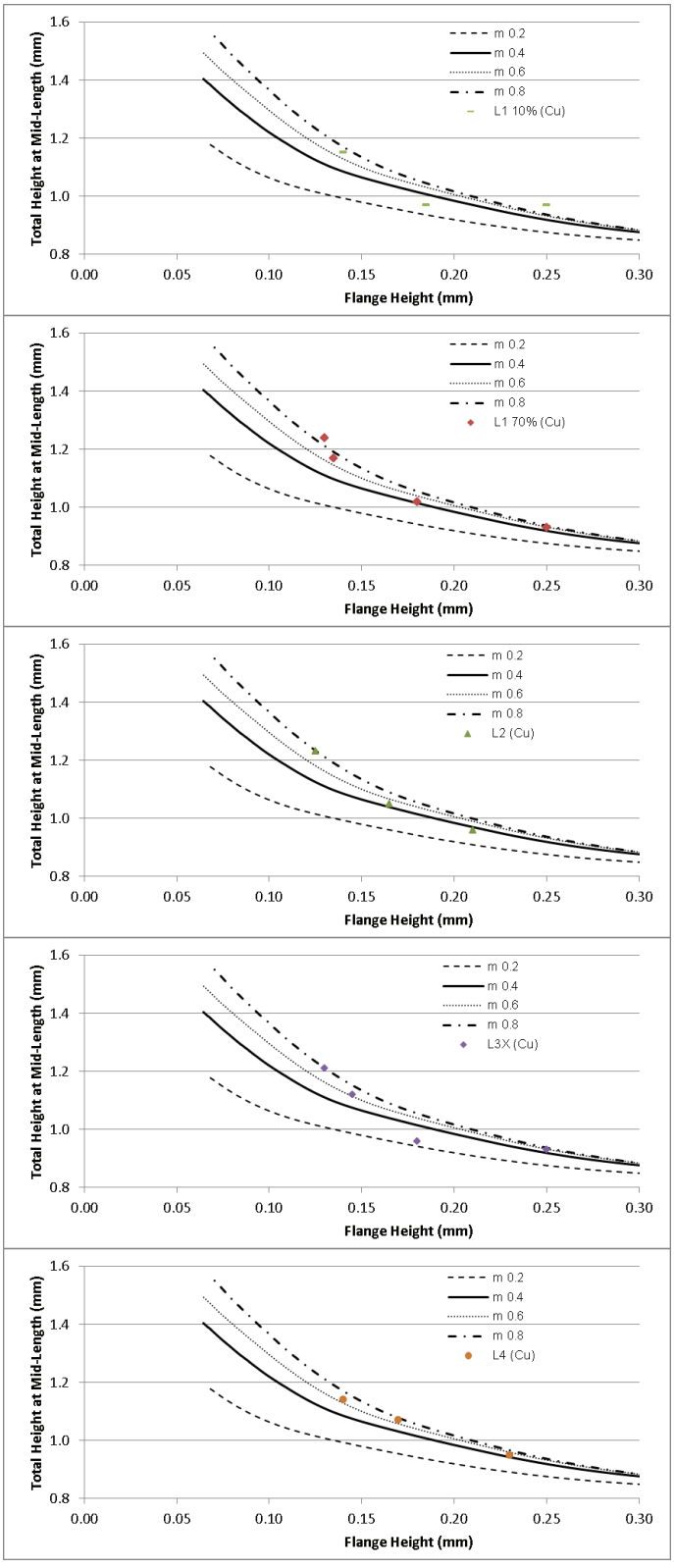


Figure 51: Copper experiment with liquid lubricants

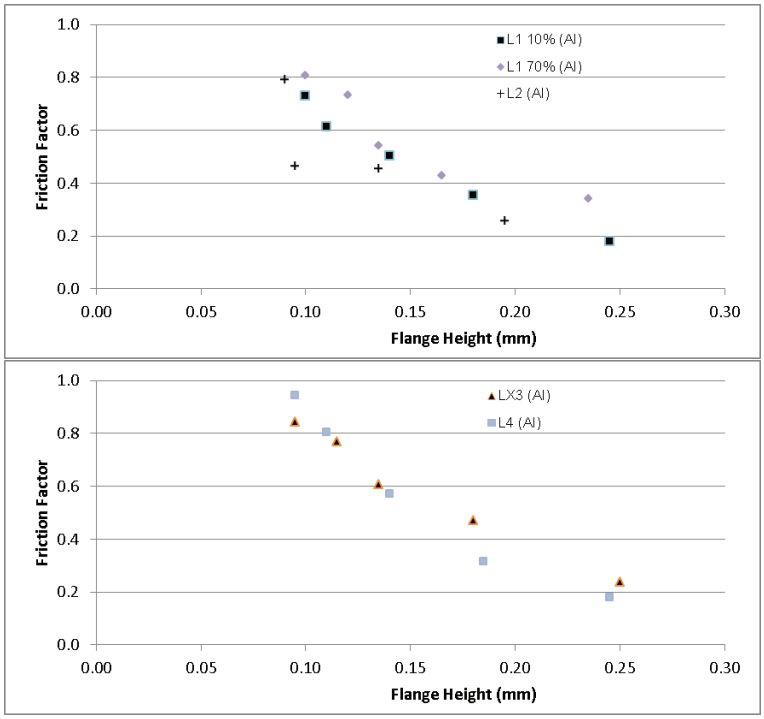


Figure 52: Increasing friction with deformation (Al with liquid lubricants)

This behaviour can be explained by considering the influence of contact pressure on the lubricant pocket model and therefore the lubricant effectiveness. The lubricant pocket model dictates that the lubricant reservoirs can be either effective reservoir (closed pocket) or ineffective reservoir (open pocket) depending on the distance of it from the nearest open surface. The mechanism of evolution from effective to ineffective reservoir is attributed to lubricant leak as contact pressure builds up. Similarly, the amount of lubricant leak (and therefore lubricant effectiveness and friction) can therefore be proposed as a function of contact pressure (Figure 54). The pressure-dependent friction factor proposed here was inspired by the equation of phase change [127]. In essence, the surface roughness forms effective lubricant reservoir at low contact pressure and this effectiveness decreases with increasing contact pressure.

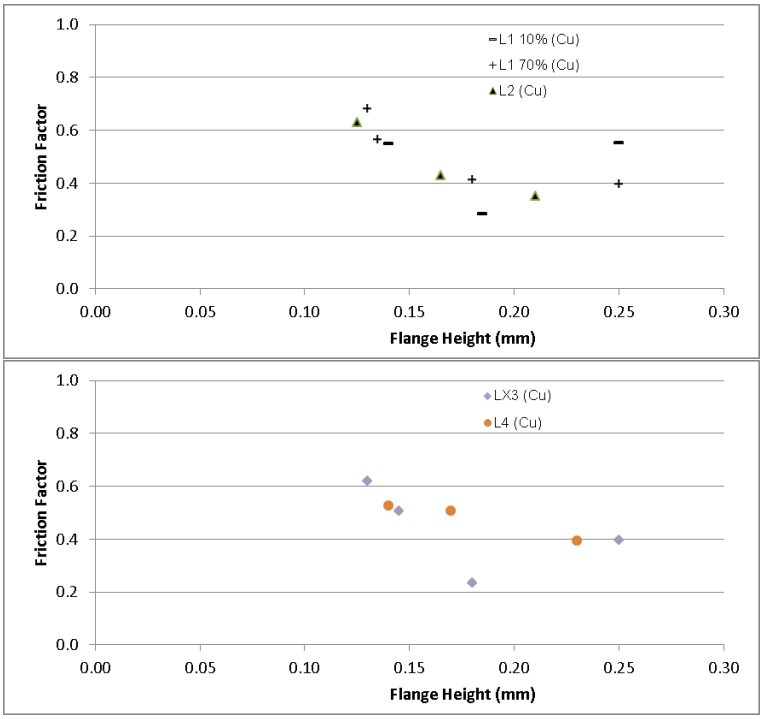


Figure 53: Constant friction with deformation (Cu with liquid lubricants)

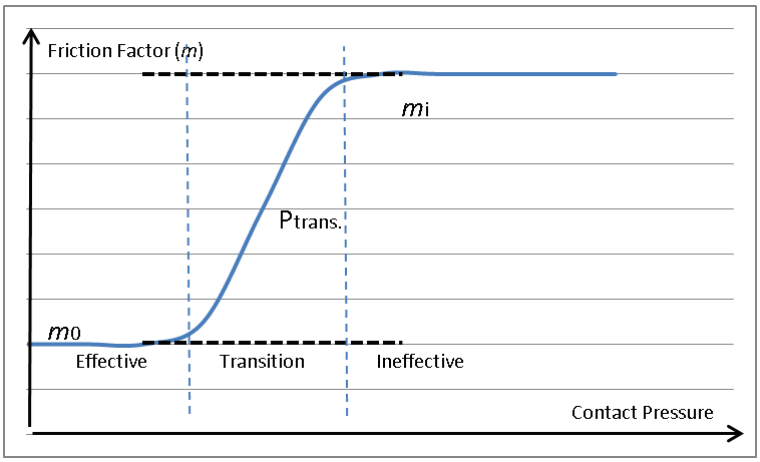


Figure 54: Frictional properties for microforming

The friction model is constructed using several parameters: $m_0$ the friction factor at effective lubrication region, $m_1$ the friction factor for ineffective lubrication and $P_{trans}$ the transitional contact pressure. However, through sensitivity analysis using T-Shape geometry, $P_{trans}$ was determined as the most critical parameter contributing to the test behaviour. Therefore, the model was further simplified to only use the parameter

$P_{trans}$. In the current study, simulation was further conducted to support the pressure-dependent friction factor model by relating to experimental results. In this investigation, the value of $m_0$ was set to 0.2 and $m_1$ to 1.0 (sticking friction). This pressure-dependent frictional behaviour was therefore proposed as a method for more accurate representation of friction in microforming in simulation.

The determination of parameter $P_{trans}$ for the various lubricants was presented only for aluminium experiment as the deviation from the constant-$m$ calibration curves is more significant than for copper. Further simulation was conducted using Deform 3D to provide new friction calibration curves based on the pressure-dependent frictional properties. In Figure 50, better lubricants would produce data points at lower total height for the same flange height associated with lower friction. Similarly in Figure 55, better lubricants would produce the same behaviour associated with higher $P_{trans}$, i.e. wider lubricant effectiveness window.

In Figure 55, the simulation results using pressure-dependent frictional properties are presented together with experimental results of aluminium with liquid lubricants. According to Figure 55, L1 70%, LX3 and L4 have similar $P_{trans}$ of 150 – 200 MPa when tested with aluminium. The remaining two liquid lubricants showed marginally better friction reduction with higher $P_{trans}$.

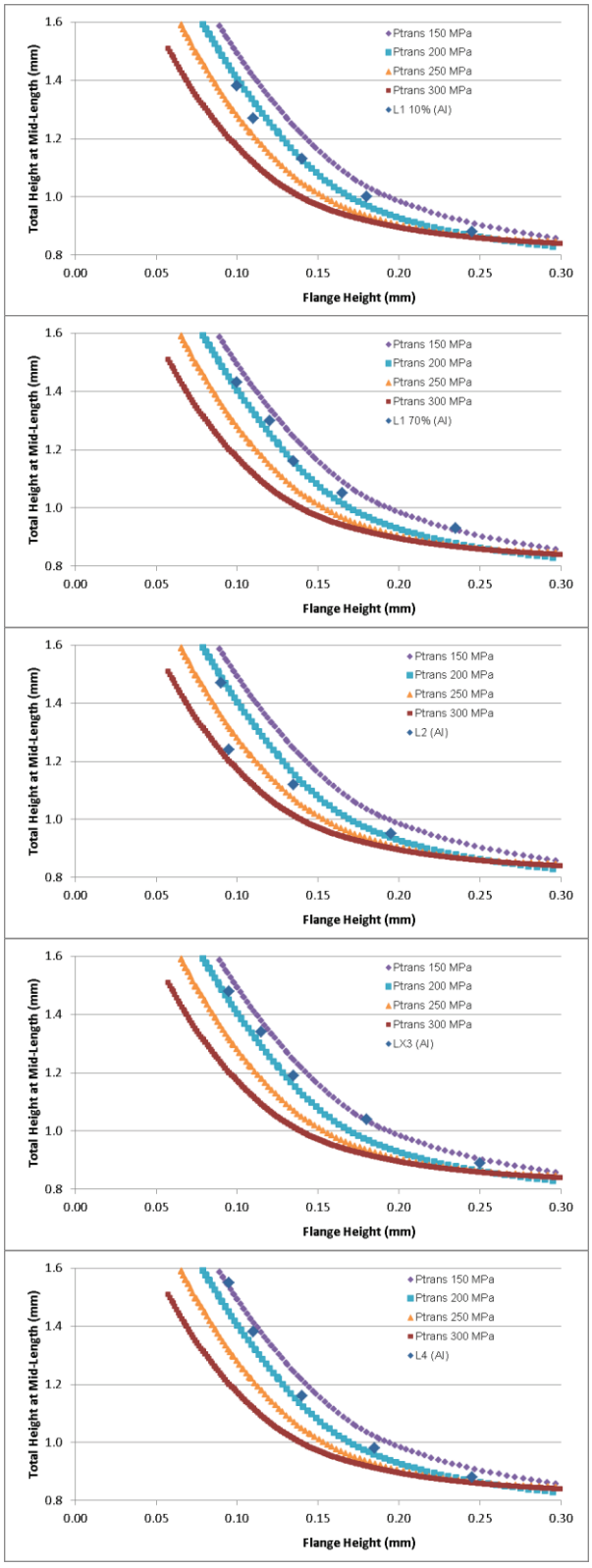


Figure 55: Liquid lubricants experiment with pressure-dependent FCC

Critically, the liquid lubricants which do not follow constant-*m* friction calibration curves showed strong agreement to the proposed friction model which supports that lubrication in microforming can be described using pressure-dependent friction factor. In the case of L2, the lubricant is capable of producing constant friction factor throughout the range of contact pressure tested and therefore the experiment using L2 showed agreement with constant-*m* calibration curves.

### *4.6.3 Dried film lubricants*

Deviation from the constant-*m* calibration curves was also observed when dried film lubricant was used as illustrated in Figure 56. As aerosol spray and liquid lubricants have no significant friction reduction on copper experiment, the dried film lubricants were tested only for aluminium. Figure 57 shows the experimental results of aluminium with dried film lubricants superimposed on the pressure-dependent friction calibration curves. Moreover, in contrast to liquid lubricants, the dried film lubricants also do not follow the pressure dependent friction factor model as closely as liquid lubricants do.

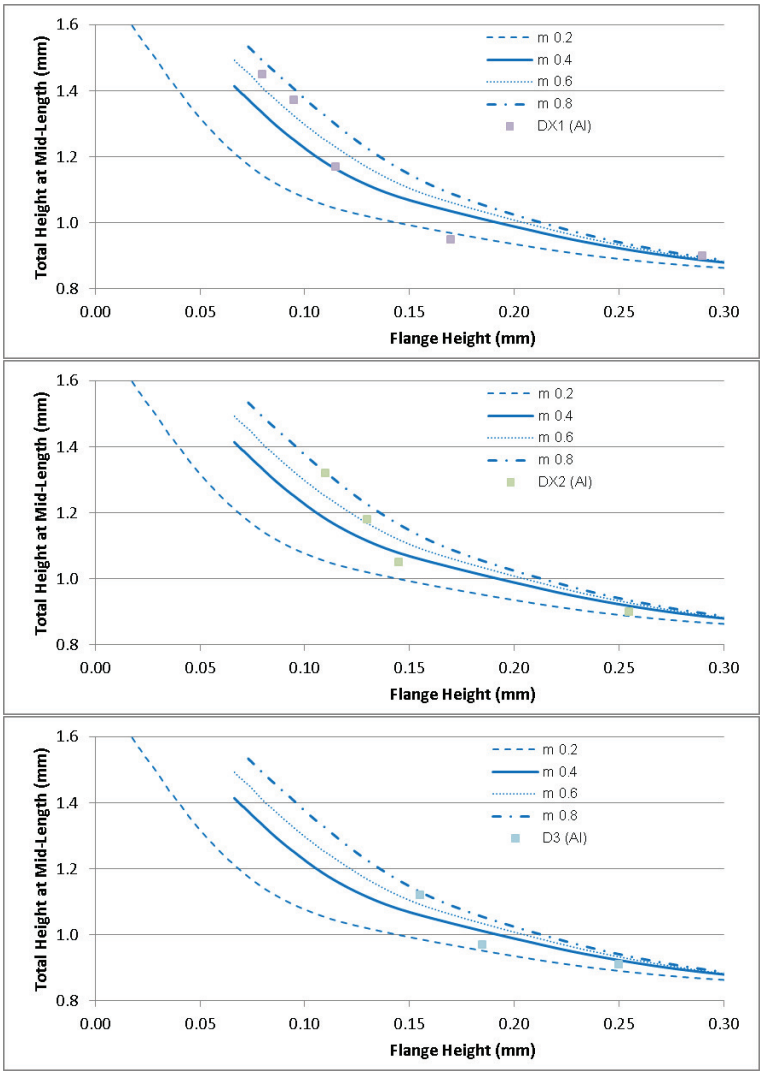


Figure 56: Aluminium experiment with dried film lubricants

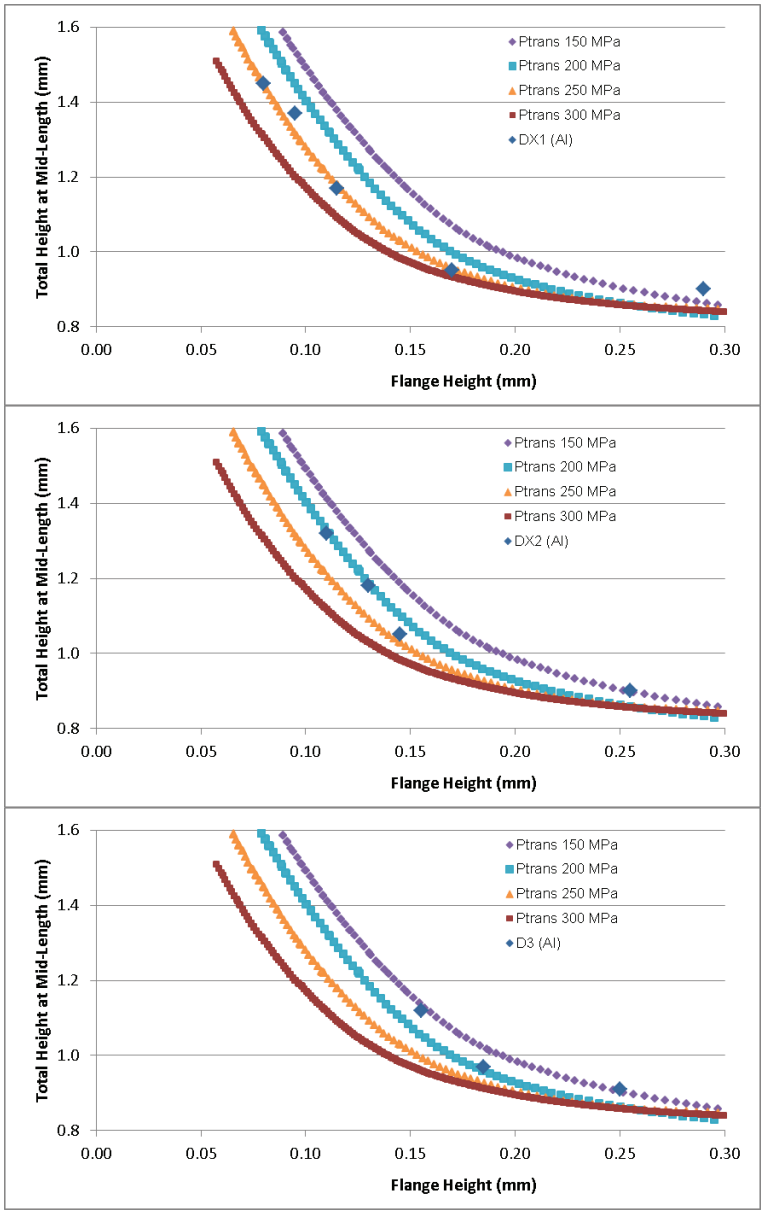


Figure 57: Dried film lubricants experiment with pressure-dependent FCC

The lubrication performance of the three groups of lubricants was evaluated using two workpiece materials, copper and aluminium. Generally, all the lubricants did not produce the desirable friction reduction associated with effective lubrication when copper material is used. Also, the lubricants do not produce significant differences in friction factor between them which supports that lubrication has no apparent efficacy in the current experiment.

However, when aluminium is used, the three groups of lubricant showed relatively good differentiation between each other. Spray lubricants generally showed accordance to constant-*m* calibration curves in the T-Shape test. The amount of friction reduction was also significant for A2 and A3. In the case of liquid lubricants, strong accordance to pressure dependent friction factor was observed and can be related to the lubricant pocket model.

Ultimately for dried film lubricants, the frictional behaviour follows partly both sets of calibration curves. It is suggested that dried film lubricants carry both the traits of liquid lubricants because of their solvents and the traits of spray lubricants because of the nature of solid lubrication, i.e. friction is constant at low deformation (low contact pressure) and pressure-dependent at high deformation (high contact pressure). Galling was still observed for lubricated aluminium experiment although the amount of material transfer was relatively reduced.

Among spray lubricants, the lubricant A3 was considered best lubricant as it gives rise to the lowest friction factor. For liquid lubrication, the forging lubricant L2 was determined to be best as its performance is not pressure-dependent, i.e. lubricant leak associated with pressure build up is not significant. In comparison to machining or sheet metal forming processes, forging involves much higher contact pressure between tool and workpiece. The resilient performance of lubricant L2 from low to high pressure is consistent with the design as forging lubricant. Finally, the prototype lubricants DX1 and DX2 are incrementally better performers than lubricant D3.

## 4.7 Closing Remarks

The microforming T-Shape test design is proposed for friction investigation tool for microforming research and industry. With that in mind, the characterisation approach

to the T-Shape test was redesigned and its versatility for industrial scale was improved by simplifying the handling during the test as well as allowing users to inspect the pre- and post-test surface conditions, such as the surface roughness and galling observation.

Tolerance allowance was also established in order to minimize the fabrication cost while keeping the performance of the test. The current geometry has also been found to produce little influence from changing material properties and multi-material experiment has been conducted to validate the performance of the friction test.

In addition, a mathematical function was proposed to represent the calibration curves and obtain accurately the friction coefficients. It has been shown that large difference in friction factor ($m$) in the aluminium experiments in comparison to the other two materials can be attributed to the chemical aspect of the aluminium piece, i.e. its behaviour to spontaneously to form oxides. It was also shown that the lubricant effectiveness in the current experiments is very limited to aluminium experiments and the effectiveness is not evident for copper. In the lubricated experiment with aluminium, the three groups of lubricants are well distinguished by their frictional behaviour, be it a solid lubrication, a liquid lubrication, or a hybrid of both.

These differing behaviours are seen as the effect of the constituents of the lubricants. In solid lubricant, the lubricant effectiveness is maintained so long as the size of the solid particles is still significantly smaller than the surface features (roughness). This explains the constant friction factor throughout the test for the solid lubricants. In the liquid lubricants, the lubrication is governed by the surface tension properties of the lubricants, i.e. cohesion and adhesion. As such, every liquid lubricant has a specific limit of lubricant effectiveness which corresponds to the pressure at which the

lubricant film can no longer sustain at the contact. Whereas dried film lubricants seem to carry traits of both solid and liquid lubrication.

A phenomenological friction model was also proposed in the study in order to provide more accurate representation of friction in liquid lubrication settings.

# CHAPTER 5 SURFACE TEXTURES FOR FRICTION CONTROL

## 5.1 Background

Past investigations have shown the friction increases with miniaturization in microforming [3]. Results from the current study using microforming T-Shape test supports this finding and the limit of lubricant effectiveness was proposed.

Because of this, there is a need to look into non-traditional friction control. Surface textures have been extensively studied and their effectiveness in controlling friction has been documented for lubricated condition [68], unlubricated condition [69], and even for sheet metal forming application [70]. However, previous studies on surface textures focus mostly on experiments with only limited explanation for the friction-reducing behaviour. Previous works have mostly focus on two geometries –parallel grooves and pores, and the results showed that the friction reduction can be attributed to some parameters (texture area density [77], texture size [83] and texture geometry [128]. The investigation for use in bulk metal forming has started recently and its focus was mainly in aiding lubrication and extending tool life [72, 73]. In the current study and studies reviewed herein, the surface textures are defined as geometrically deterministic surface features with dimensions between 40 and 200 μm. In the context of microforming, this size is considered suitable so that the contact during forming covers at least a few textures concurrently.

Wear particles entrapment has been proposed as the friction-reduction mechanism for unlubricated contact [74]. However, results suggest that the friction-reduction has initiated at very small sliding distance at which wear particles are unlikely to have been generated [69, 74]. Wear particles are removed from surface as wear sheets

which are generated only through creation of sub-surface cracks. Through repeated sliding, these micro-cracks coalesce to form larger cracks. The wear particles (in the form of sheets) get delaminated from the surface only after the crack reaches a critical size. Such mechanism is known as the delamination theory of wear [129].

In lubricated contact, the friction-reduction has been attributed to lubricant entrapment to enable the lubricant to remain on the surface [77] and to enhanced hydrodynamic lubrication [79] for boundary lubrication and full film lubrication [62], respectively. However, experiments have suggested that friction-reduction can also be reached in water-immersed sliding setup [68]. In the immersion setup, water was supplied abundantly such that the two sliding surfaces are submerged in water ensuring complete lubrication. These findings suggest that the wear particles and lubricant entrapments are not the only friction-reducing mechanisms attributed to surface textures. In other words, further understanding of mechanism is required such that the friction reduction explanation applies for all cases of sliding contact.

The scope in this part of the study is to propose a FE approach to simulate contact between smooth and textured surface. In order to validate the approach, a tribometer experiment was conducted alongside.

## 5.2 Pin on Plate Test

A well designed simulation setup will be able to provide realistic clarification for the role of surface textures. The current investigation considers surface textures with texture size of approximately 100 μm. This size is chosen as it is within the 40 – 200 μm texture size context of the study.

Prior to the development of the simulation, it was necessary to develop and perform the appropriate validation experiment for two reasons: a) to examine the feasibility of having surface texture as friction control in microforming, b) to obtain appropriate friction definition for the simulation input. The experiment involves producing surface to surface contact throughout the range of contact pressures relevant to metal forming, up to above the yield stress of the material.

### *5.2.1 Surface texturing*

Experimental validation on the role of surface textures in microforming would involve two parts: a) determining good and repeatable method to fabricate surface textures of the desired 100 μm texture, and b) conducting a constant-pressure friction test which allows experimenting throughout the range of contact pressures relevant to metal forming.

Fabrication of surface textures using 533 nm wavelength Q-switch Nd:YAG nano-second laser was attempted to have a viability study of using long pulse laser for fabricating surface textures on hardened SLD Magic tool steel surface. The target aspect ratio for the surface texture for pore texture was set as depth to diameter ratio of 0.1 as it was revealed by Amanov et al. that aspect ratio closer to 0.1 produces the lowest friction [67].

Using long pulse laser for surface texturing, the laser fluence and number of pulses irradiated from the laser source determines the geometry of the resulting pore. However, the disadvantage faced in using laser for surface texturing is that the results are not repeatable as presented in Figure 58. Using the same parameter, two very different pore geometries can be obtained and therefore the use of the laser is not

desirable. Moreover, long pulse laser creates very significant bulge on the rim of the pore in Figure 58 (Right) as the heat energy from the long pulses resulted in material melting and solidification rather than ablation. The images of the textured surface were taken using the Alicona InfiniteFocus form measurement instrument.

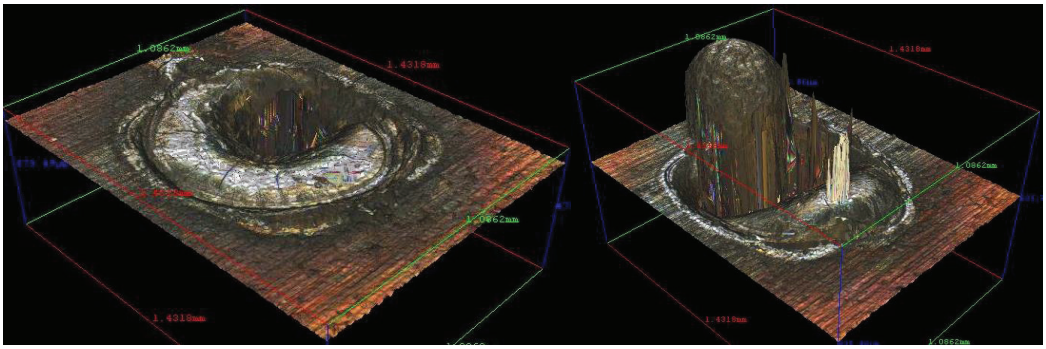

Figure 58: Non-repeatability of long pulse laser for surface texturing

Micro-drilling process was also attempted in producing pore texture. However, the use of micro-drilling tool for surface texturing created unwanted bulge surrounding the pore and there is no control of the side surface of the pore texture as presented in Figure 59.

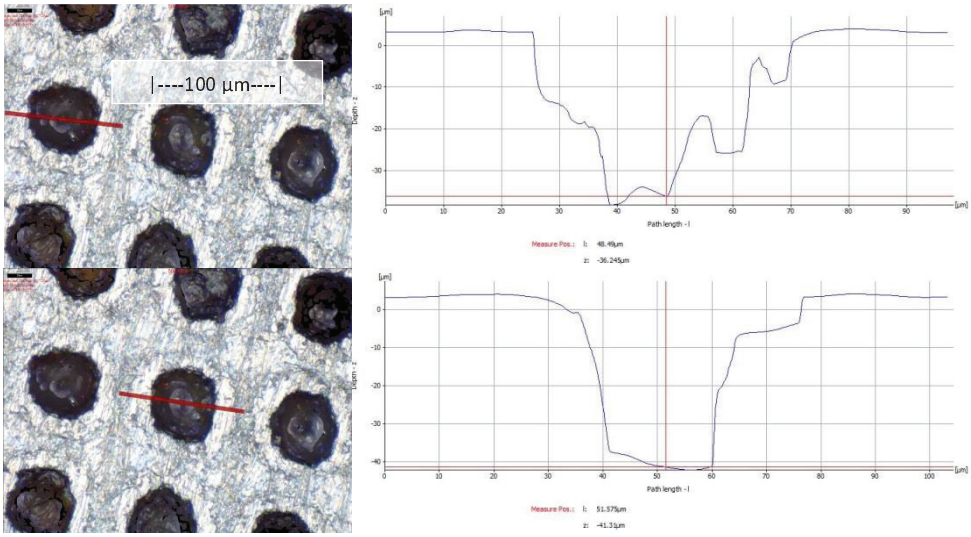


Figure 59: Inconsistent wall from micro-drilling

An accurate way to fabricate surface texture is using embossing technique. The principle of embossing technique is to create a male textured pad which produces the corresponding female surface textures. However, in order to create textures on tool steel (HRC > 60), a harder embossing tool is needed, e.g. diamond tool [87].

However, the fabrication of diamond embossing tool was not carried out as the level of complexity of perfecting a method to produce diamond embossing tool is considered too vast with respect to the focus of this study. Instead, tool steel AISI D2 was used as the material for the embossing tool. The male textured pad was created using wire electro-discharge machining. An example of such pad is presented in Figure 60. This embossing tool was further used to create the textures on softer material.

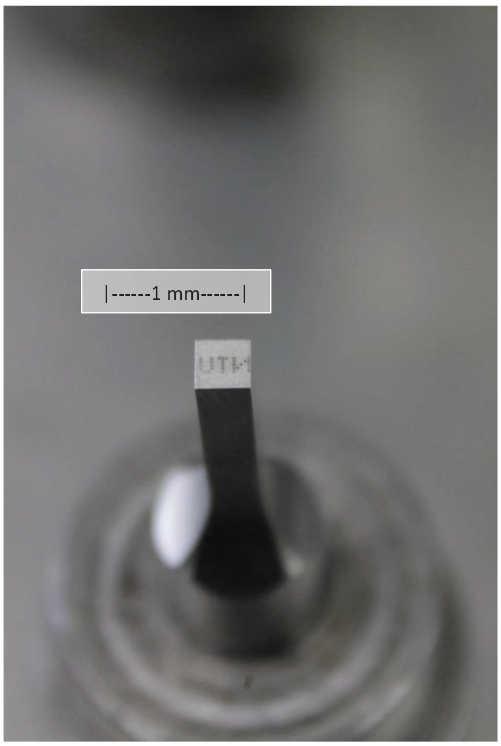


Figure 60: Male textured pad bearing the letters "NTU"

During this study, four different male pads were manufactured with different textures. Two of them are created with letters “NTU” and “SIMTech” which can be used also as an example of product identification (Figure 61). The SIMTech pad consists of square-shaped pore with 100 µm size and 200 µm centre-to-centre spacing (from now on referred to as “square pore”) while the NTU pad consists of round-shaped pore with 100 µm diameter and 200 µm centre-to-centre spacing (referred to as “round pore”). In Figure 61, the textures were created on ETP Copper material.

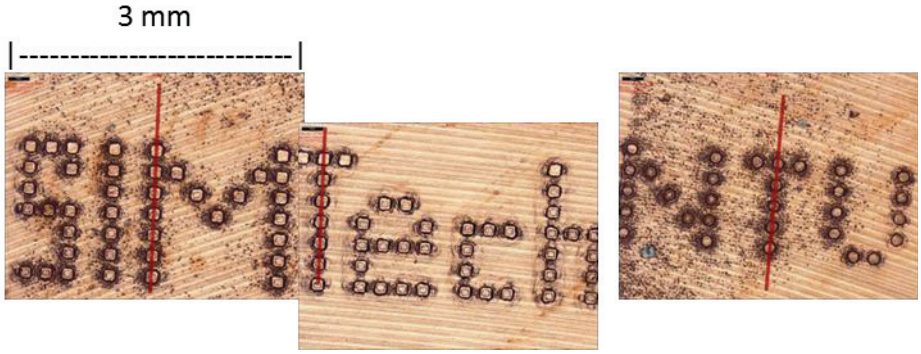


Figure 61: Resulting textures with “SIMTech” and “NTU” pads on copper

The other two pads were fabricated with full array of round- and square pores (Figure 62 and Figure 63), respectively. All the textures were produced through load controlled embossing to create aspect ratio between 0.10 and 0.15. The textures produced by these pads are presented in Figure 64.

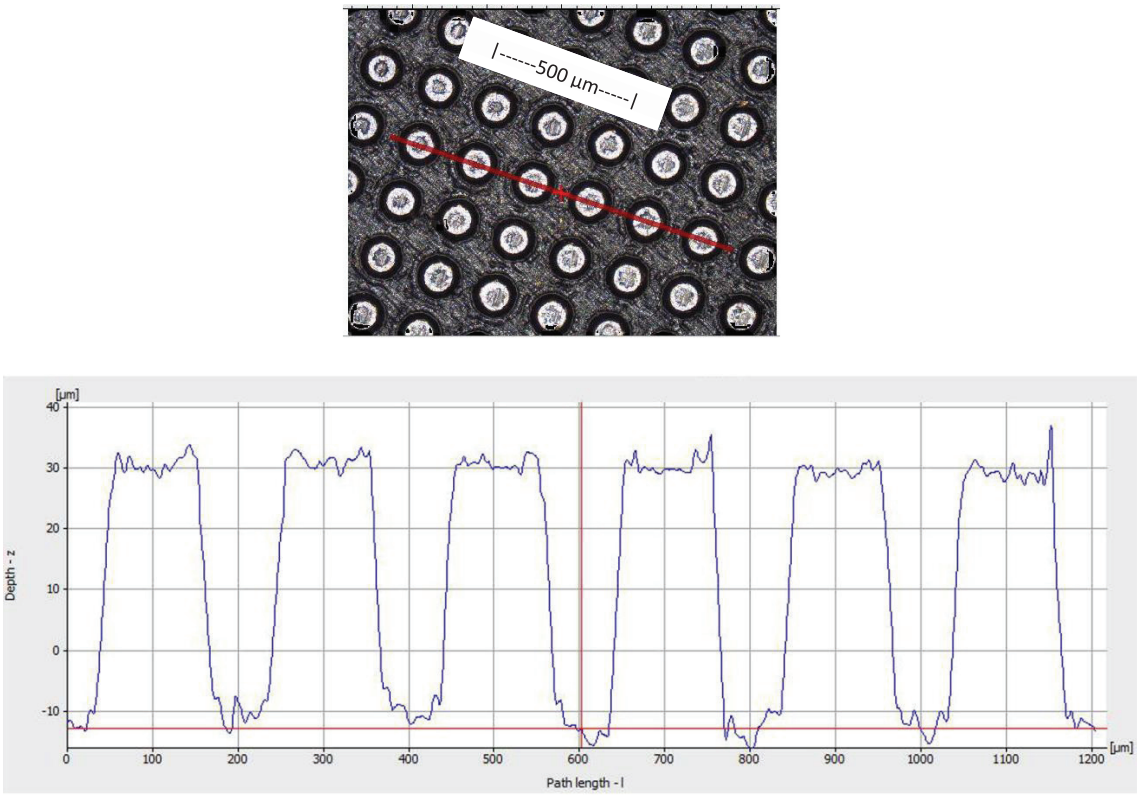


Figure 62: Geometry of male textured pad (round pore)

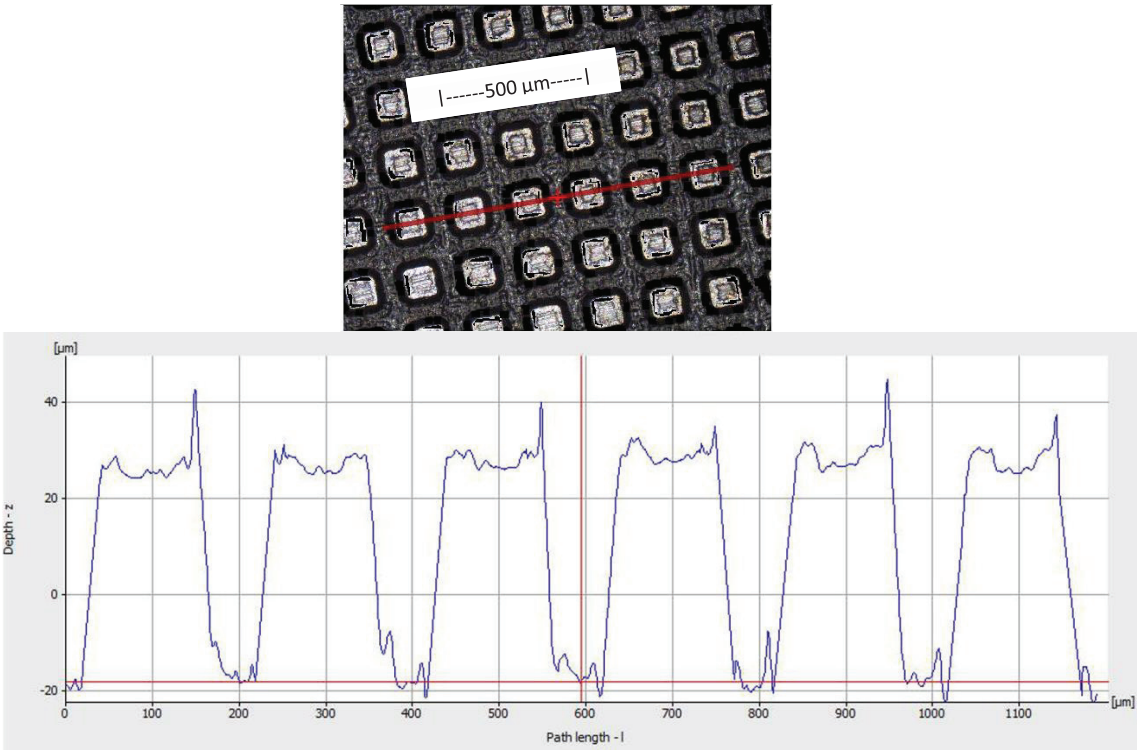


Figure 63: Geometry of male textured pad (square pore)

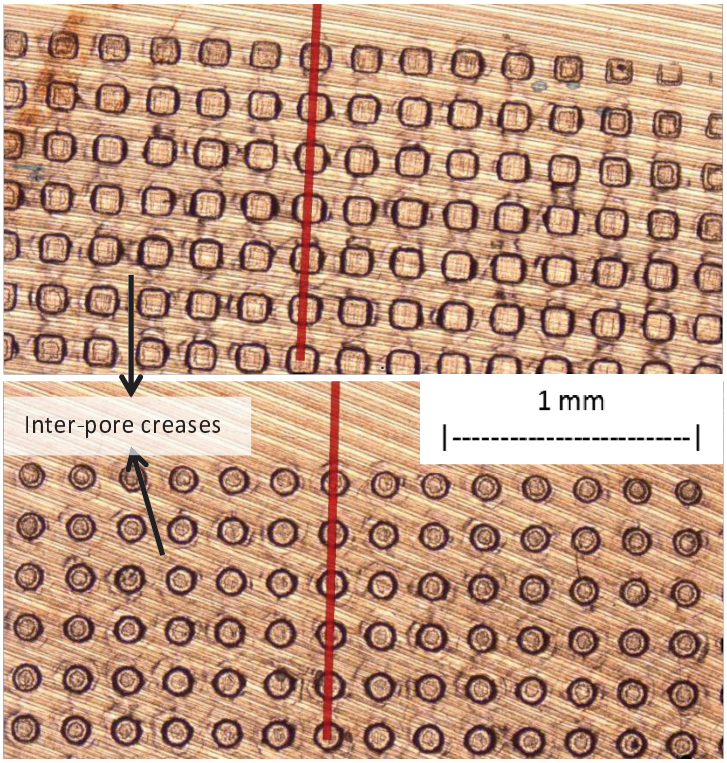


Figure 64: Resulting textures with square- and round pore pad on copper

However, inter-pore creases were observed during the post texturing examination for copper material as shown in Figure 64. These creases significantly roughen the surface of the textured material. In order to determine whether the creasing is a process or material related behaviour, another set of textures were created on AISI 316L stainless steel. Ultimately, these creases were not observed on textured stainless steel 316L material as the machining lay observed between the pores are in accordance to the machining lay on the untextured surface (Figure 65). This finding can be further studied through the examination of the mechanism of micro metal deformation and the difference in crystal structures, Poisson's ratio and general ductility can be attributed to the significant difference in embossing deformation behaviour.

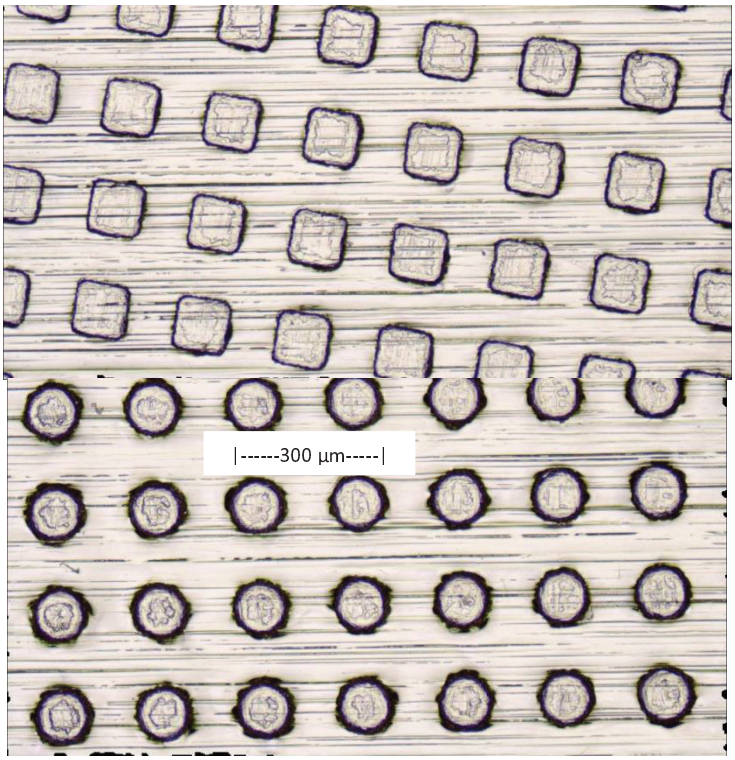


Figure 65: Resulting textures with square- and round pore pad on stainless steel

### *5.2.2 Tribometer test*

In order to focus on the effect of the contact area reduction from the surface texture, the tribometer test was conducted only for 316L stainless steel material as texturing of this material does not produce creasing between the pores. As for the texture, only one texture was used in the experiment –the round pore texture.

The same simulation approach presented in this chapter was used again to simulate the tribometer test of tool steel pin on textured 316L stainless steel plate. The comparison between the experiment and simulation was then used to examine the accuracy of the simulation approach.

In the experiment, a series of textures was produced using the pad to create the consumable plate (Figure 66) for a pin-on-plate tribometer experiment. In a single textured experiment, the sliding of the pin covers only the textures produced by one embossing (i.e. 3 mm) such that the sliding does not occur on the gaps.

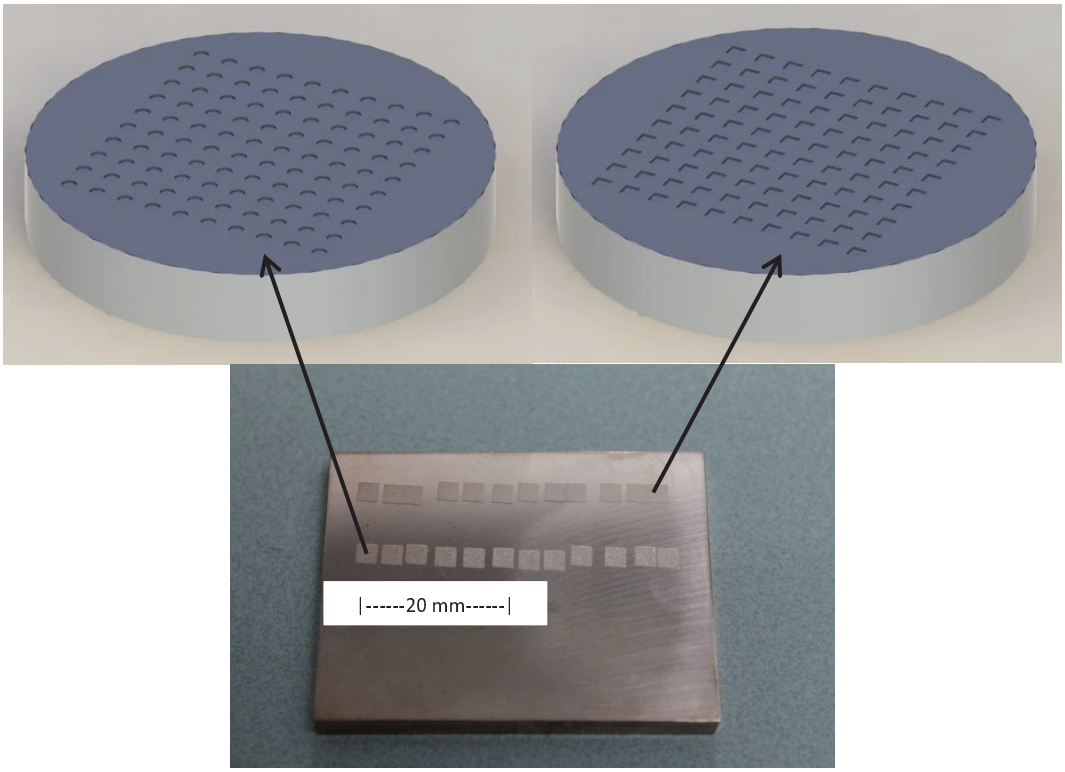


Figure 66: Textured plate for tribometer test

AISI D2 tool steel was used to make the pin for the experiment as illustrated in Figure 67. The pin has a circular tip of 1 mm diameter. However, fillet around the circular tip was necessary to avoid ploughing of the plate material by the sharp edge and therefore the effective contact diameter is reduced to 0.7 mm. This has been verified through post-experiment scratch examination on the stainless steel plate by Alicona InfiniteFocus. The circular tip was finished by fine grinding to create surface finish of approximately Ra 0.9 – 1.0 μm.

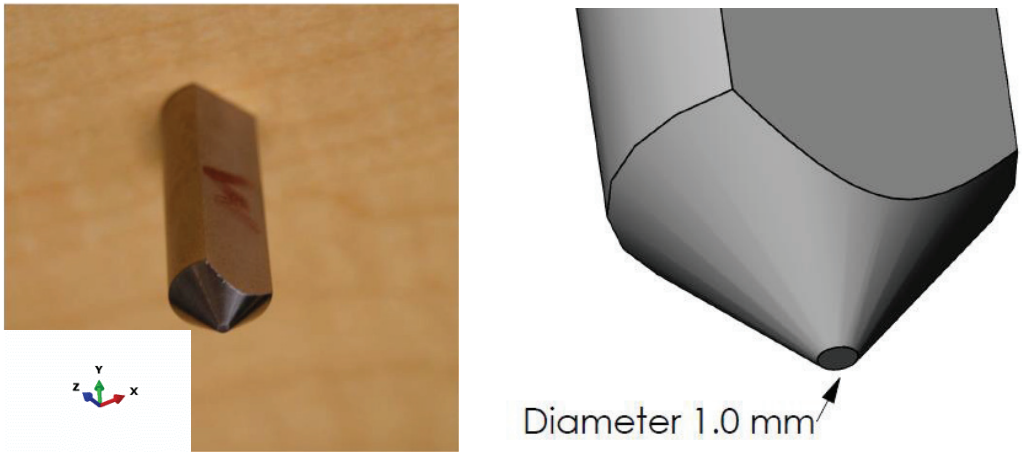


Figure 67: Experimental pin for pin on plate test

Untextured pin on plate experiment was conducted to provide the frictional properties to be used in the simulation. CETR UMT3 tribometer was used for the pin on plate experiment. The experimental result of the untextured pin on flat experiment is presented in Figure 68.

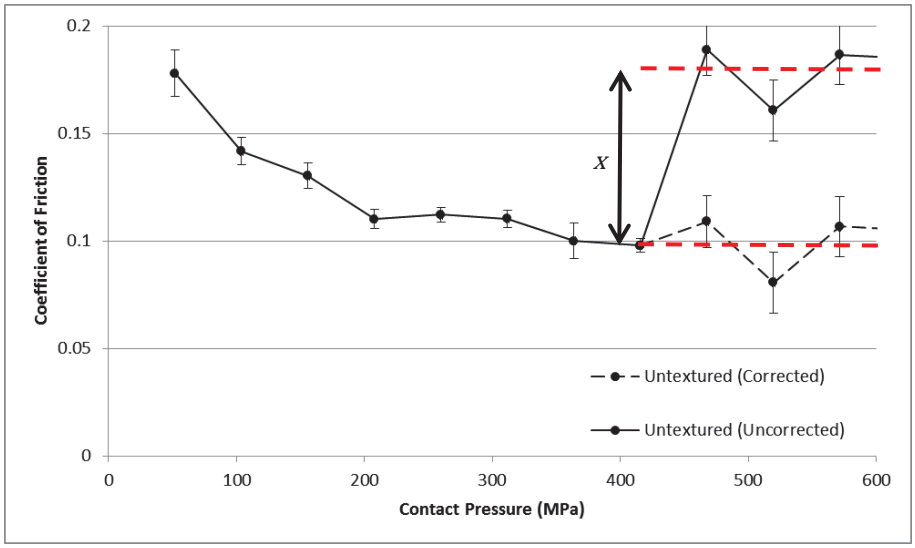


Figure 68: Untextured pin on plate experiment results

Tribometer test is generally used for repetitive sliding at low contact pressure (up to tens of MPa) and its use for high contact pressure such as in the current study (up to

600 MPa) presents unavoidable experimental artefacts which require correction of experimental data. In Figure 68, there is significant increase of coefficient of friction between tests at 400 and 450 MPa. This was attributed to the rotational flexure of the tribometer suspension whose structure is illustrated in Figure 69.

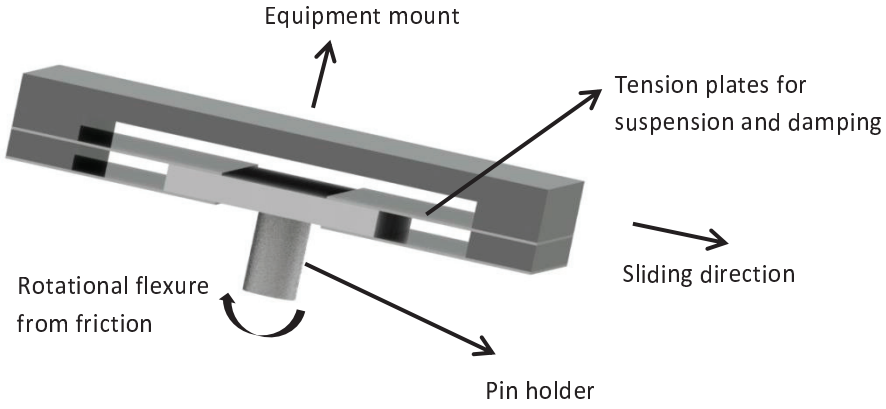


Figure 69: tribometer rotational flexure

In the tribometer test, the pin is connected to the load cell through a suspension to create a smooth contact transition and safeguard the load cell from sudden compression at the start of contact. Although this suspension is optimized to be used for up to 100 kg loading, the suspension was not able to sustain its lateral rigidity and therefore, at pressure upwards of 400 MPa, the suspension starts to flex and the contact between the pin and plate is no longer circular and the pin starts to plough into the softer plate due to the much reduced effective contact area. This ploughing effect creates the significant increase in the coefficient of friction.

The correction was further taken by subtracting the coefficient of friction above 450 MPa by the gap between the average coefficient of friction for the immediate three data points higher and lower than 425 MPa and this correction is shown in Figure 68, denoted as *x*. This corrected data was fitted in order to produce continuous frictional data for the simulation as superimposed in Figure 70 in accordance to general friction

model [56, 102] with yield stress of the stainless steel material. As the workpiece material does not undergo significant bulk deformation, the shear strength $k$ in equation 1.5 is considered a constant of $1/\sqrt{3}$ of the yield stress of the material based on von Mises yield criterion.

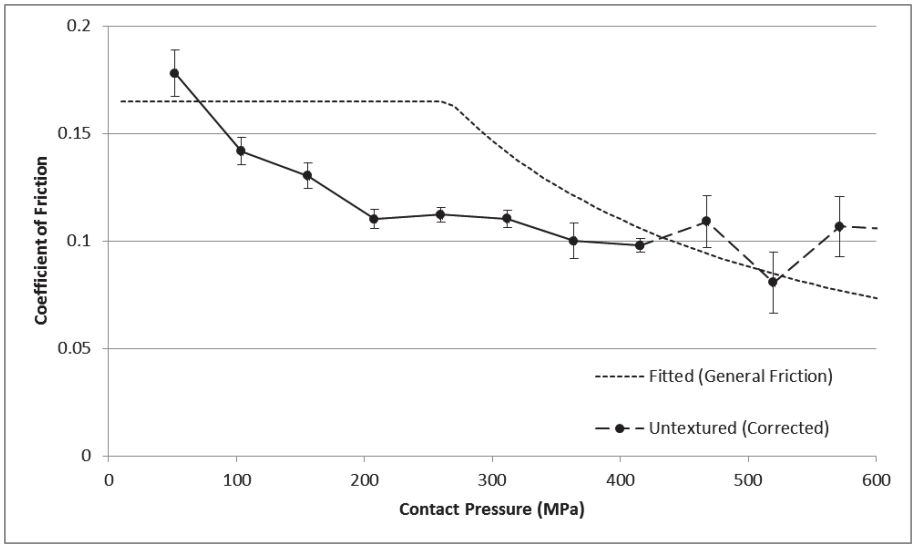


Figure 70: Untextured pin on plate experiment results (corrected)

Similar experiment on textured surface was conducted and the experimental results (uncorrected and corrected) are presented in Figure 71.

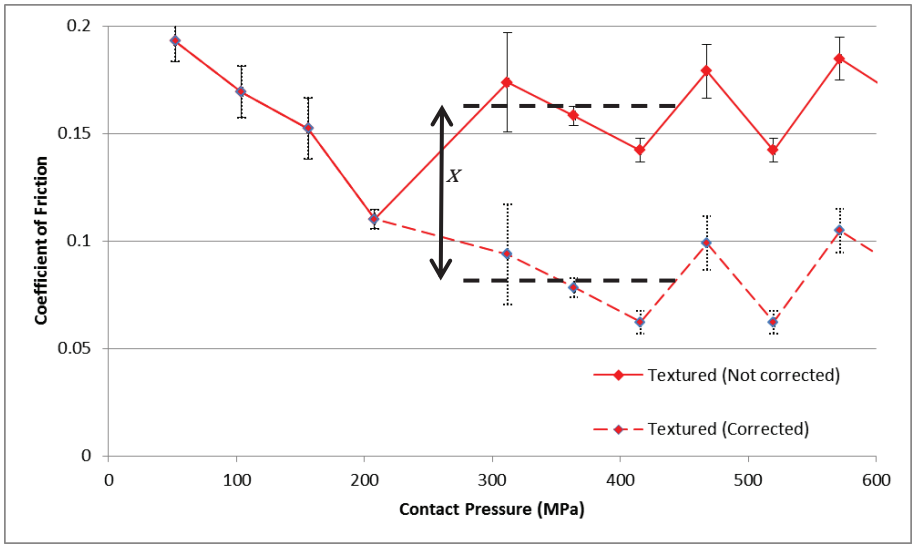


Figure 71: Textured pin on plate experimental results

The friction reduction throughout the range of pressures examined can be quantified by calculating the percentage of friction reduction ($\%\Delta\mu$, Eq. 5.1 and Figure 72). However, experimental results were not able to provide clear distinction on the limit of texture effectiveness due to variability in the results as presented in Figure 72. As such, a trend line for Figure 72 (with correlation factor of $R^2 > 0.95$) is presented for the material pair in the experiment.

$$\%\Delta\mu = \frac{(\mu_{untex.} - \mu_{tex.})}{\mu_{untex.}} 100\% \qquad 5.1$$

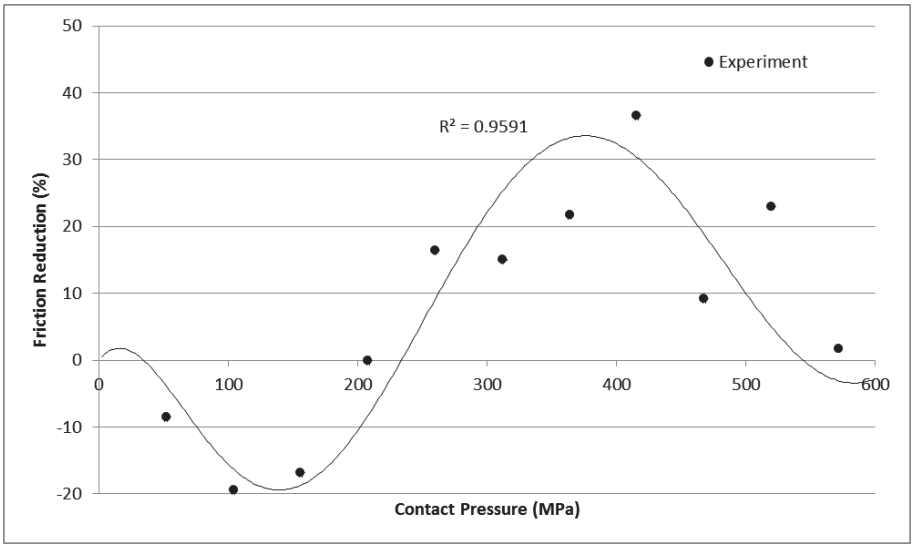


Figure 72: Friction reduction from the addition of surface texture (experiment)

Using the surface texture, a sinusoidal-like behaviour was observed and two distinct regions are highlighted. There is a region with positive effect from surface texture (positive friction reduction, 230 – 550 MPa) and another segment with negative effect from surface texture (negative friction reduction, 50 – 220 MPa). It is important to note that the positive friction reduction is observed only above 230 MPa and the results at contact pressure above 200 MPa were subjected to data correction (Figure

71). This sinusoidal-like trend will be studied further using FE simulation in section 5.3 as the experiments are not able to provide the physical explanation for the behaviour.

## 5.3 Pin on Plate Simulation

The simulation is aimed to predict the behaviour of surface textures without performing the full friction experiment with real textures. The inputs and outputs for the simulation, including the boundary conditions have been explained in Chapter 3.

The round pore texture produced by the pad has a texture density of approximately 20%, further called the P20 texture. This P20 texture is recreated using SolidWorks to be then imported into the simulation (Figure 73). The material properties of the stainless steel 316L was then used as the material definition for the P20 texture. On the counter surface, the much harder tool steel is prescribed as smooth surface and discrete rigid (Figure 74).

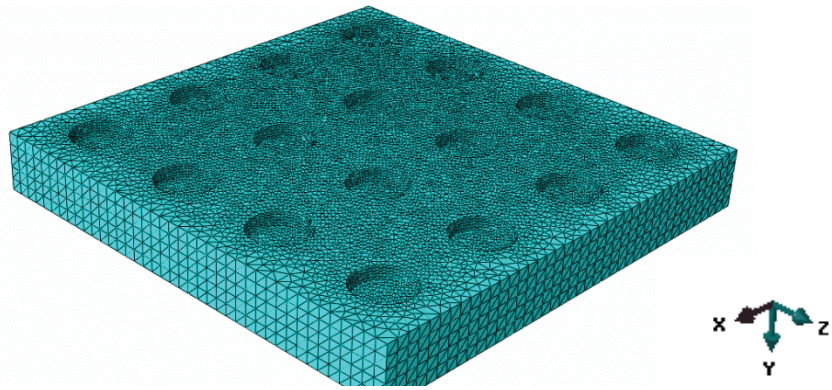


Figure 73: Round pore texture deformable mesh representing 316L

In the simulation, the P20 mesh was pinned at the bottom (see Figure 73). The contact pressure was produced by moving the rigid body into the workpiece (+Y direction).

Simultaneously, the textured tool is prescribed with a sliding movement parallel to the workpiece surface (+X direction) with the gradient of ploughing movement of 4%, i.e. 4 micron in -Y direction movement every 100 micron in +X direction movement. The reaction forces along the X and Y directions were analysed. The ratio between reaction forces along X (sliding) axis and Y (normal) axis is then recorded throughout the contact pressures to create pressure dependent friction definition resulted by simulated texture (Figure 23). The simulation was repeated with a different displacement of the tool into the workpiece to provide prediction of friction behaviour at various contact pressures.

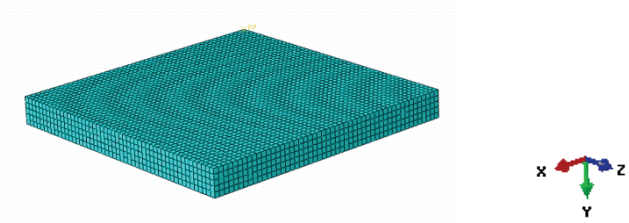


Figure 74: Discrete rigid mesh representing tool steel

The simulation does not simulate the whole pin on flat experiment. Instead, the simulation assumed periodicity of the textured and smooth surface to obtain good details during the simulation without adding much computation time. As such, in the simulation, the discrete rigid body is made sure to be in contact with the same number of textures at any time during the simulation. As a control, a similar simulation was also performed using smooth surfaces for both the stainless steel and the tool steel pin.

The simulation results for the untextured and textured tool steel pin on stainless steel plate are presented in Figure 75 and Figure 76. In general, the simulation is able to capture the trend from the experiment especially for the untextured setup. It is noted

as illustrated in the simulation graphics in Figure 76 that at high contact pressure, there is significant deformation on the softer textured surface which may result in non-performance of textured surface at high contact pressure as the textures get damaged.

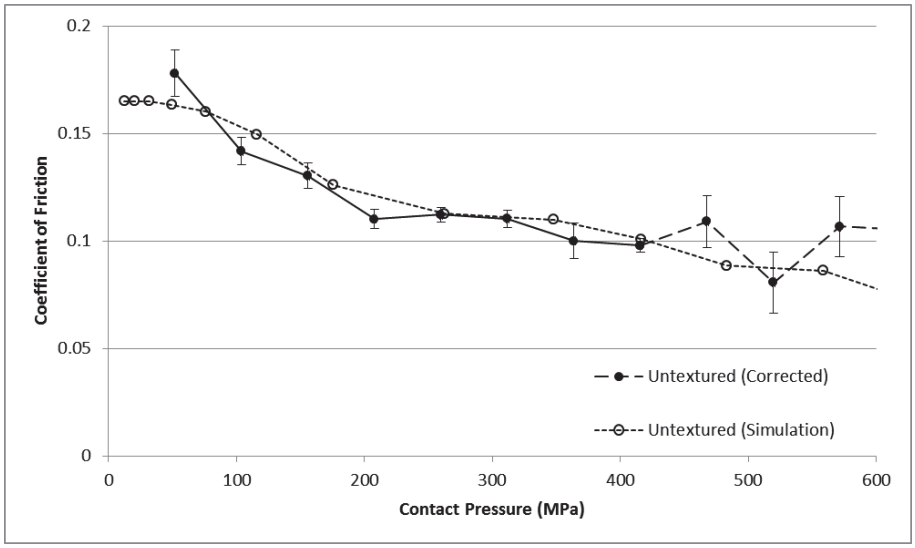


Figure 75: Pin on plate simulation result (Untextured)

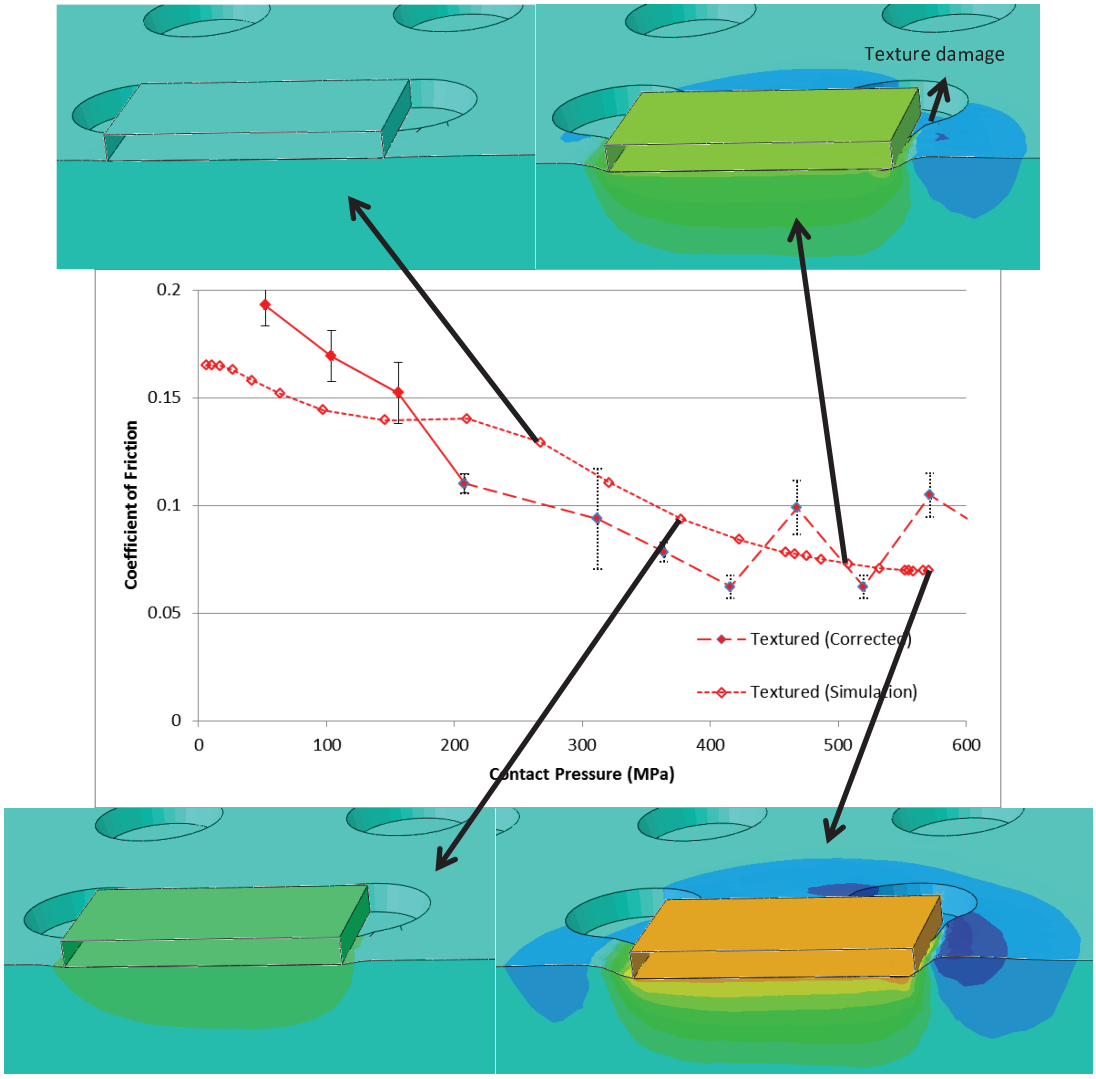


Figure 76: Pin on plate simulation result (Textured)

The percentage of friction reduction from the simulation is further presented in Figure 77. From the trend line (with correlation factor of R2 > 0.97) drawn in Figure 77, it is observed that the positive effect of surface texture is visible between 30-130 MPa and above 330 MPa. As the simulation does not include defect such as possible bulge on the rim of the individual texture, Figure 77 is therefore achievable only if the fabrication of texture is done perfectly. In reality, an observation of the textured stainless steel pad revealed that there is small amount of bulging between up to 5 μm in height on the rim of the texture. Although this number is small in comparison to the

size of the texture, defects such as bulging have been seen to modify the friction behaviour [67].

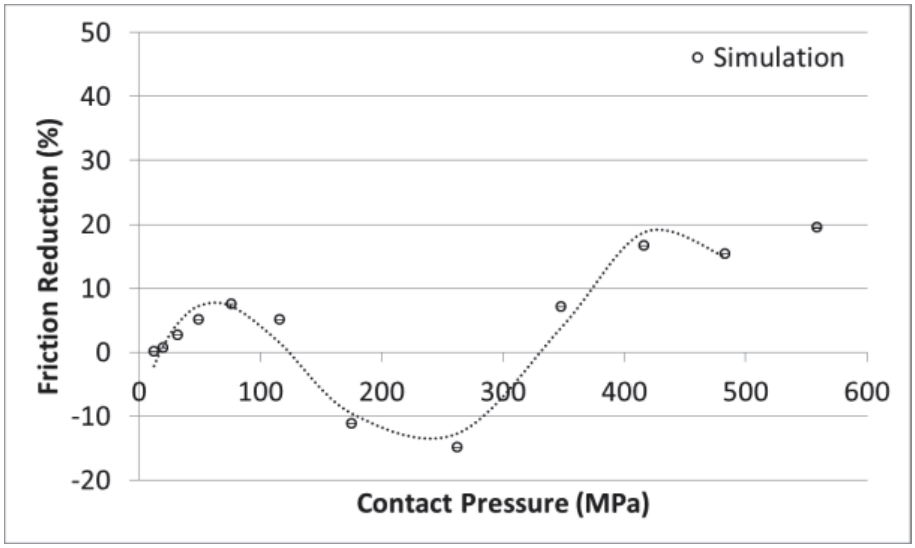


Figure 77: Friction reduction from the addition of surface texture (simulation)

Ultimately, although the range of effective pressure for surface texture P20 from the simulation is not exactly identical to the experimental results, the simulation results in general are able to capture the sinusoidal-like behaviour of the surface texture as friction control. Using the simulation, it was revealed that there is competition between the positive and negative effects of surface textures. On one hand, the surface textures create smaller friction bearing area in comparison to untextured surface, which results in lower sustainable friction during the contact. However, the surface texture creates irregularity of contact geometry which results in higher rate of material build up at the sliding front as illustrated through the simulation graphics in Figure 76.

Observing the simulation results, the friction reduction is positive at low pressure (<130 MPa), this is associated with the saturation of friction stress. At this region, the smaller contact surface in the textured pad limits the maximum sustainable friction in accordance to the general friction model definition. However, as pressure increases,

this positive effect is overpowered by the negative effect of deformation of the textured pad (Figure 76) which create material build up at the deformation front and hinder subsequent sliding. In short, throughout the contact pressure, there is competing physical effect of maximum sustainable friction and material build up at the sliding front (Figure 76). The stronger of the two effects then determines whether or not the texture produces positive effect at a particular contact pressure.

Meanwhile, the discrepancy between experiment and simulation is associated with the defects around the rim of the texture. Unfortunately, these defects are irregular in shape and hence the simulation of their behaviour is not straightforward. Through the experiment and simulation, it was concluded that the control and characterisation of surface defects during texturing are of high interest for research and the mechanism of the defect formation and its influence on friction is considered for future work.

## 5.4 Prediction of Copper Forming

### *5.4.1 Friction model*

The performance improvement created by the surface textures is highly dependent on the original friction behaviour of the untextured contact. In the steel to tool steel contact, the general friction factor, $\mu_{WB}$, is approximately 0.16. Because of this, in the pin on flat experiment, the surface textures produce limited friction reduction (at most 20% based on simulation using P20).

In contrast, according to the experimental results on microforming T-Shape test with copper, the unlubricated test resulted in friction factor, $m$, of 0.473. As the constant friction factor, $m$, generally overestimates the friction at lower pressure, the general

friction factor, $\mu_{WB}$, of 0.5 was used to predict texture performance with copper material.

As the workpiece material does not undergo significant bulk deformation, the shear strength $k$ in equation 1.5 is considered constant, i.e. $1/\sqrt{3}$ of the yield stress of the material. This friction model with $\mu_{WB}$ 0.5 is presented in Figure 78. The general friction model can be seen as conventional Coulomb friction model with constant $\mu$ for low contact pressure (up to 267 MPa for the current material), followed by a drop in $\mu$ as the friction stress remains constant with increasing contact pressure. The workpiece material used in the simulation follows the stress-strain relation shown in Figure 25 representing copper with yield stress of 178 MPa.

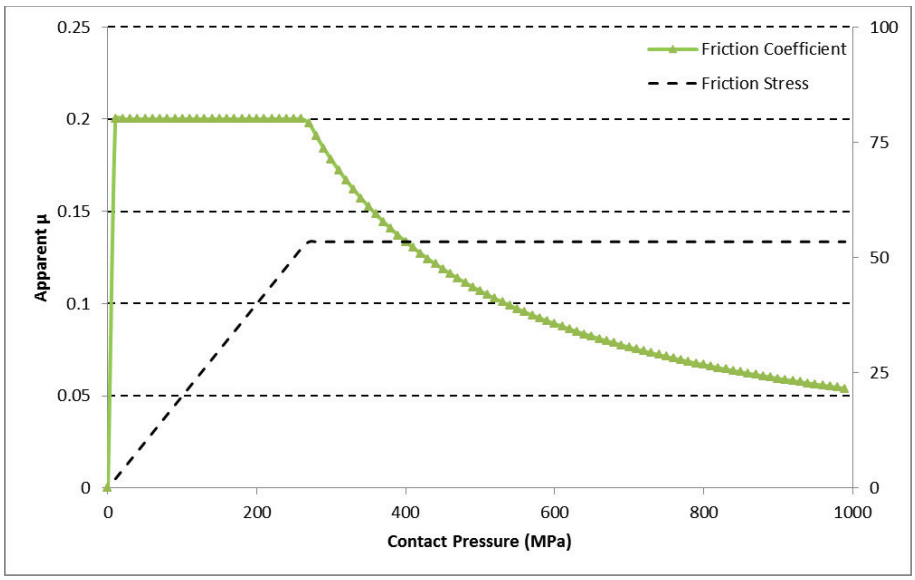


Figure 78: Friction model used in the surface texture simulation

### *5.4.2 Simulation setup*

Using Abaqus, the simulation inputs the material model, the friction definition for the flat surface and texture geometry in order to produce a new texture-dependent friction

definition. Four textured surfaces which represent two kinds of textures, and two texture densities each, were used in the simulation to represent the tool in microforming process. These surfaces were presented in Table 8. The textured surfaces were created using SolidWorks before importing into Abaqus.

Table 8: Textures used in the simulation

| Texture Notation | Geometry | Density | Illustration |
|---|---|---|---|
| P5 | Pore | 4.9% | 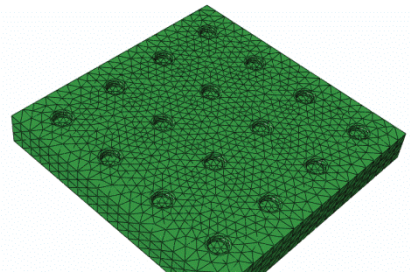 |
| P25 | Pore | 24.6% | 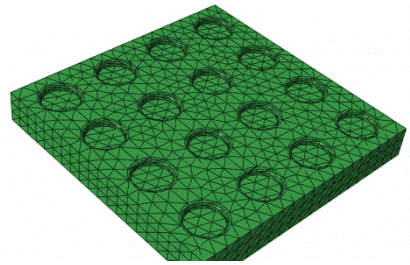 |
| X44 | Cross-channel | 43.8% | 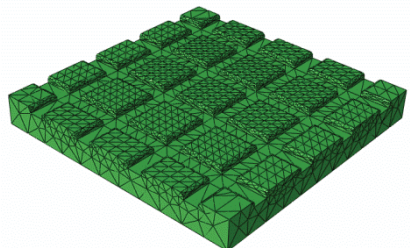 |
| X23 | Cross-channel | 23.4% | 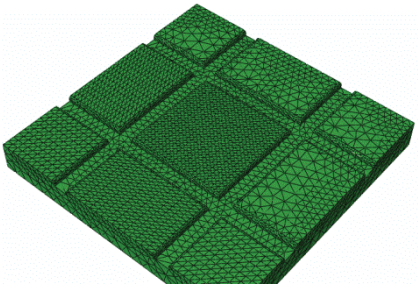 |

Similar to the pin on plate simulation, the workpiece mesh was pinned at the bottom (-Y face, see Figure 79). The periodic boundary condition was prescribed using zero-translation boundary condition at the +Z and -Z faces and using tie constraints at every mirroring nodes at the +X and -X faces such that the translation field in all three directions experienced at the +X face is also experienced at the -X face. The loading and sliding movement was set to the same parameter of 4% gradient as it is with the simulation in section 5.3. The simulation was repeated with a different displacement of the tool into the workpiece to provide prediction of friction behaviour at various contact pressures.

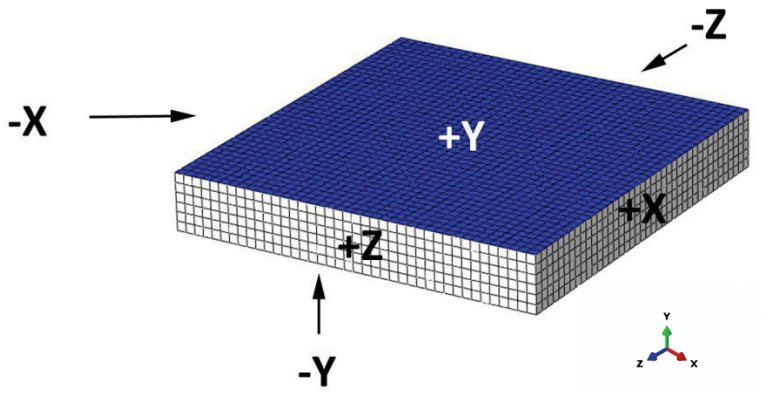


Figure 79: Full workpiece material mesh for surface texture simulation

The appropriate simulation domain for each texture was determined by simulating different element density (number of element for one texture period) and different number of textures included in the simulation. The objective was to determine the cost-effective simulation setup (specific to each texture) which gives representative results with minimum computation time.

## 5.5 Discussion

The pressure-dependent friction behaviour produced by the introduction of P5 texture is presented in Figure 80. The objective of introducing surface textures on the tool surface is to modify the friction behaviour to produce friction reduction in comparison to process with untextured tool surface. As shown in Figure 80, the friction reduction was visible for contact pressure higher than 180 MPa. The limit of surface texture effectiveness in this thesis was defined as the pressure at which the apparent coulomb coefficient, $\mu$, is at minimum. At pressure higher than this critical pressure, the texture acts as entrapment of material (illustrated in Figure 81) which results in friction increase and as a possible source of damage on the surface finish of the product.

This entrapment of material should not be confused with texture damage illustrated in Figure 76. Entrapment of material occurs at high contact pressure if the textured surface is harder than the smooth surface such in the case in microforming with textured die in which case the softer material gets embedded in the texture and hence called entrapment. On the other hand, texture damage (Figure 76) occurs when the textured surface is softer than the smooth surface. At high pressure, the harder smooth surface damages the softer, textured surface.

The simulation is considered finished at this critical pressure as subsequent data points cannot be considered reliable due to the severe mesh distortion associated with large local deformation. However, understanding the behaviour up to this critical pressure is considered adequate as the large local deformation is associated with material entrapment by the harder texture which seizes the die-workpiece interface.

In future work, this simulation can be extended beyond this critical pressure using remeshing and solution mapping technique. However, the extension of the simulation needs to be accompanied with damage criterion of the workpiece material. It is well understood that when the die-workpiece is seized, the (observed) friction is then governed by the shear property of the material. Therefore, the extension of the simulation needs better representation of the delamination and fracture of the surface material.

When the friction increase is not observed in the simulation, the critical pressure is defined as the pressure at which the texture is no longer producing lower friction in comparison to untextured surface. According to Figure 80, texture P5 is therefore considered useful for use between approximately 180 and 850 MPa.

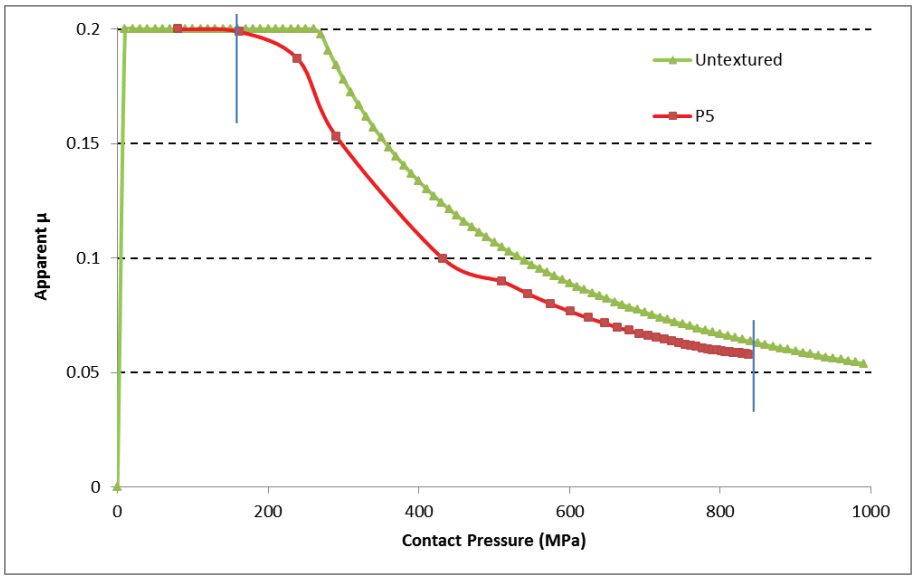


Figure 80: Friction behaviour produced by P5 texture

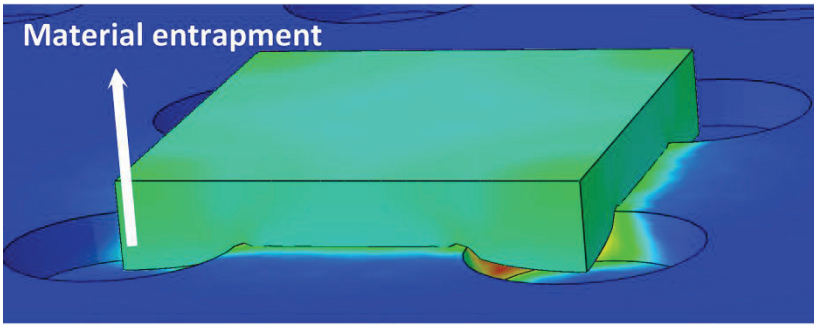


Figure 81: Illustration of material entrapment

Similarly, the pressure-dependent friction behaviour produced by the introduction of P25 texture is presented in Figure 82. In comparison to the P5 texture, the P25 produces greater friction reduction from the untextured tool with the expense of more narrow friction reduction window. The P25 texture is considered effective for friction reduction (for the copper material) when it is used between approximately 150 to 450 MPa.

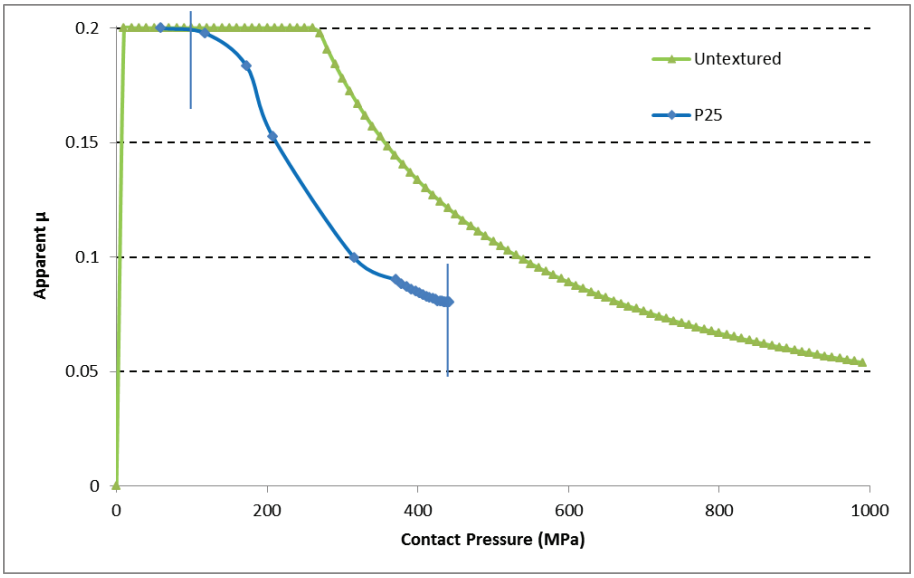


Figure 82: Friction behaviour produced by P25 texture

Figure 83 shows the percentage of friction reduction across the range of contact pressure. It is shown in general that surface with higher texture density produces the larger friction reduction. This is caused by the friction model included in this simulation (general friction factor). As the *actual* contact surface reduces for P25, the limit of friction force which can be sustained in a given *apparent* surface area is reduced. This is similar to the traction comparison between road and track tyres. Consequently, however, P25 surface with higher texture density is more susceptible to workpiece material entrapment which limits its friction reduction effectiveness range.

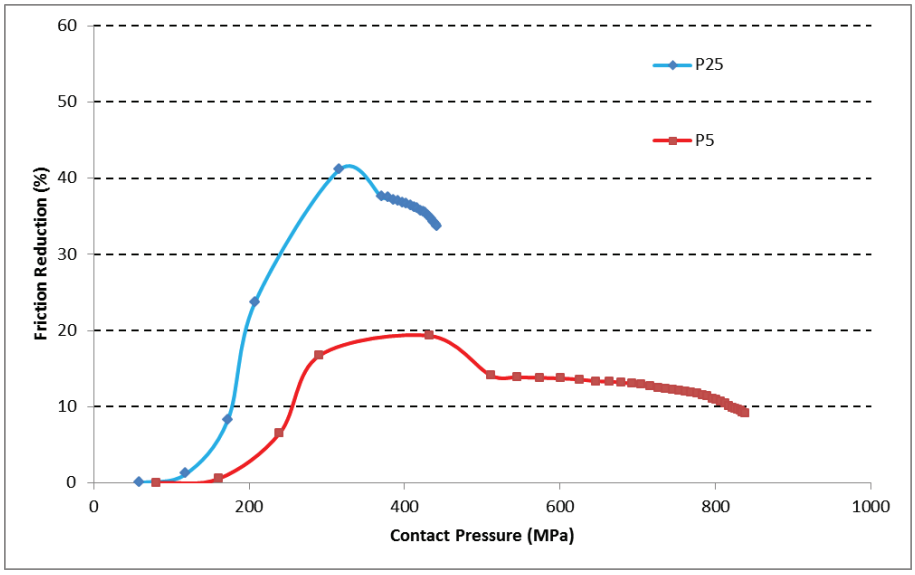


Figure 83: Comparison of friction reduction between P5 and P25

Similar simulation setup was used to examine the influence of introducing cross-channel textures. The pressure-dependent friction behaviour produced by the introduction of X44 texture is presented in Figure 84. Texture X44 is considered useful for use between 50 and 300 MPa as it shows friction reduction at this range of pressures.

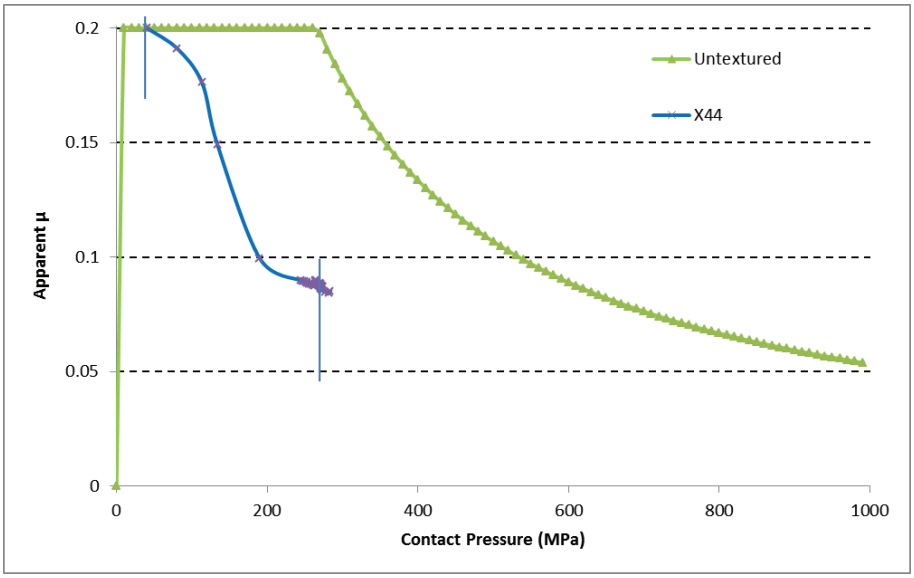


Figure 84: Friction behaviour produced by X44 texture

Meanwhile, the pressure-dependent friction behaviour produced by the introduction of X23 texture is presented in Figure 85. In comparison to the X44 texture, the X23 produces smaller friction reduction from the untextured tool but with wider friction reduction window. The X23 texture is considered effective for friction reduction when it is used between 100 to 550 MPa. As the simulation was only conducted using a single material and its corresponding general friction factor, it was not possible to conclude a general surface texture performance with respect to the material property such as yield stress. In future study, multi-material simulation is needed so as to understand the effects of material property to texture performance.

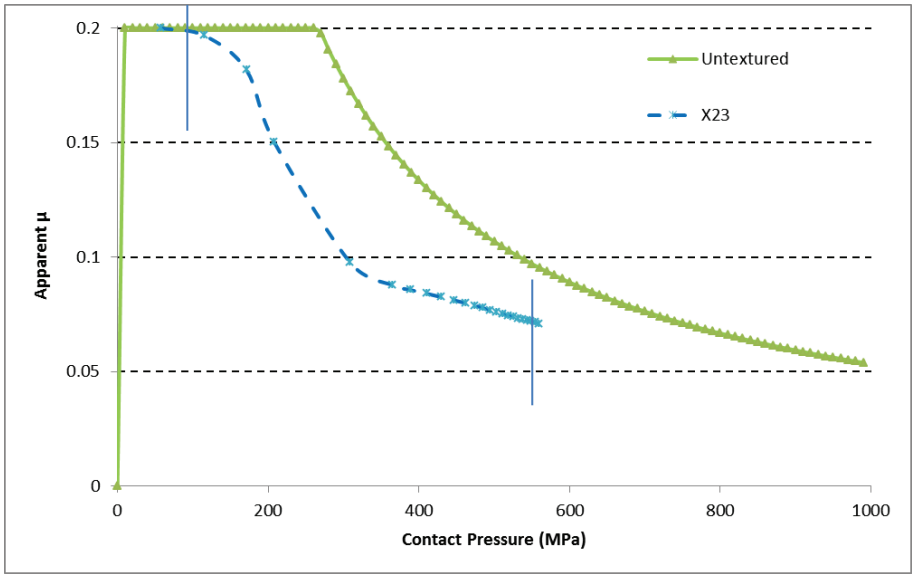


Figure 85: Friction behaviour produced by X23 texture

Figure 86 shows the percentage of friction reduction across the range of contact pressure for X44 and X23. While the general behaviour is similar to that of pore texture, friction increase attributed to the material entrapment in cross-channel textures is lower than that of the pore texture as presented in Figure 87. In Figure 87, the P25 has marginally higher texture density (24.6%) in comparison to X23 (23.4%). Therefore considering the maximum sustainable friction, the geometry which allows greater contact patch (X23) should produce marginally smaller friction reduction. However, the reverse is observed from the simulation and this is caused by the difference in texture geometry. When pore texture is used, subsequent sliding between the surfaces needs to overcome the total material entrapment in the pore. However, when cross-channel texture is used on the tool surface, the sliding of the surface needs to overcome the material entrapment only in channels perpendicular to the sliding direction. As a result, not only does X23 produce greater friction reduction, but also wider range of effectiveness.

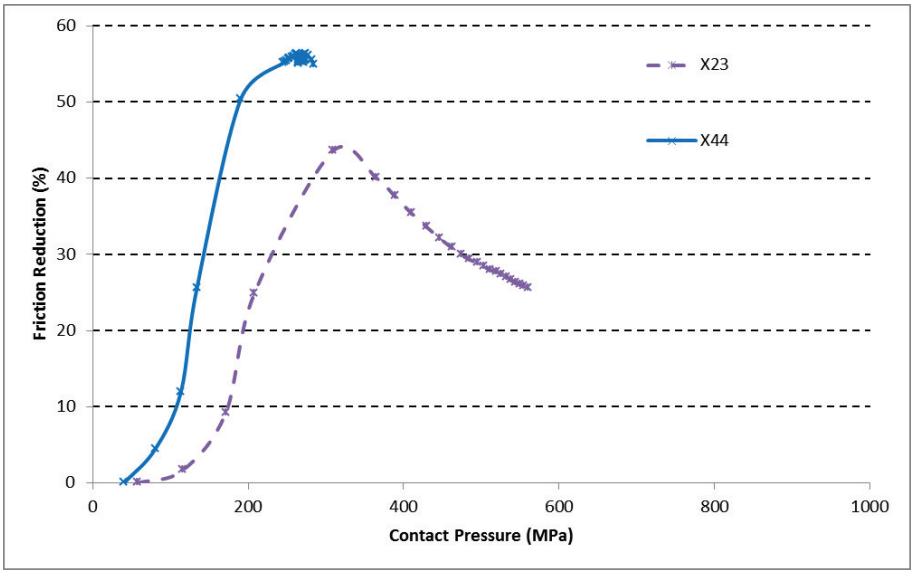


Figure 86: Comparison of friction reduction between X44 and X23

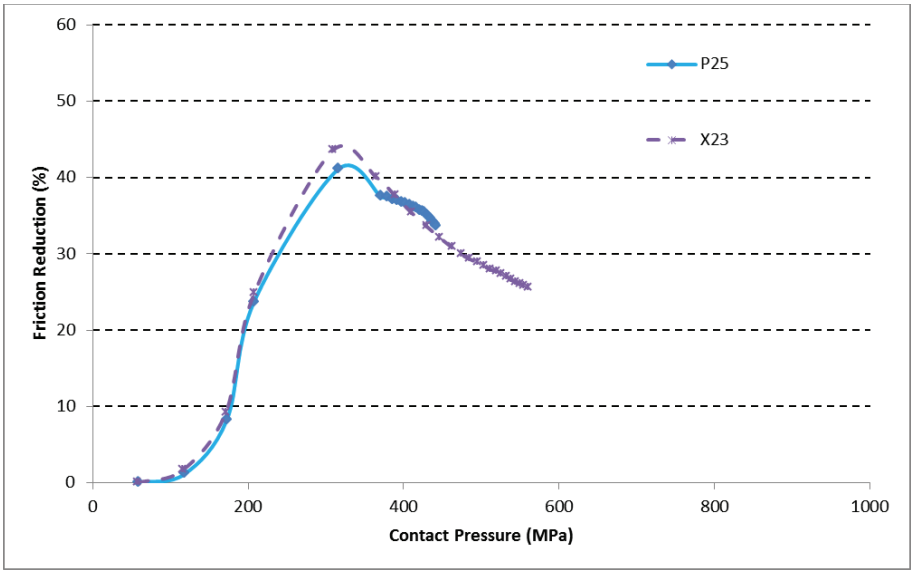


Figure 87: Comparison of friction reduction between P25 and X23

## 5.6 Closing Remarks

The simulation on surface textures provided clarification of the role of surface textures in metal forming which can be attributed to the general friction model definition. Although other arguments of the mechanisms of friction reduction such as lubricant entrapment, wear particle entrapment, etc. may be accurate, the main

mechanism for friction reduction by surface textures is that the surface texture limits the friction force which can be sustained by the same *apparent* surface area, which is related to the shear strength of the material itself.

In reality, there is a competing physical effect of the limit of friction stress and the entrapment of material in the texture. These competing physical effects create a sinusoidal-like friction reduction for the pin on plate setup (low $\mu_{WB}$) while they create two distinct regions at low and high contact pressure, respectively, for the copper forming simulation. The difference in overall effect is derived from the difference in the deformation behaviour. In the pin on plate test, the negative effect is attributed to the deformation of the softer pad material, creating material build up which hinders subsequent sliding. In the copper forming simulation, the negative effect is caused by the entrapment of the softer copper material in the texture.

As for the discrepancy between the experiment and simulation results of the pin on plate setup, it can be attributed to the irregular bulge created around the rim of the individual texture, which is missing from the simulation.

Ultimately, FE simulation was used here as a tool to examine closely the performance of surface textures of different geometry and size. Generally, low texture density produces a modest friction reduction but wide range of application pressures while high texture density produces more significant friction reduction but narrow range of usable pressure range. The same examination could not be done using experimental method.

With the simulation findings, it is suggested that it is possible to design tooling surface textures to lower overall friction in microforming in place of lubricant. At the

pinnacle of the surface texture design, it will be possible to design microforming die with specific textures for different section of the die according to metal flow direction and contact pressure. The outlook towards mapping die surface textures is also shared in a 2013 study by Scaraggi et al. [130].

Other work on the subject has established that very small surface textures such as by the addition of nano-particles using self-assembled monolayer primer can also be used when it is desirable [131]. This can be very useful in producing even smaller microformed part and nanoformed features and the development on this approach can be considered for future work.

The use of surface textures in recent years have also grown to accommodate and sustained densely packed solid lubricants on the surface [132, 133]. Solid lubricants in general do not possess sufficient adhesion to the substrate. Surface textures are therefore used to enable better adhesion to surfaces.

Another recent work also suggested that surface texturing can be designed not only to improve tribological properties directly but also through the modification of the material properties of the material especially near the surface [134]. As such, the surface texturing can benefit both tribologically (i.e. reduce contact area) and mechanically (e.g. surface hardening, improve wear and corrosion resistance).

# CHAPTER 6 DEPTH-DEPENDENT STRESS-STRAIN RELATION

## 6.1 Background

For conventional metal forming processes, the FE simulation generally uses the continuum material model where the stress ($\sigma$) is a function of the strain ($\varepsilon$), the strain rate ($\dot{\varepsilon}$) and the temperature ($T$). However, for smaller size deformation, various simulation approaches have been attempted such as the crystal plasticity simulation [29, 135, 136] and the gradient-dependent plasticity simulation [32, 137] in order to provide better process prediction.

This chapter proposes an approach to account the effect of strain gradient to mechanical properties of materials [138] which contributes to the size effects using FE simulation through a modified continuum model in order to avoid performing the more computationally-exhaustive crystal plasticity or gradient-dependent plasticity simulation for use in microforming prediction. With the inclusion of strain gradient model, the mechanical properties of materials at and near the surface is significantly affected, resulting in shift in surface behaviour. While this shift of surface behaviour is not large enough to influence the overall process behaviour in metal forming, the process behaviour in microforming with much smaller workpieces is significantly affected due to the larger surface area to volume ratio.

In a previous study with conical asperity [139], it was shown that the measured friction during the simulation is lower when the DSS is introduced. More importantly, the influence of ISE model is stronger in smoother surface. The current study aims to develop further the DSS model and provide validation to the strain gradient friction model.

## 6.2 Simulation

### *6.2.1 Indentation size effect*

Along with the growing interest in recent years for micro- and nano-structures such as thin films, micro-wires, flexible electronics and fibre composites, there is increasing interest in understanding the mechanical properties of materials at very small scale. Experiments in micro- and nano-indentation test have revealed the dependency of material hardness on the size [138] and shape [140] of the indentation. Nix and Gao [138] proposed a mechanism-based model (Equation 6.1) which agrees to micro-indentation results by considering the development of geometrically necessary dislocations (GND) and statistically stored dislocation (SSD) during deformation by a conical indenter. In the model, the hardness at the indentation depth of interest ($H$) can be related to the indentation depth ($h$) through experimentally determined constants of the bulk hardness ($H_0$) and the material length scale ($h^*$) which are material dependent.

$$\frac{H}{H_0} = \sqrt{1 + \frac{h^*}{h}} \qquad 6.1$$

This phenomenon is known as the Indentation Size Effect (ISE) and linked to strain gradient plasticity. However, experimental results from nano-indentation at very small indentation depth have shown significant deviation from the model of Nix and Gao. Consequently, models have been proposed to account and explain this deviation using different indenter geometries, at different indentation depths and with different materials [141-143]. In general, the hardness at shallow indentation (using nano-

indentation tests) is lower than the value suggested by Nix and Gao.

Qiu et al. [144] proposed that when dislocation is considered, the effect of material friction stress ($\tau_0$) should not be ignored and the complete Taylor's equation of shear flow stress (Equation 6.2) should be considered. In equation 6.2, $G$ and $b$ are shear modulus and Burgers vector, $\alpha_T$ is a proportionality constant and $\rho$ is the dislocation density (SSD and GND). The material friction stress was not considered in Nix and Gao model as the materials in observation were copper and silver. However, for BCC metals and other materials with strong covalent bonds, the material friction stress is significant. Equation 6.2 essentially separates the flow stress from dislocation from those otherwise. As a result, the ISE equation from Qiu et al. contains a threshold hardness value related to the flow stress not attributed to dislocation generation (denoted $Y$, Equation 6.3). It was proposed that for FCC metals, the $Y$ should be negligible and hence the equation reverts to Equation 6.1.

$$k = \alpha_T G b \sqrt{\rho_S + \rho_G} + \tau_0 \qquad 6.2$$

$$\frac{H - Y}{H_0} = \sqrt{\left(\frac{H - Y}{H}\right)^2 + \frac{h^*}{h}} \qquad 6.3$$

The size of the plastic zone was further studied in the work by Feng and Nix [143]. This deviation has been attributed to a difference in formation and arrangement of GND and SSD from very small deformation in nano-indentation test. The motivation for the work was to provide other explanation for the lower hardness at very shallow indentation. The explanation by Qiu et al [144] was considered inadequate by Feng and Nix [143] as the lower hardness at very shallow indentation applies not only to

BCC metals but also in FCC metals. A coefficient which represents plastic zone growth, $f_{pz}$ (Figure 88), was included into the ISE equation (Equation 6.4). It was also determined that the plastic zone can grow up to 66% larger ($f_{pz}$ = 1.66) than the contact for MgO at the surface ($h \rightarrow 0$) and 71% ($f_{pz}$ = 1.71) for iridium (FCC metal) [143].

$$\frac{H}{H_0} = \sqrt{1 + \frac{h^*}{f_{pz}^3 h}} \qquad 6.4$$

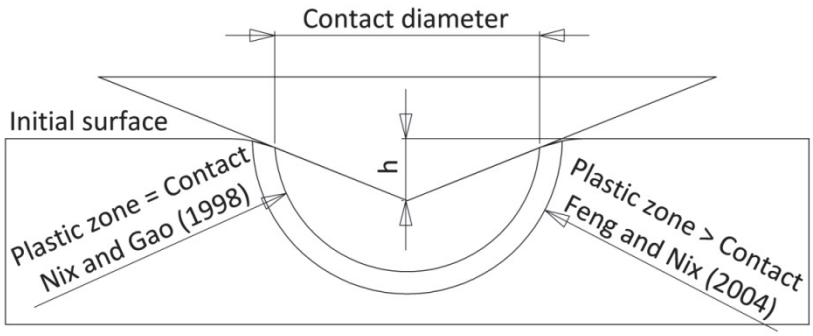


Figure 88: Plastic zone growth

Chicot [142] proposed a bi-linear equation to treat micro-indentation and nano-indentation separately. In the model, micro- and nano-indentation regimes were treated using two separate Nix and Gao type equations. Each regime was then assigned different values of $H_0$ and $h^*$ to fit the experimental results for the entire range of the indentation tests. The two indentation regimes were further proposed to be renamed as uniform dislocation spacing (UDS) and non-UDS regimes for micro- and nano-indentation, respectively. In the micro-indentation, the plastic zone (zone of GND development) diameter is equal to the contact diameter. The same does not apply in nano-indentation or non-UDS regime. However, the bi-linear equation was proposed with inadequate physical explanation for the difference in constants for the

two regimes.

The model of Abu Al-Rub [145] has been proven reliable to predict the ISE of various metals through micro- and nano-indentation experiments and it includes physical meaning of variables as have been considered in previous studies. It is therefore used in the current investigation. In general, Abu Al-Rub model considers both a threshold hardness value as well as the growth of plastic zone. In addition, similar to the observation by Feng and Nix, the growth of the plastic zone was also related to the indentation size (or depth) through the dislocation coupling coefficient, $\beta$. The main difference between Nix-Gao and Abu Al-Rub model is presented in Table 9. The present work treats surface asperities of metal forming tool as indenters in hardness testing.

Table 9: ISE formulae of Nix-Gao and Abu Al-Rub

| | Nix and Gao [138] | Abu Al-Rub [145] |
|---|---|---|
| ISE Formula | $\frac{H}{H_0} = \sqrt{1 + \frac{h^*}{h}}$ | $\frac{H - Y}{H_0 - Y} = \sqrt[\beta]{1 + \left(\frac{h^*}{h}\right)^{\beta/2}}$ |

### *6.2.2 Simulation setup*

Friction involves the presence of roughness convex and concaves on contacting surfaces, called asperities (Figure 89). This asperities distribution generally governs the real area of contact which is generally much smaller than the apparent area of contact [146]. The large number of asperities during surface to surface contact was then used to justify that the friction coefficient during continuous sliding can be attributed to the averaged behaviour of the interaction between asperities, from initiating contact to deformation to separation. Green [147] used this assumption to

develop the basis of friction simulation involving asperities in which friction can be modelled using two asperities (one from each surface) undergoing the full cycle of asperity interaction (initiating contact to deformation to separation). The averaged tangential and normal forces derived from this simulation were therefore extracted as the frictional properties.

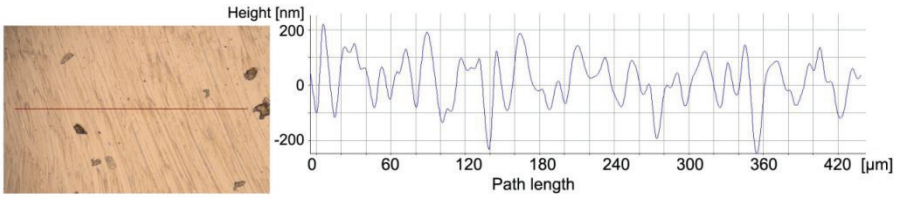


Figure 89: Surface profile of the polished steel pin

This modelling approach is valid with the assumption of uniformity among asperities including their mechanical properties. Mulvihill et al. [148] provided good summary on the development of researches on friction simulation using this approach. However, the modelling approach has a setback: the resulting friction predicted from the simulation generally suggests values which are much lower compared to experimental results from metal to metal contacts. In order to generate simulation results in better agreement with experiments, researchers generally used the Coulomb friction coefficient to offset for the higher friction observed in experiments. Such incorporation of Coulomb friction coefficient as additional friction definition in order to offset the simulation results is generally inaccurate as the Coulomb friction law was derived from macroscopic experiment whereas the microscopic simulation using asperities was initiated to understand the mechanism of macroscopic friction.

Instead of using the averaged transient process of contact initiation to deformation to separation, the simulation in the current work uses steady state sliding of two surfaces

with appropriate material definition to generate the friction behaviour. As the current investigation is aimed to address medium to high contact pressure problems such as those occurring in metal forming, the simulation work was designed to use single-sided asperity contact. The harder surface during metal forming contact, the tool, was prescribed with one asperity while the workpiece was represented by a smooth surface. This configuration is adequate for metal forming purpose as the workpiece surface is usually much softer than the tool surface. In which case, the workpiece will copy the surface roughness of the tool.

Generally, at medium to high pressure contact during metal forming, the two materials can have a full contact in which the real contact area equals the apparent contact area [102] and therefore the final surface profile (after contact) of the workpiece is more important than the initial surface profile (before contact) and the definition of asperities on the workpiece surface has little meaning.

The yield stress of a material is generally accepted to be proportional to its hardness, with the correlation factor ($x$ in Equation 6.5) varies from 2.5 to 3.0 for most metals. This correlation factor was initially governed for large sample, i.e. indentation size much smaller than specimen size. Chen and Tsai further extended this validation for small specimen of few millimetre dimension [149]. However, although the correlation factor can estimate the flow stress of the material, it is not sufficient to create the complete stress-strain relation at different depths from the surface.

Tabor [150] suggested a method to construct stress-strain relation from a series of hardness testing by assuming the true strain during indentation as proportional to $d_c/D$, with $d_c$ the contact diameter and $D$ the ball diameter for spherical indenter (Equation 6.6) if the strain hardening exponent, $n$, is known. However, implementing

this conversion is not possible because: a) increasing $d_c/D$ to get larger strain would result in increasing indentation depth, which is known to affect the measured hardness, and b) the maximum $d_c/D$ is limited to 1 which is equivalent to a true strain of 0.2.

$$H = x\sigma_y \tag{6.5}$$

$$p \approx 3\sigma_y \left(0.2\frac{d_c}{D}\right)^n \tag{6.6}$$

$$\sigma(\varepsilon, h) = \sigma(\varepsilon) * \frac{H}{H_0}(h) \tag{6.7}$$

As there is no systematically established method to create the stress-strain relation over large range of strain from hardness testing, the current study assumes that the bulk of the workpiece has the property of a typical copper material as has been used in 3D simulation in Chapter 4 (see Figure 22). This stress-strain relation is further multiplied by the depth-dependent coefficient $H/H_0$ presented in Figure 90 to create the DSS relation of the material ($\sigma(\varepsilon,h)$, Equation 6.7). The complete procedure used in the current study is presented in Appendix C.

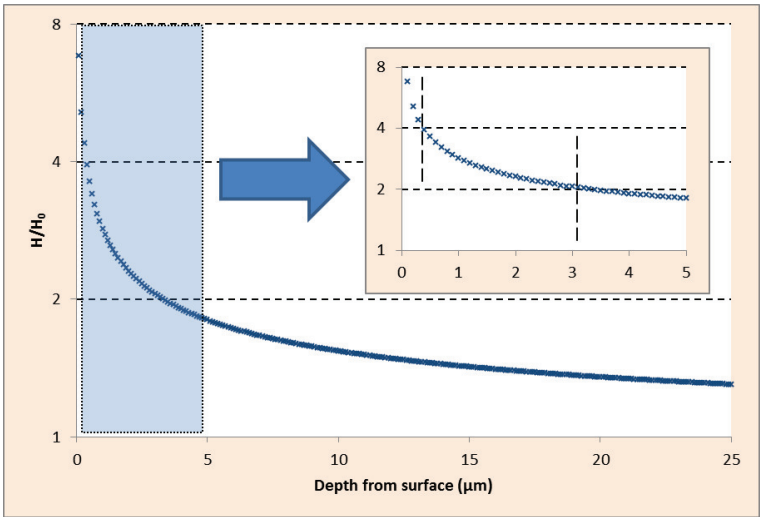


Figure 90: DSS relation coefficient

The DSS relation coefficient was derived using the ratio between the measured hardness and the bulk hardness, $H/H_0$, from the work by Abu Al-Rub [145] for copper (Figure 90). The work reveals that the relative hardness ($H/H_0$) doubles at approximately 3 µm from the surface. The effect exponentially increases for region nearer to the surface with the relative hardness quadruples at approximately 0.4 µm. The mechanical properties for the first 3 µm from the surface is highly important with respect to friction as it is within range of naturally formed asperity size from surfaces made through machining processes and polishing.

The interaction between the tool and workpiece was specified as frictionless since adhesive friction is ignored in the current examination. Adhesive friction can be included by considering micro-welds formation during contact and can be included through fixed shear strength which corresponds to the stress required to break the micro-welds. However, the appropriate magnitude of the fixed shear strength can only be determined empirically by comparing experimental results with simulation with various fixed shear strength.

In the simulation, 3D workpiece domain adapted from the 2D friction reading mesh of Stupkiewicz [151] as illustrated in Figure 91 was used to investigate the influence of surface roughness on sliding friction.

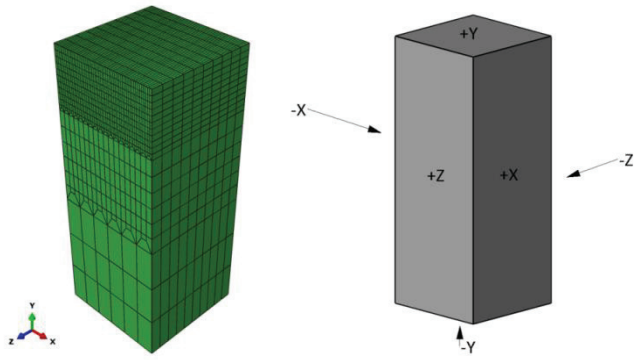


Figure 91: Full workpiece material mesh and assignment of faces

The tool surface in the simulation (Figure 92) is designed to have a periodic array spherical asperity with the period of 10 µm in x- and z-direction. Because of the assumed periodicity, the simulation domain is selected as 10 x 10 µm with the necessary periodic boundary conditions applied. The simulation domain has a thickness of 25 µm and this thickness is considered adequate for good representation of the DSS relation as it covers the range of depths with steep $H/H_0$ gradient (Figure 90).

The level of surface roughness is created by changing the radius of the spherical asperity (Table 10). The surface roughness used in this simulation was approximately Sa 0.5, 1.0 and 2.5 µm representing polished surface, ground surface and rough surface, respectively. Areal roughness parameter, Sa, was used instead of the more common linear roughness parameter, Ra, in order to provide better definition for the whole area of contact in the simulation. Inclusion of other surface profile parameters (e.g. skewness, kurtosis, density of asperities) would create more accurate

representation of actual surfaces. However, this inclusion requires larger simulation mesh to constitute representative volume elements and this was not the focus of the current study.

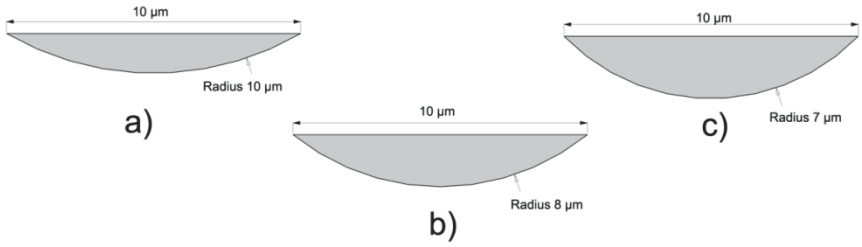


Figure 92: Tool material domain for: a) Sa 0.5, b) 1.0 and c) 2.5 µm

Table 10: Conversion of surface roughness to asperity radius

| Surface roughness (Sa, µm) | Equivalent spherical asperity radius (µm) |
|---|---|
| 0.5 | 10 |
| 1.0 | 8 |
| 2.5 | 7 |

FE code Abaqus was used for the modelling. Due to the demanding contact calculations, the Abaqus/Explicit was used. The simulation used linear hexahedral elements with reduced integration for the workpiece and rigid body elements for the tool. Both bodies are prescribed with concentrated elements surrounding the contact area. The temperature degree of freedom was used to provide *pseudo* temperature-dependent mechanical properties to describe mechanical properties at different depth from the surface. Prior to the analysis step, the workpiece mesh was prescribed heat and cold sink boundary conditions and it was allowed to generate constant gradient of temperature across the thickness. In this simulation, the region closer to the surface is

set with cold sink boundary condition representing the harder volume due to the DSS relation coefficient and the region farthest from the surface is set with heat sink boundary condition representing the softer volume (material property leaning towards the bulk material).

In a similar manner as the simulation in Chapter 5, the workpiece mesh was pinned at the bottom (-Y face). The periodic boundary condition was prescribed using zero-translation boundary condition at the +Z and -Z faces and using tie constraints at every mirroring nodes at the +X and -X faces such that the translation field in all three directions experienced at the +X face is also experienced at the -X face. The contact pressure was produced by moving the tool into the workpiece (-Y direction). Afterwards, the tool is prescribed with a sliding movement parallel to the workpiece surface (+X direction) and the reaction forces along X and Y directions were recorded to produce normal and friction stresses. The simulation was repeated with a different displacement of the tool into the workpiece to provide prediction of friction behaviour at various contact pressures.

Tool steel pin on copper flat tribometer experiments were performed alongside the simulation to provide verification for the model. The pins are produced with circular contact of 1 mm diameter as has been illustrated previously in Figure 67. The small contact diameter was necessary to reduce the tribometer load required to create high contact pressure which is the interest in metal forming. The pins were supplied with two kinds of surface finish: polished and ground using 600-grit sand paper. The surface roughnesses of the pins are 0.4-0.5 μm and 0.9-1.0 μm, for polished and ground pins respectively. The tribometer experiment is conducted at room temperature and ambient humidity (80-95%). The simulation considers solely the

friction behaviour during ploughing friction without the presence of third body particles or friction heating. In order to produce the most representative experiment to this simulation, the experiment in this study involves only a one-time sliding on fresh samples with sliding speed approximately 0.1 mm/s. The one-time sliding is chosen as repetitive sliding between surfaces is likely to produce third body particles through surface shearing and sub-surface cracking [81, 129]. Slow sliding speed further minimizes the production of heat on the surface due to friction [152] which is not currently considered in the simulation.

## 6.3 Discussion

Figure 93 shows the simulation results using DSS model for Sa 1.0 μm and tribometer experiment using ground pin. Figure 93 showed an increase of coefficient of friction with increasing contact pressure which is in agreement with the observation of Mulvihill et al. [148] in which the coefficient of friction increases with the amount of asperity overlap. In the current study, the changing contact pressure was obtained by introducing a known deformation depth from the asperity, which is equivalent to the asperity overlap in the simulation works inspired by Green [147].

Unlike the simulation results, experiments do not result in an increase of friction with contact pressure. This can be explained because the current simulation was aimed specifically to examine the influence of the DSS relation on friction based on asperity deformation mechanism whereas friction in experiments also includes aspects such as adhesion and steady-state surface degradation. The large error bar in the experimental results for ground pin is attributed to the significant stick-slip behaviour between the pin and plate.

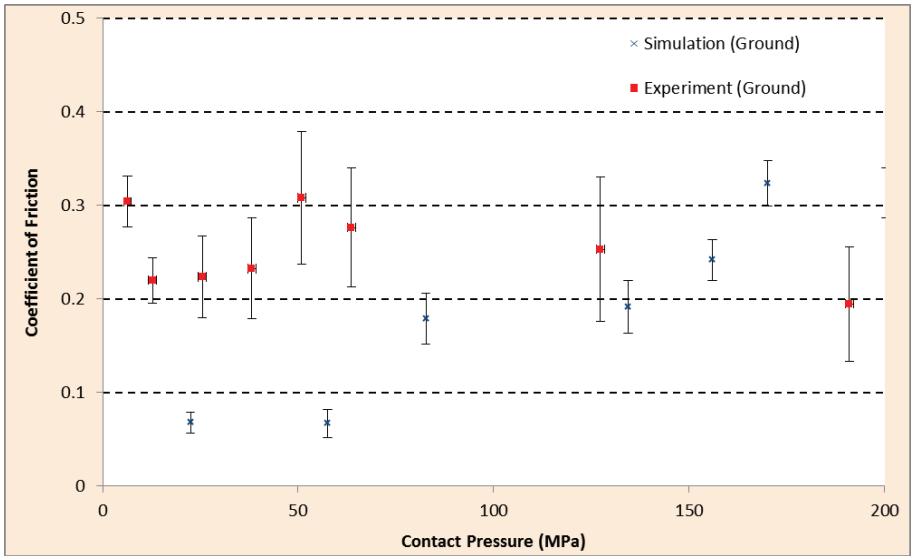


Figure 93: Simulation (DSS) and experimental results for ground surface

The agreement between simulation and experimental results is excellent in the case of polished pin (Figure 94) and the error bar from the experiment is significantly smaller due to the reduced stick-slip behaviour.

The accuracy of the model in relation to experimental results was considered better than the simulation without DSS properties. The non-DSS simulation overestimated friction coefficient as illustrated in Figure 95. In addition, both experimental and simulation results with DSS for the polished surface showed a weaker trend of increasing friction coefficient with contact pressures.

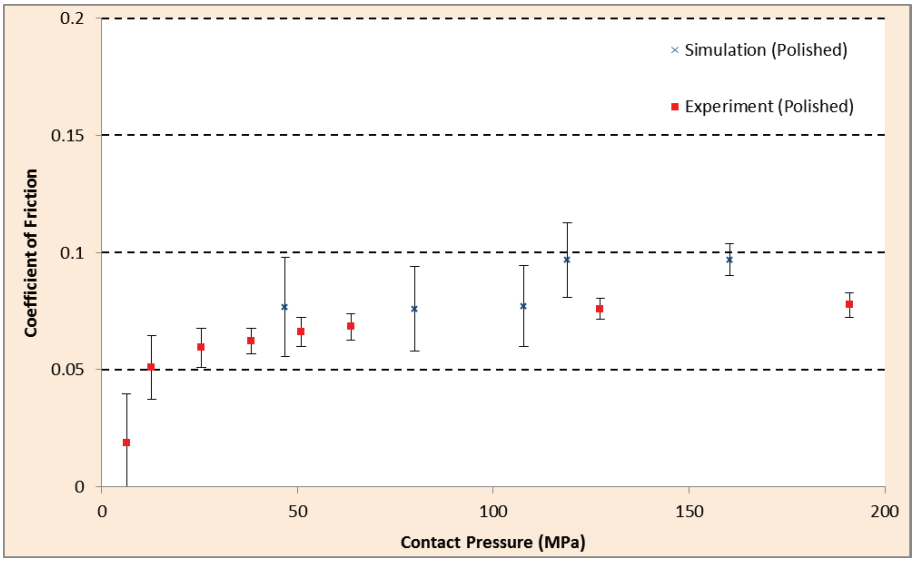


Figure 94: Simulation (DSS) and experimental results for polished surface

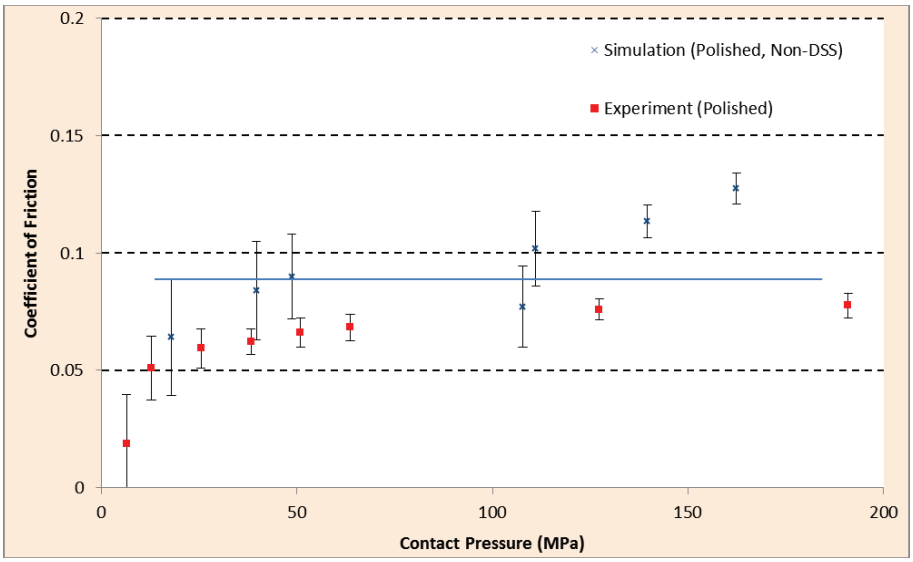


Figure 95: Simulation (non-DSS) and experimental results for polished surface

Ultimately, the DSS simulated rough surface suggests that there is no significant friction influence between tool surface with Sa 1.0 and 2.5 μm as presented in Figure 96.

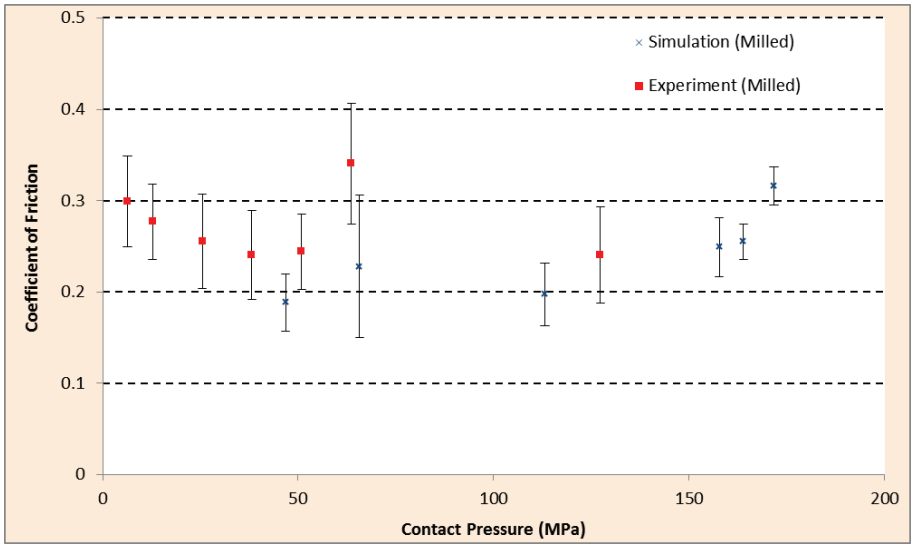


Figure 96: Simulation (DSS) results for rough surface

## 6.4 Application to Metal Forming Simulation

In order to illustrate the influence of the DSS model on a metal forming process, additional simulation on an actual metal forming geometry was performed on Deform-3D 6.9. The Deform-3D analysis code was selected because its simulation algorithm (e.g. remeshing, solution mapping) has been optimized to simulate large deformation in metal forming.

The role of FE simulation in metal forming design has been crucial with the initial purpose of determining the suitable size and shape of metal forming preform [153, 154]. With the vast improvement in computing power over the past decade, the use of FE method in metal forming design has extended to other purposes such as forming limit [155, 156] and springback analysis [157-159], damage prediction such as wrinkle in sheet metal forming [160] as well as non-isothermal process design [161].

The modified T-Shape test [121] was selected as the simulation aims to identify the effect of the changing friction behaviour from DSS. The modified T-Shape test is a

friction test designed for friction investigation in microforming. As such, it has great sensitivity to friction and is therefore very effective in demonstrating the influence of changing friction behaviour from current study on DSS mainly through the differential metal flow behaviour.

The simulation method follows the 3D simulation parameters applied in Chapter 4. As for the friction definition, the Deform-3D simulation compared the two averaged friction coefficients obtained from the Abaqus simulation for the polished surface: a) with DSS model and b) without DSS model (conventional continuum simulation).

However, the current simulation is limited to contact pressure to up to 200 MPa and was focused on the shift of behaviour attributed to the addition of DSS model. For higher contact pressures, it was suggested by the work of Wanheim et al. [56] and Petersen et al. [102] that the concept of constant coefficient of friction (or Coulomb friction) does not apply in high contact pressure.

In Coulomb friction, the friction stress is proportional to the contact pressure thus yielding a constant friction coefficient. However, there is a proportionality limit to this Coulomb friction, which is further governed by the law of 'general friction' [102]. This law dictates that when the friction stress saturates when $p/2k$ exceeds 1.3with $p$ and $k$ correspond to the contact pressure and the yield stress of the material in pure shear, respectively. In which case, the DSS model can be applied up to contact pressure $2.6k$, beyond which the general friction (or its gradient-dependent derivative) should apply.

In the friction definition, the proportionality limit of friction stress was determined at 267 MPa of contact pressure, which corresponds to the $2.6k$ of the copper material

being investigated. Hence in the Deform-3D simulation, the friction definition used was therefore reconstructed in Figure 97 with the averaged coefficient of friction from DSS simulation prescribed up to 267 MPa and the extrapolation using general friction was made for contact pressures higher than 267 MPa.

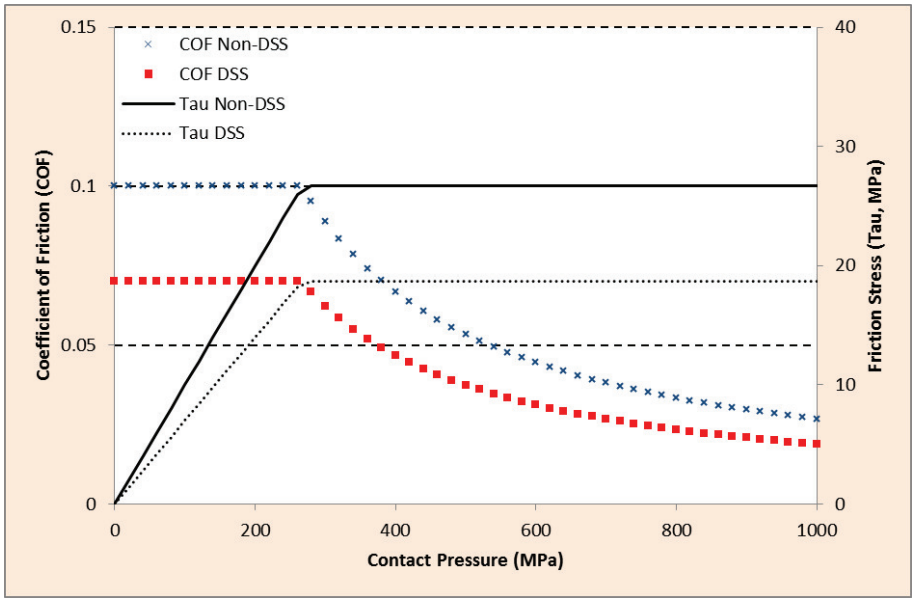


Figure 97: Friction definition used in the Deform-3D simulation

As the DSS model has been validated using tribometer experiment, the Deform-3D simulation is now aimed to demonstrate behavioural shift affected by the change of friction definition from the DSS model. As illustrated in Figure 98 and Figure 99, when the simulation uses friction definition derived from DSS simulation, it predicts the material flow differently, i.e. lower total height at the same flange height in modified T-Shape test.

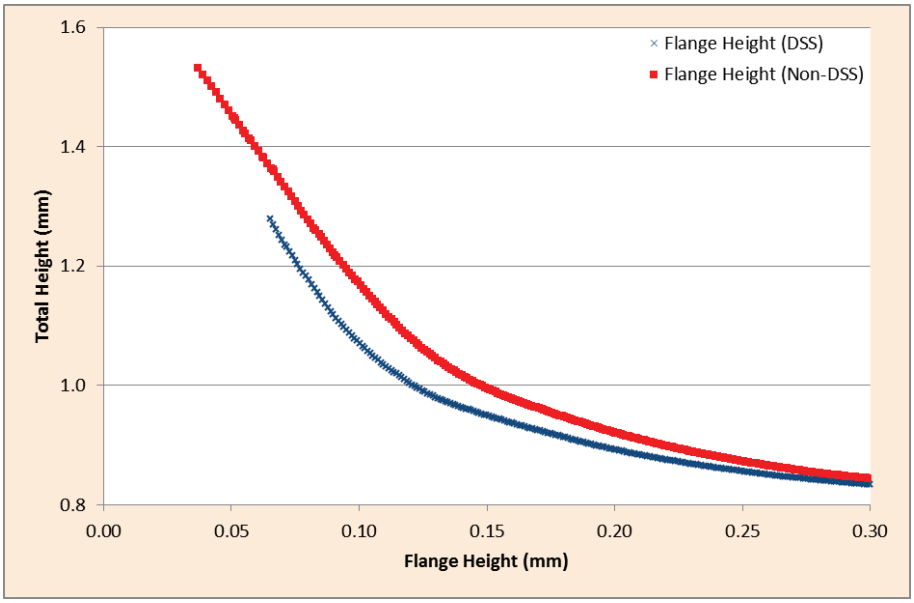


Figure 98: Change in geometry development in T-Shape test

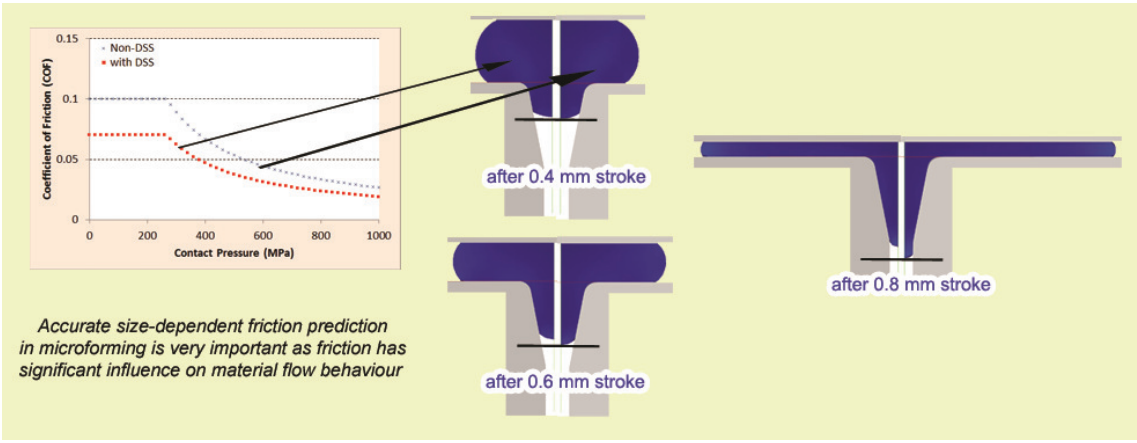


Figure 99: Part geometry difference due to friction

The DSS model in general affects only the surface with the region within 3 μm from the surface having the largest effect. It was derived from hardness testing of specimens with its thickness much greater than the indentation depth. Therefore, further hardness testing experiments will help to understand the ISE behaviour when the indentation depth becomes comparable to the specimen thickness.

However, as understood in the current study, the DSS model is more accurate in predicting friction behaviour in tribometer experiment. When it is used in microforming simulation, DSS provides different metal flow prediction, which can be used to provide a size-dependent metal flow prediction, especially when the thickness of the workpiece material becomes comparable to the DSS affected depth.

## 6.5 Closing Remarks

The depth-dependent stress-strain (DSS) modelling approach was developed for friction prediction simulation especially for microforming application where the shift of surface behaviour can affect the overall process behaviour significantly due to the very small workpieces. The model was presented as an alternative to asperity simulation approach by Green which generally underestimates the amount of friction in metal to metal contact.

The current DSS model showed satisfactory agreement when it is compared with tribometer experimental results for polished and ground surfaces even without artificial implementation of friction coefficient. It is also noted that in comparison to the DSS model, the conventional continuum model overestimates friction when used with single sided asperity contact.

Ultimately, a complete metal forming simulation approach based on DSS model and a shift in metal flow preference was shown to be affected by the change of friction definition due to DSS model.

# CHAPTER 7 CONCLUSION

The motivation, relevant literature review and the results of the current study have been presented in previous chapters. The notable achievements of this thesis include:

- Development, fabrication and experimentation of a new microforming-specific friction test.
- Proposal for the lubrication mechanisms for solid, liquid and colloidal lubricants and its validation.
- Feasibility study on the use of surface textures for microforming friction control and proposal for the friction reduction mechanism from using surface textures.
- Development of FE contact simulation to represent the effect of strain gradient through DSS relation and its validation.

This chapter further elaborates on these achievements and relevant key findings.

## 7.1 Friction Test for Microforming

### *7.1.1 Microforming T-Shape test apparatus*

As presented in Chapter 4, the original T-Shape test which was designed for use in cold forging has been further developed for improved suitability for use in microforming. The test geometry was modified to enhance its friction sensitivity and the workpiece specimen was designed to have higher aspect ratio.

Aspect ratio (length/diameter) of 5 was used in the current experimental investigation. Aspect ratio equal to or higher than 5 is recommended to allow greater tolerance on the length of the specimen and thus it enables microforming T-Shape users to prepare the test workpiece from a stock reel without the need to precision machine the

workpiece to size. Aspect ratio equal to and higher than 10 is encouraged to enable plane strain simulation to be used to provide friction calibration curves instead of the costlier three-dimensional simulation. However, specimen with such high aspect ratio requires higher loading requirement for the microforming T-Shape test. In short, there is a trade-off between the capability of the press machine to be used and the desired amount of computation resource that can be allocated for the work.

The influence of die geometry and material mechanical properties was also investigated and it has been concluded than the die geometry tolerance of 1%, i.e. 10 micron for 1 mm workpiece, is suitable for the microforming T-Shape geometry. It was also found that the results of the microforming T-Shape test were not influenced by mechanical property variation up to 10%. Multi-material simulation has further established that even when the material mechanical property is changed threefold (between aluminium and copper), the resulting friction calibration curves remained similar. However, the limit to this material non-sensitivity was not yet established.

The overall modifications on the T-Shape test also simplify the handling of specimens, allow precise fabrication and characterization of the surface, as well as avoid the need to perform stroke correction to compensate for equipment deflection. These improvements further affirm the microforming T-Shape test apparatus as a suitable microforming friction test for both research and industry use.

### *7.1.2 Investigation of different materials and lubricants*

Copper, aluminium and silver were selected for the current investigation. Their selection was based on the projected demand of microformed products in the near future and that they have a common FCC crystal structures. For the multi-material

investigation, an empirical model to represent the friction calibration curves was presented to enable users to produce quantitative friction factor, $m$, without approximating it from the calibration curves. In the investigation, aluminium forming exhibited the highest friction and it can be explained by the likelihood of aluminium material to spontaneously form oxide layer which further transfers to the tool as galling.

Furthermore as presented in Chapter 4, three kinds of lubricants were used to further investigate the role of lubricants in microforming. The microforming T-Shape apparatus produced three distinct behaviours for the three kinds of lubricants used which can be attributed to factors such as particle size (of the solids) and the surface tension (of the liquids).

## 7.2 Surface Textures for Friction Control

Simulation was used to examine the usefulness of surface texturing as friction control in microforming. The simulation setup for investigating friction reduction mechanism of tribological surface texturing was presented in Chapter 5. The simulation technique was validated using pin on plate tribometer experiment as results showed that good agreement was achieved by both simulation and experiment.

The simulation results presented suggests there are two competing mechanisms when textures are introduced on the tool surface: reducing friction due to the reduced *actual* contact area, and increasing friction due to material entrapment by the textures.

This mechanism occurs in unlubricated contact without wear particles interaction at the interface which further explains the friction reduction in absence of wear particles

or in immersion lubrication and representative simulation setups were determined for each texture for future simulations.

The technique of the simulation has been validated through a pin on plate setup and the discrepancy between simulation and experimental results were attributed to the presence of defects on the textured pad which are not practical to fully simulate.

In the copper forming simulation, the simulation results suggest that the texturing of the tool in microforming can be tailored differently to various sections of the die, depending on the contact pressure experienced in each section of said die. Ultimately, the shape and alignment of the texture can be engineered with respect to the metal flow direction and the texture density can be created differently, i.e. low texture density for high pressure section and high texture density for low pressure section. Although this process is more straightforward for continuous process such as extrusion, it can also be used for other microforming processes.

Pore textures in general produce a certain friction reduction that is independent of the sliding direction and they are more suitable for forging processes where the direction of the metal flow may change during a forging process. Whereas directional textures such as ridges are more optimum when the sliding direction is parallel to the texture direction and hence alignment of these textures becomes significant for forming process with unidirectional sliding during the process such as extrusion.

The results acquired using this unit texture simulation can be used directly in microforming process simulation using process simulation software such as Deform 3D.

## 7.3 Depth-dependent Stress-strain Relation

The DSS relation was derived from the ISE model. ISE model from Abu Al-Rub [145] was selected for the current study as it encompasses both the threshold hardness value (which separates the hardness (or flow stress) due to dislocation and hardness from other source, e.g. material friction stress) as well as the non-linear coupling of dislocations which further results in growth of plastic zone.

The simulation work using the DSS relation showed good agreement with tribometer experiment without the addition of adhesion friction coefficient as it is commonly used in Green-based simulation [148].

The good agreement between simulation and experiment further supports the use of this modelling technique in simulating microforming processes in which strain gradient becomes significant. This DSS simulation method can be easily implemented into currently available FE analysis code for microforming of complex geometry. This further provides an alternative to the crystal plasticity or gradient-dependent plasticity simulation as these simulation methods are not suitable for use with complex geometry due to the very expensive computation time.

## 7.4 Future Work

This study has provided the microforming research and industry with the tool to better examine the friction behaviour in microforming, the microforming T-Shape test. During the multi-lubricant experiment, it was revealed that liquid lubricants in general are not suited for high pressure microforming process. This calls for a development work for a microforming friendly liquid lubricant as a future work.

This new microforming lubricant may be based on functional short chain polymers with functional head which will allow better surface wetting to the die surface. The short chain polymers will results in lower viscosity for better surface tension property for wetting while the functional head can be optimized for improving chemisorption to the surface.

Another avenue to look into is by using electric field to control the surface wetting of electrically charged lubricant, a technique which has been majorly used in automotive colour coating process, or even more advanced processes such as self-assembled monolayer (SAM) to create a lubricant coating.

In parallel, future work is also required to build further understanding in micro-meso metal deformation mechanism and provide a viable microforming process simulation algorithm.

The mechanism of deformation in micro-meso regime (1 μm to 1 mm) is influenced by the strain gradient plasticity severely and as such it may be inappropriate to consider the deformation using classical continuum plasticity and yet the use of nano-micro deformation model such as crystal plasticity is not suitable for severe deformation simulation to create complex geometry such is the case of microforming process.

The work on DSS incorporation has provided a stepping stone that it is possible to have a simulation approach which can predict this micro-meso deformation with reasonable numerical complexity. However, before the simulation technique can be fully implemented, more calibration is needed with different materials of varying deformation behaviour, e.g. different crystal structures, and with validation using

more complex deformation behaviour. The current study was focused on friction which is why the work is validated mainly for friction behaviour.

The simulation results on surface textures in Chapter 5 is presented to assess the feasibility of using surface textures for high pressure contact problems such as microforming, in which lubricant has reduced or negligible effect. This simulation can and needs to be improved further to predict possible microscopic texture imprint on the surface of the finished product, as well as crack initiation at the edges of the textures due to stress concentration.

This required more complete material and damage criteria of the specific materials to be provided for the simulation code but the outputs are of high interest. This also calls for more robust remeshing and solution mapping algorithm to be included in the simulation approach.

**References**

[1] M. Geiger, M. Kleiner, R. Eckstein, N. Tiesler, U. Engel, Microforming, CIRP Annals - Manufacturing Technology, 50 (2001) 445-462.

[2] U. Engel, A. Rosochowski, S. Geissdoerfer, L. Olejnik, Microforming and nanomaterials, in: F. Chinesta, E. Cueto (Eds.) Advances in Material Forming, Esaform 10 years on, Springer-Verlag, France, Paris, 2007, pp. 99-124.

[3] U. Engel, Tribology in Microforming, Wear, 260 (2006) 265-273.

[4] U. Engel, R. Eckstein, Microforming—from basic research to its realization, Journal of Materials Processing Technology, 125-126 (2002) 35-44.

[5] U. Engel, A. Messner, N. Tiesler, Cold Forging of Microparts - Effects of Miniaturization on Friction, in: J.L. Chenot (Ed.) 1st ESAFORM Conference on Materials Forming, Sophia Antipolis, 1998, pp. 77-80.

[6] N. Bay, A. Azushima, P. Groche, I. Ishibashi, M. Merklein, M. Morishita, T. Nakamura, S. Schmid, M. Yoshida, Environmentally benign tribo-systems for metal forming, CIRP Annals, 59 (2010) 760-780.

[7] T. Altan, S.-I. Oh, H.L. Gegel, Metal Forming: Fundamentals and Applications, American Society for Metals, Metals Park, 1983.

[8] T. Altan, G. Ngaile, G. Shen, Cold and Hot Forging: Fundamentals and Applications, ASM International, Ohio, 2005.

[9] T. Altan, Design and Manufacture of Dies and Molds, CIRP Annals - Manufacturing Technology, 36 (1987) 455-462.

[10] T. Altan, R.A. Miller, Design for Forming and other Near Net Shape Manufacturing Processes, CIRP Annals - Manufacturing Technology, 39 (1990) 609-620.

[11] T. Altan, V. Vazquez, Numerical Process Simulation for Tool and Process Design in Bulk Metal Forming, CIRP Annals - Manufacturing Technology, 45 (1996) 599-615.

[12] T. Altan, V. Vazquez, Status of process simulation using 2D and 3D finite element method 'What is practical today? What can we expect in the future?', Journal of Materials Processing Technology, 71 (1997) 49-63.

[13] M. Knoerr, J. Lee, T. Altan, Application of the 2D finite element method to simulation of various forming processes, Journal of Materials Processing Technology, 33 (1992) 31-55.

[14] T. Altan, M. Knoerr, Application of the 2D finite element method to simulation of cold-forging processes, Journal of Materials Processing Technology, 35 (1992) 275-302.

[15] T. Altan, B. Lilly, Y.C. Yen, Manufacturing of Dies and Molds, CIRP Annals - Manufacturing Technology, 50 (2001) 404-422.

[16] T. Altan, B.W. Lilly, J.P. Kruth, W. König, H.K. Tönshoff, C.A. van Luttervelt, A.B. Khairy, Advanced Techniques for Die and Mold Manufacturing, CIRP Annals - Manufacturing Technology, 42 (1993) 707-716.

[17] J. Jeswiet, M. Geiger, U. Engel, M. Kleiner, M. Schikorra, J. Duflou, R. Neugebauer, P. Bariani, S. Bruschi, Metal forming progress since 2000, CIRP Journal of Manufacturing Science and Technology, 1 (2008) 2-17.

[18] A.R. Razali, Y. Qin, A Review on Micro-manufacturing, Micro-forming and their Key Issues, Procedia Engineering, 53 (2013) 665-672.

[19] J. Ast, K. Durst, Nanoforming behaviour and microstructural evolution during nanoimprinting of ultrafine-grained and nanocrystalline metals, Materials Science and Engineering: A, 568 (2013) 68-75.

[20] Friction, in: J. Simpson, E. Weiner (Eds.) Oxford English Dictionary, Oxford University Press, Oxford, 1989.

[21] P.J.M. Janssen, T.H.d. Keijser, M.G.D. Geers, An experimental assessment of grain size effects in the uniaxial straining of thin Al sheet with a few grains across the thickness, Materials Science and Engineering A, 419 (2006) 238-248.

[22] W.D. Callister, D.G. Rethwisch, Materials Science and Engineering: An Introduction, Wiley, 2013.

[23] W.F. Smith, J. Hashemi, Foundations of materials science and engineering, McGraw-Hill Publishing, 2006.

[24] N. Hansen, Hall–Petch relation and boundary strengthening, Scripta materialia, 51 (2004) 801-806.

[25] J. Schiotz, F.D. Di Tolla, K.W. Jacobsen, Softening of nanocrystalline metals at very small grain sizes, Nature, 391 (1998) 561-563.

[26] R. Raj, M.F. Ashby, On grain boundary sliding and diffusional creep, MT, 2 (1971) 1113-1127.

[27] P.F. Bariani, T. Dal Negro, S. Bruschi, Testing and Modelling of Material Response to Deformation in Bulk Metal Forming, CIRP Annals - Manufacturing Technology, 53 (2004) 573-595.

[28] P. Bate, Modelling deformation microstructure with the crystal plasticity finite–element method, Philosophical Transactions of the Royal Society of London. Series A: Mathematical, Physical and Engineering Sciences, 357 (1999) 1589-1601.

[29] J. Cao, W. Zhuang, S. Wang, J. Lin, Development of a VGRAIN system for CPFE analysis in micro-forming applications, Int J Adv Manuf Technol, 47 (2010) 981-991.

[30] J.S. Stölken, A.G. Evans, A microbend test method for measuring the plasticity length scale, Acta Materialia, 46 (1998) 5109-5115.

[31] R. De Borst, J. Pamin, Some novel developments in finite element procedures for gradient-dependent plasticity, International Journal for Numerical Methods in Engineering, 39 (1996) 2477-2505.

[32] R. De Borst, H.-B. Mühlhaus, Gradient-dependent plasticity: Formulation and algorithmic aspects, International Journal for Numerical Methods in Engineering, 35 (1992) 521-539.

[33] C. Keller, E. Hug, Hall–Petch behaviour of Ni polycrystals with a few grains per thickness, Materials Letters, 62 (2008) 1718-1720.

[34] C. Keller, E. Hug, D. Chateigner, On the origin of the stress decrease for nickel polycrystals with few grains across the thickness, Materials Science and Engineering: A, 500 (2009) 207-215.

[35] S. Miyazaki, H. Fujita, H. Hiraoka, Effect of specimen size on the flow stress of rod specimens of polycrystalline Cu-Al alloy, Scripta Metallurgica, 13 (1979) 447-449.

[36] F. Vollertsen, H. Schulze-Niehoff, Z. Hu, State of the art in micro forming, International Journal of Machine Tools & Manufacture, 46 (2006) 1172-1179.

[37] F. Vollertsen, Categories of size effects, Production Engineering: Research and Development, 2 (2008) 377-383.

[38] J.G. Liu, M.W. Fu, W.L. Chan, A constitutive model for modeling of the deformation behavior in microforming with a consideration of grain boundary strengthening, Computational Materials Science, 55 (2012) 85-94.

[39] W.L. Chan, M.W. Fu, Experimental studies and numerical modeling of the specimen and grain size effects on the flow stress of sheet metal in microforming, Materials Science and Engineering: A, 528 (2011) 7674-7683.

[40] S.A. Parasız, B.L. Kinsey, N. Mahayatsanun, J. Cao, Effect of specimen size and grain size on deformation in microextrusion, Journal of Manufacturing Processes, 13 (2011) 153-159.

[41] C. Wang, C. Wang, B. Guo, D. Shan, G. Huang, Size effect on flow stress in uniaxial compression of pure nickel cylinders with a few grains across thickness, Materials Letters, 106 (2013) 294-296.

[42] B. Eichenheuller, E. Egerer, U. Engel, Microforming at elevated temperature - forming and material behaviour, Int J Adv Manuf Technol, 33 (2005) 119-124.

[43] U. Engel, E. Egerer, Basic research on cold and warm forging of microparts, Key Engineering Materials, 233-236 (2002) 449-456.

[44] E. Egerer, U. Engel, Process characterization and material flow in microforming at elevated temperatures, Journal of Manufacturing Processes, 5 (2004) 11-16.

[45] M. Geiger, U. Engel, M. Pfestorf, New Developments for the Qualification of Technical Surfaces in Forming Processes, CIRP Annals - Manufacturing Technology, 46 (1997) 171-174.

[46] S.W. Baek, S.I. Oh, S.H. Rhim, Lubrication for Micro Forming of Ultra Thin Metal Foil, CIRP Annals - Manufacturing Technology, 55 (2006) 295-298.

[47] Z. Hu, A. Schubnov, F. Vollertsen, Tribological behaviour of DLC-films and their application in micro deep drawing, Journal of Materials Processing Technology, 212 (2012) 647-652.

[48] C. Wang, B. Guo, D. Shan, X. Bai, Tribological behaviors of DLC film deposited on female die used in strip drawing, Journal of Materials Processing Technology, 213 (2013) 323-329.

[49] B. Guo, F. Gong, C. Wang, D. Shan, Flow stress and tribology size effects in scaled down cylinder compression, Transactions of nonferrous metals society of China, 19 (2009) s516-s520.

[50] W.L. Chan, M.W. Fu, Studies of the interactive effect of specimen and grain sizes on the plastic deformation behavior in microforming, Int J Adv Manuf Technol, 62 (2012) 989-1000.

[51] L. Dubar, C. Hubert, P. Christiansen, N. Bay, A. Dubois, Analysis of fluid lubrication mechanisms in metal forming at mesoscopic scale, CIRP Annals - Manufacturing Technology, 61 (2012) 271-274.

[52] K. Holmberg, P. Andersson, A. Erdemir, Global energy consumption due to friction in passenger cars, Tribology International, 47 (2012) 221-234.

[53] O. Singh, S.S. Bhavikatti, S. Chandra, P.K. Bharti, Introduction To Mechanical Engineering: Thermodynamics, Mechanics And Strength Of Material, New Age International, New Delhi, 2007.

[54] J. Beddoes, M.J. Bibby, Principles of Metal Manufacturing Processes, Arnold, London, 1999.

[55] E. Orowan, The calculation of roll pressure in hot and cold flat rolling, in: Institute of Mechanical Engineering, 1943, pp. 140.

[56] T. Wanheim, N. Bay, A.S. Peterson, A theoretically determined model for friction in metal forming processes, Wear, 28 (1974) 251-258.

[57] N. Bay, Friction stress and normal stress in bulk metal-forming processes, Journal of Mechanical Working Technology, 14 (1987) 203-223.

[58] X. Tan, Comparisons of friction models in bulk metal forming, Tribology International, 35 (2002) 385-393.

[59] Z. Mróz, S. Stupkiewicz, Constitutive model of adhesive and ploughing friction in metal-forming processes, International Journal of Mechanical Sciences, 40 (1998) 281-303.

[60] S. Kalpakjian, S.R. Schmid, Manufacturing Engineering and Technology, 5th ed., Pearson Prentice Hall, Upper Saddle River, 2006.

[61] F.P. Bowden, D. Tabor, The Friction and Lubrication of Solids, Oxford University Press, Oxford, 2001.

[62] W.R.D. Wilson, Friction and lubrication in bulk metal-forming processes, Journal of Applied Metalworking, 1 (1978) 7-19.

[63] U. Pettersson, Surfaces designed for high and low friction, Digital Comprehensive Summaries of Uppsala Dissertations from the Faculty of Technology, 63 1651-6214.

[64] C.G. Sørensen, J.I. Bech, J.L. Andreasen, N. Bay, U. Engel, T. Neudecker, A Basic Study of the Influence of Surface Topography on Mechanisms of Liquid Lubrication in Metal Forming, CIRP Annals - Manufacturing Technology, 48 (1999) 203-208.

[65] J. Bech, N. Bay, M. Eriksen, Entrapment and escape of liquid lubricant in metal forming, Wear, 232 (1999) 134-139.

[66] J. Bech, N. Bay, M. Eriksen, A Study of Mechanisms of Liquid Lubrication in Metal Forming, CIRP Annals - Manufacturing Technology, 47 (1998) 221-226.

[67] A. Amanov, R. Tsuboi, H. Oe, S. Sasaki, The influence of bulges produced by laser surface texturing on the sliding friction and wear behavior, Tribology International, 60 (2013) 216-223.

[68] S. Schreck, K.H. Zum Gahr, Laser-assisted structuring of ceramic and steel surfaces for improving tribological properties, Applied surface science, 247 (2005) 616-622.

[69] A. Borghi, E. Gualtieri, D. Marchetto, L. Moretti, S. Valeri, Tribological effects of surface texturing on nitriding steel for high-performance engine applications, Wear, 265 (2008) 1046-1051.

[70] E. Brinksmeier, O. Riemer, S. Twardy, Tribological behavior of micro structured surfaces for micro forming tools, International Journal of Machine Tools and Manufacture, 50 (2010) 425-430.

[71] R.S. Eriksen, M. Arentoft, J. Grønbæk, N. Bay, Manufacture of functional surfaces through combined application of tool manufacturing processes and Robot Assisted Polishing, CIRP Annals - Manufacturing Technology, 61 (2012) 563-566.

[72] K. Wagner, R. Völkl, U. Engel, Tool life enhancement in cold forging by locally optimized surfaces, Journal of Materials Processing Technology, 201 (2008) 2-8.

[73] M. Geiger, U. Popp, U. Engel, Excimer Laser Micro Texturing of Cold Forging Tool Surfaces - Influence on Tool Life, CIRP Annals - Manufacturing Technology, 51 (2002) 231-234.

[74] N.P. Suh, M. Mosleh, P.S. Howard, Control of friction, Wear, 175 (1994) 151-158.

[75] H. Tian, N. Saka, N.P. Suh, Boundary lubrication studies on undulated titanium surfaces, Tribology Transactions, 32 (1989) 289-296.

[76] A. Blatter, M. Maillat, S. Pimenov, G. Shafeev, A. Simakin, E. Loubnin, Lubricated sliding performance of laser-patterned sapphire, Wear, 232 (1999) 226-230.

[77] Y. Uehara, M. Wakuda, Y. Yamauchi, S. Kanzaki, S. Sakaguchi, Tribological properties of dimpled silicon nitride under oil lubrication, Journal of the European Ceramic Society, 24 (2004) 369-373.

[78] A. Kovalchenko, O. Ajayi, A. Erdemir, G. Fenske, I. Etsion, The effect of laser surface texturing on transitions in lubrication regimes during unidirectional sliding contact, Tribology International, 38 (2005) 219-225.

[79] X. Wang, K. Kato, K. Adachi, K. Aizawa, The effect of laser texturing of SiC surface on the critical load for the transition of water lubrication mode from hydrodynamic to mixed, Tribology International, 34 (2001) 703-711.

[80] W. Tang, Y. Zhou, H. Zhu, H. Yang, The effect of surface texturing on reducing the friction and wear of steel under lubricated sliding contact, Applied surface science, 273 (2013) 199-204.

[81] P. Suh, The delamination theory of wear, Wear, 25 (1973) 111-124.

[82] W. Koszela, P. Pawlus, L. Galda, The effect of oil pockets size and distribution on wear in lubricated sliding, Wear, 263 (2007) 1585-1592.

[83] M. Wakuda, Y. Yamauchi, S. Kanzaki, Y. Yasuda, Effect of surface texturing on friction reduction between ceramic and steel materials under lubricated sliding contact, Wear, 254 (2003) 356-363.

[84] D.Z. Segu, S.G. Choi, J.h. Choi, S.S. Kim, The effect of multi-scale laser textured surface on lubrication regime, Applied surface science, 270 (2013) 58-63.

[85] J. Li, D. Xiong, J. Dai, Z. Huang, R. Tyagi, Effect of surface laser texture on friction properties of nickel-based composite, Tribology International, 43 (2010) 1193-1199.

[86] U. Pettersson, S. Jacobson, Influence of surface texture on boundary lubricated sliding contacts, Tribology International, 36 (2003) 857-864.

[87] U. Pettersson, S. Jacobson, Textured surfaces for improved lubrication at high pressure and low sliding speed of roller/piston in hydraulic motors, Tribology International, 40 (2007) 355-359.

[88] P.L. Menezes, Influence of surface texture on coefficient of friction and transfer layer formation during sliding of pure magnesium pin on 080 M40 (EN8) steel plate, Wear, 261 (2006) 578-591.

[89] P.L. Menezes, Effect of surface roughness parameters and surface texture on friction and transfer layer formation in tin-steel tribo-system, Journal of Materials Processing Technology, 208 (2008) 372-382.

[90] P.L. Menezes, Influence of surface texture and roughness parameters on friction and transfer layer formation during sliding of aluminium pin on steel plate, Wear, 267 (2009) 1534-1549.

[91] P.L. Menezes, Studies on friction and formation of transfer layer when Al-4Mg alloy pins slid at various numbers of cycles on steel plates of different surface texture, Wear, 267 (2009) 525-534.

[92] J. Danckert, T. Wanheim, Analysis of the ring test method for the evaluation of frictional stresses in bulk metal forming processes, CIRP Annals-Manufacturing Technology, 37 (1988) 217-220.

[93] X. Tan, P. Martins, N. Bay, W. Zhang, Friction studies at different normal pressures with alternative ring-compression tests, Journal of Materials Processing Technology, 80 (1998) 292-297.

[94] T. Schrader, M. Shirgaokar, T. Altan, A critical evaluation of the double cup extrusion test for selection of cold forging lubricants, Journal of Materials Processing Technology, 189 (2007) 36-44.

[95] Y. Qin, Y. Ma, C. Harrison, A. Brockett, M. Zhou, J. Zhao, F. Law, A. Razali, R. Smith, J. Eguia, Development of a new machine system for the forming of micro-sheet-products, International Journal of Material Forming, 1 (2008) 475-478.

[96] G.E. Dieter, H.A. Kuhn, S.L. Semiatin, Handbook of workability and process design, ASM International, Materials Park, 2003.

[97] E. Ghassemali, M.-J. Tan, A.E.W. Jarfors, S.C.V. Lim, Optimization of axisymmetric open-die micro-forging/extrusion processes: An upper bound approach, International Journal of Mechanical Sciences, 71 (2013) 58-67.

[98] W.L. Chan, M.W. Fu, Meso-scaled progressive forming of bulk cylindrical and flanged parts using sheet metal, Materials & Design, 43 (2013) 249-257.

[99] M. Merklein, J.M. Allwood, B.A. Behrens, A. Brosius, H. Hagenah, K. Kuzman, K. Mori, A.E. Tekkaya, A. Weckenmann, Bulk forming of sheet metal, CIRP Annals - Manufacturing Technology, 61 (2012) 725-745.

[100] M. Merklein, J. Koch, T. Schneider, S. Opel, U. Vierzigmann, Manufacturing of complex functional components with variants by using a new metal forming process – sheet-bulk metal forming, International Journal of Material Forming, 3 (2010) 347-350.

[101] M. Merklein, J. Koch, S. Opel, T. Schneider, Fundamental investigations on the material flow at combined sheet and bulk metal forming processes, CIRP Annals - Manufacturing Technology, 60 (2011) 283-286.

[102] S. Petersen, P. Martins, N. Bay, Friction in bulk metal forming: a general friction model vs. the law of constant friction, Journal of Materials Processing Technology, 66 (1997) 186-194.

[103] A.T. Male, M.G. Cockroft, A Method for the determination of the coefficient of friction of metals under conditions of bulk plastic deformation, Journal Institute of Metals, 93 (1964) 38-46.

[104] A. Messner, U. Engel, R. Kals, F. Vollertsen, Size effect in the FE-simulation of micro-forming processes, Journal of Materials Processing Technology, 45 (1994) 371-376.

[105] S.I. Oh, Finite element analysis of metal forming processes with arbitrarily shaped dies, International Journal of Mechanical Sciences, 24 (1982) 479-493.

[106] Y.T. Im, O. Vardan, G. Shen, T. Altan, Investigation of Metal Flow in Non-Isothermal Forging Using Ring and Spike Tests, CIRP Annals - Manufacturing Technology, 37 (1988) 225-230.

[107] S. Isogawa, A. Kimura, Y. Tozawa, Proposal of an evaluating method on lubrication, CIRP Annals - Manufacturing Technology, 41 (1992) 263-266.

[108] W. Xu, K. Rao, Analysis of the deformation characteristics of spike-forging process through FE simulations and experiments, Journal of Materials Processing Technology, 70 (1997) 122-128.

[109] K. Kuzman, E. Pfeifer, N. Bay, J. Hunding, Control of material flow in a combined backward can-forward rod extrusion, Journal of Materials Processing Technology, 60 (1996) 141-147.

[110] A. Buschhausen, K. Weinmann, J.Y. Lee, T. Altan, Evaluation of lubrication and friction in cold forging using a double backward-extrusion process, Journal of Materials Processing Technology, 33 (1992) 95-108.

[111] X. Tan, N. Bay, W. Zhang, On parameters affecting metal flow and friction in the double cup extrusion test, Scandinavian Journal of Metallurgy, 27 (1998) 246-252.

[112] H. Sofuoglu, H. Gedikli, Determination of friction coefficient encountered in large deformation processes, Tribology International, 35 (2002) 27-34.

[113] E. Ghassemali, A.E.W. Jarfors, M.J. Tan, S.C.V. Lim, On the microstructure of micro-pins manufactured by a novel progressive microforming process, International Journal of Material Forming, (2011) 1-10.

[114] R. Ebrahimi, A. Najafizadeh, A new method for evaluation of friction in bulk metal forming, Journal of Materials Processing Technology, 152 (2004) 136-143.

[115] N. Krishnan, J. Cao, K. Dohda, Study of the Size Effects on Friction Conditions in Microextrusion---Part I: Microextrusion Experiments and Analysis, Journal of Manufacturing Science and Engineering, 129 (2007) 669-676.

[116] Q. Zhang, E. Felder, S. Bruschi, Evaluation of friction condition in cold forging by using T-shape compression test, Journal of Materials Processing Technology, 209 (2009) 5720-5729.

[117] Y.T. Im, J.S. Cheon, S.H. Kang, Determination of friction condition by geometrical measurement of backward extruded aluminum alloy specimen, Journal of Manufacturing Science and Engineering, 124 (2002) 409-415.

[118] G. Shen, A. Vedhanayagam, E. Kropp, T. Altan, A method for evaluating friction using a backward extrusion-type forging, Journal of Materials Processing Technology, 33 (1992) 109-123.

[119] F. Fereshteh-Saniee, H. Badnava, S.M. Pezeshki-Najafabadi, Application of T-shape friction test for AZ31 and AZ80 magnesium alloys at elevated temperatures, Materials & Design, 32 (2011) 3221-3230.

[120] M. Taureza, S. Castagne, Y. Aue-u-lan, Improving the sensitivity of T-Shape test to friction condition for the evaluation of friction behaviour in microforming, Key Engineering Materials, 447-448 (2010) 386-390.

[121] M. Taureza, S. Castagne, Y. Aue-u-lan, S.C.V. Lim, The influence of die geometry and workpiece mechanical properties in T-Shape friction test, Journal of Materials Processing Technology, 212 (2012) 2413-2423.

[122] L.M. Bernick, R.R. Hilsen, C.L. Wandrei, Development of a quantitative sheet galling test, Wear, 48 (1978) 323-346.

[123] K.G. Budinski, Incipient galling of metals, Wear, 74 (1981) 93-105.

[124] E. Schedin, Galling mechanisms in sheet forming operations, Wear, 179 (1994) 123-128.

[125] F. Gong, B. Guo, Effects of solid lubrication film on SKD11 in micro sheet forming, Surface and Coatings Technology, 232 (2013) 814-820.

[126] L. Peng, X. Lai, H.J. Lee, J.H. Song, J. Ni, Friction behavior modeling and analysis in micro/meso scale metal forming process, Materials & Design, 31 (2010) 1953-1961.

[127] M. Avrami, Kinetics of Phase Change. I General Theory, The Journal of Chemical Physics, 7 (1939) 1103-1112.

[128] M. Suh, Y. Chae, S. Kim, T. Hinoki, A. Kohyama, Effect of geometrical parameters in micro-grooved crosshatch pattern under lubricated sliding friction, Tribology International, 43 (2010) 1508-1517.

[129] N.P. Suh, An overview of the delamination theory of wear, Wear, 44 (1977) 1-16.

[130] M. Scaraggi, F. Mezzapesa, G. Carbone, A. Ancona, L. Tricarico, Friction Properties of Lubricated Laser-MicroTextured-Surfaces: An Experimental Study from Boundary- to Hydrodynamic-Lubrication, Tribology letters, 49 (2013) 117-125.

[131] X. Zhang, Y. Lu, X. Zhong, G. Yi, J. Jia, Adhesion and friction studies of Au nanoparticle-textured surfaces with colloidal tips, Surface and Interface Analysis, 44 (2012) 126-132.

[132] Z. Wu, J. Deng, Y. Xing, H. Cheng, J. Zhao, Effect of surface texturing on friction properties of WC/Co cemented carbide, Materials & Design, 41 (2012) 142-149.

[133] D.Z. Segu, J.-H. Kim, S.G. Choi, Y.-S. Jung, S.-S. Kim, Application of Taguchi techniques to study friction and wear properties of MoS2 coatings deposited on laser textured surface, Surface and Coatings Technology, 232 (2013) 504-514.

[134] A. Amanov, I.S. Cho, Y.S. Pyoun, C.S. Lee, I.G. Park, Micro-dimpled surface by ultrasonic nanocrystal surface modification and its tribological effects, Wear, 286–287 (2012) 136-144.

[135] D. Raabe, M. Sachtleber, Z. Zhao, F. Roters, S. Zaefferer, Micromechanical and macromechanical effects in grain scale polycrystal plasticity experimentation and simulation, Acta Materialia, 49 (2001) 3433-3441.

[136] X. Song, S.Y. Zhang, D. Dini, A.M. Korsunsky, Finite element modelling and diffraction measurement of elastic strains during tensile deformation of HCP polycrystals, Computational Materials Science, 44 (2008) 131-137.

[137] X. Song, F. Hofmann, A.M. Korsunsky, Dislocation-based plasticity model and micro-beam Laue diffraction analysis of polycrystalline Ni foil: A forward prediction, Philosophical Magazine, 90 (2010) 3999-4011.

[138] W.D. Nix, H. Gao, Indentation size effects in crystalline materials: a law for strain gradient plasticity, Journal of the Mechanics and Physics of Solids, 46 (1998) 411-425.

[139] M. Taureza, S. Castagne, S.C.V. Lim, Application of indentation size effect in finite element analysis for friction simulation, Key Engineering Materials, 535 (2013) 227-230.

[140] J.G. Swadener, E.P. George, G.M. Pharr, The correlation of the indentation size effect measured with indenters of various shapes, Journal of the Mechanics and Physics of Solids, 50 (2002) 681-694.

[141] N. Tymiak, D. Kramer, D. Bahr, T. Wyrobek, W. Gerberich, Plastic strain and strain gradients at very small indentation depths, Acta Materialia, 49 (2001) 1021-1034.

[142] D. Chicot, Hardness length-scale factor to model nano-and micro-indentation size effects, Materials Science and Engineering: A, 499 (2009) 454-461.

[143] G. Feng, W.D. Nix, Indentation size effect in MgO, Scripta materialia, 51 (2004) 599-603.

[144] X. Qiu, Y. Huang, W.D. Nix, K.C. Hwang, H. Gao, Effect of intrinsic lattice resistance in strain gradient plasticity, Acta Materialia, 49 (2001) 3949-3958.

[145] R.K. Abu Al-Rub, Prediction of micro and nanoindentation size effect from conical or pyramidal indentation, Mechanics of Materials, 39 (2007) 787-802.

[146] F. Bowden, D. Tabor, The area of contact between stationary and between moving surfaces, Proceedings of the Royal Society of London. Series A, Mathematical and Physical Sciences, 169 (1939) 391-413.

[147] A.P. Green, Friction between Unlubricated Metals: A Theoretical Analysis of the Junction Model, Proceedings of the Royal Society of London. Series A. Mathematical and Physical Sciences, 228 (1955) 191-204.

[148] D. Mulvihill, M. Kartal, D. Nowell, D. Hills, An elastic–plastic asperity interaction model for sliding friction, Tribology International, 44 (2011) 1679-1694.

[149] F.-K. Chen, J.-W. Tsai, A study of size effect in micro-forming with micro-hardness tests, Journal of Materials Processing Technology, 177 (2006) 146-149.

[150] D. Tabor, Indentation hardness: fifty years on a personal view, Philosophical Magazine A, 74 (1996) 1207-1212.

[151] S. Stupkiewicz, Micromechanics of contact and interphase layers, Springer, 2007.

[152] M.F. Ashby, J. Abulawi, H.S. Kong, Temperature Maps for Frictional Heating in Dry Sliding, Tribology Transactions, 34 (1991) 577-587.

[153] J.J. Park, N. Rebelo, S. Kobayashi, A new approach to preform design in metal forming with the finite element method, International Journal of Machine Tool Design and Research, 23 (1983) 71-79.

[154] S.M. Hwang, S. Kobayashi, Preform design in plane-strain rolling by the finite-element method, International Journal of Machine Tool Design and Research, 24 (1984) 253-266.

[155] T.B. Stoughton, A general forming limit criterion for sheet metal forming, International Journal of Mechanical Sciences, 42 (2000) 1-27.

[156] N. Ogawa, M. Shiomi, K. Osakada, Forming limit of magnesium alloy at elevated temperatures for precision forging, International Journal of Machine Tools and Manufacture, 42 (2002) 607-614.

[157] K.P. Li, W.P. Carden, R.H. Wagoner, Simulation of springback, International Journal of Mechanical Sciences, 44 (2002) 103-122.

[158] F. Yoshida, T. Uemori, A model of large-strain cyclic plasticity and its application to springback simulation, International Journal of Mechanical Sciences, 45 (2003) 1687-1702.

[159] W. Gan, R.H. Wagoner, Die design method for sheet springback, International Journal of Mechanical Sciences, 46 (2004) 1097-1113.

[160] A. Makinouchi, Sheet metal forming simulation in industry, Journal of Materials Processing Technology, 60 (1996) 19-26.

[161] S.Y. Kim, Y.T. Im, Three-dimensional finite element analysis of non-isothermal shape rolling, Journal of Materials Processing Technology, 127 (2002) 57-63.

## Appendix A: List of Publications

### *Journal Papers*

M. Taureza, S. Castagne, Y. Aue-u-lan, S.C.V. Lim, The influence of die geometry and workpiece mechanical properties in T-Shape friction test, Journal of Materials Processing Technology, 212 (2012) 2413-2423.

M. Taureza, X. Song, S. Castagne, On the influence of workpiece material on friction in microforming and lubricant effectiveness, Journal of Materials Processing Technology, 214 (2014) 998-1007.

M. Taureza, X. Song, S. Castagne, Depth-dependent stress–strain relation for friction prediction, International Journal of Mechanical Sciences. *In press.*

### *Conference Papers*

M. Taureza, S. Castagne, Y. Aue-u-lan, Improving the sensitivity of T-Shape test to friction condition for the evaluation of friction behaviour in microforming, Key Engineering Materials, 447-448 (2010) 386-390.

M. Taureza, S. Castagne, S.C.V. Lim, Influence of apparent contact pressures and groove parameters in contact simulation with tribological surface textures, in: The 4th International Conference on Advanced Manufacturing (ICAM 2012), Taiwan, 2012.

M. Taureza, S. Castagne, S.C.V. Lim, Application of indentation size effect in finite element analysis for friction simulation, Key Engineering Materials, 535 (2013) 227-230.

S. Castagne, M. Taureza, X. Song, Surface textures and friction control in microforming, in: The 6th International Conference on Tribology in Manufacturing Processes & Joining by Plastic Deformation (ICTMP 2014), Germany, 2014.

## Appendix B: Stress-strain Curve Correction

The upsetting experiment to obtain the stress strain relationship of the workpiece was performed in accordance with the procedure set by the Singapore Institute of Manufacturing Technology (SIMTech). The raw process load stroke curve is presented in Figure 100.

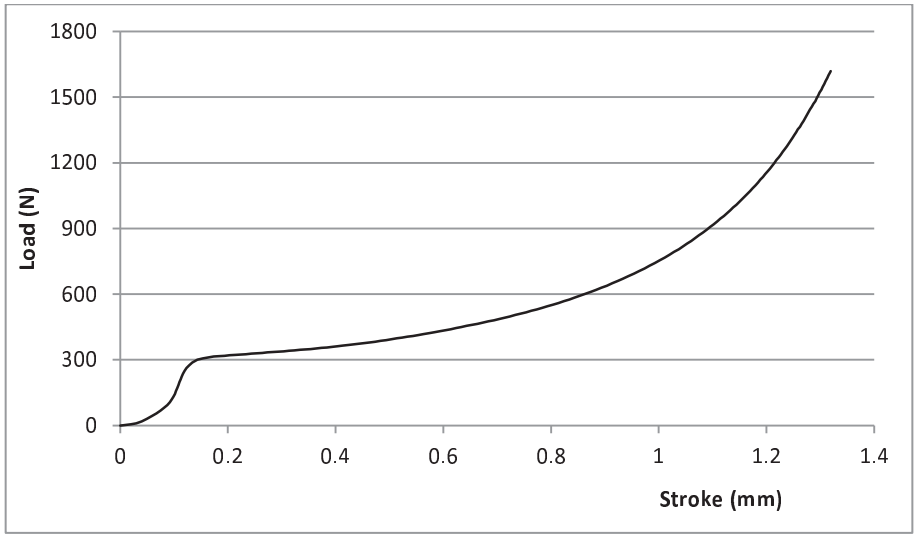


Figure 100: Raw load vs stroke curve from upsetting

Upsetting experiment was conducted using cylindrical specimen with 1±0.01 mm diameter and 1.5±0.01 mm height. Prior to the upsetting experiment, the exact initial diameter and height of the specimen was measured, and subsequently the initial contact area of the specimen was calculated. The machine stroke should allow 60-70% reduction from the initial height. In order to compensate elastic deflection of the tooling and specimen, the machine stroke in this case was set to 1.3 mm (>80% of the initial height).

Upsetting specimen was placed upright on the flat die, and thin Teflon sheets are placed at the top and bottom of the specimen to avoid direct contact between tooling

and specimen. The zero-stroke in the upsetting was determined by lowering the punch until load reading reaches a threshold value (few tens of newton). Upsetting samples are usually designed to have wax pocket at both ends to contain wax and reduce friction between the sample and the tooling. However, because of size constraint, the upsetting samples could not be made with wax pocket. With friction minimized, the influence of friction to the process load may be assumed to be negligible. After the upsetting experiment, the final height of the specimen was measured.

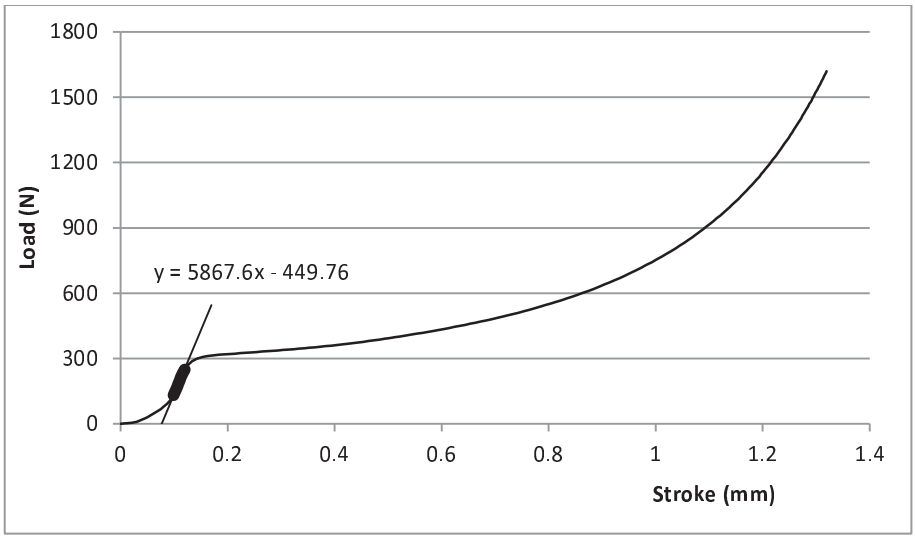


Figure 101: Raw data with tangent line

The load-stroke curve was compared with the load-stroke curve from the FE simulation. It was found that the initial non-linear rise of load (from the experiment) was not observed in the FE simulation of the upsetting process. Instead, they may be caused by the deformation of the Teflon sheet, and/or the flattening of the Teflon sheet to make the tight fit between the tooling and the specimen, and the zero-stroke is not the same with the zero-stroke from the FE simulation. Hence, a line tangent to the first linear load reading was drawn to illustrate the real load v stroke reading had the Teflon sheet not been present. Figure 101 shows the tangent line, and how the

intersection between the tangent line and the stroke axis was set to be the real zero-stroke.

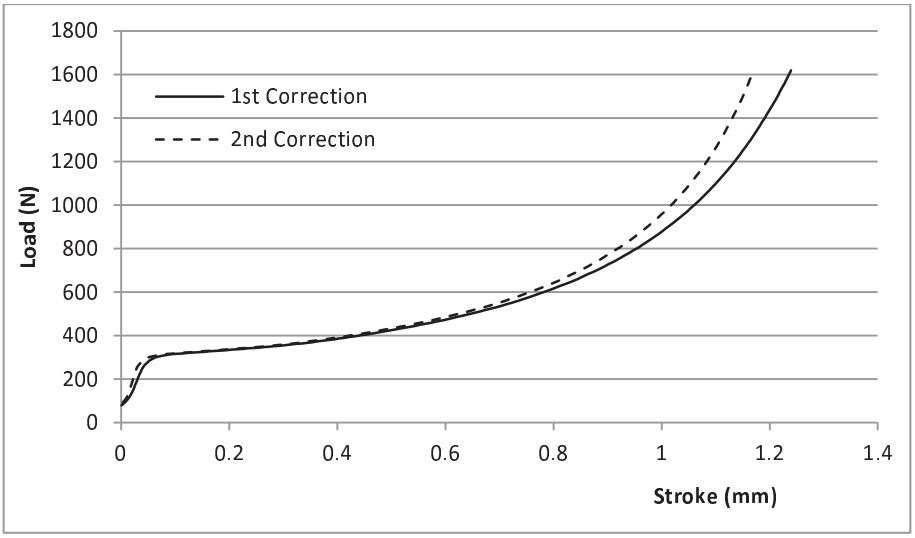


Figure 102: Load vs stroke curves after corrections

After obtaining the zero-stroke, all the points from the raw data was shifted to the left by the value of the tangent line intersect with stroke axis, i.e. intersect at 0.077 mm means that all data points should be shifted to the left by 0.077 mm (1$^{st}$ correction step as presented in Figure 102). In addition, even though the machine stroke (after zero-stroke correction) was 1.223 mm, the measurements of initial and final height reveals that the plastic stroke was only 1.17 mm (initial height 1.54 mm, final height 0.37 mm). The remaining was attributed largely to the elastic deflection of the equipment, and a smaller portion to the elastic deflection of the workpiece. Figure 102 shows the load-stroke curves after zero-stroke correction and elastic deflection correction (2$^{nd}$ correction step in Figure 102).

The constant $\alpha_{EL}$ was introduced to account for this elastic deflection (Equation B1):

$$\alpha_{EL} = \frac{Stroke_{machine} - Stroke_{measured}}{Load_{max}} \quad \text{B1}$$

The load vs stroke data points at every time, *t*, is further corrected using Equation B2:

$$Stroke_{real,t} = Stroke_{machine,t} - \alpha_{EL} * (Load_t) \quad \text{B2}$$

Lastly, the height (at every time, *t*) was calculated from the real stroke. Subsequently using Equations B3, B4, and the initial area of the tested specimen, $A_0$, the strain and stress at every data point can be calculated:

$$\varepsilon = \ln(\frac{H_0}{H_i}) \quad \text{B3}$$

$$\sigma = \frac{Load}{A_0}\exp(-\varepsilon) \quad \text{B4}$$

The stress-strain curve was produced as shown in Figure 103. The softening and hardening behaviour is more common for steels and is less so for copper. However, a previous investigation of mechanical properties of copper for microforming size at SIMTech revealed similar softening and hardening behaviour. This stress-strain curve was then used in the simulation of the

T-Shape test in Section 4.2 to 4.4. In subsequent section in Chapter 4 and elsewhere in this report, the material properties used were different as the materials for testing did not come from the same batch of material.

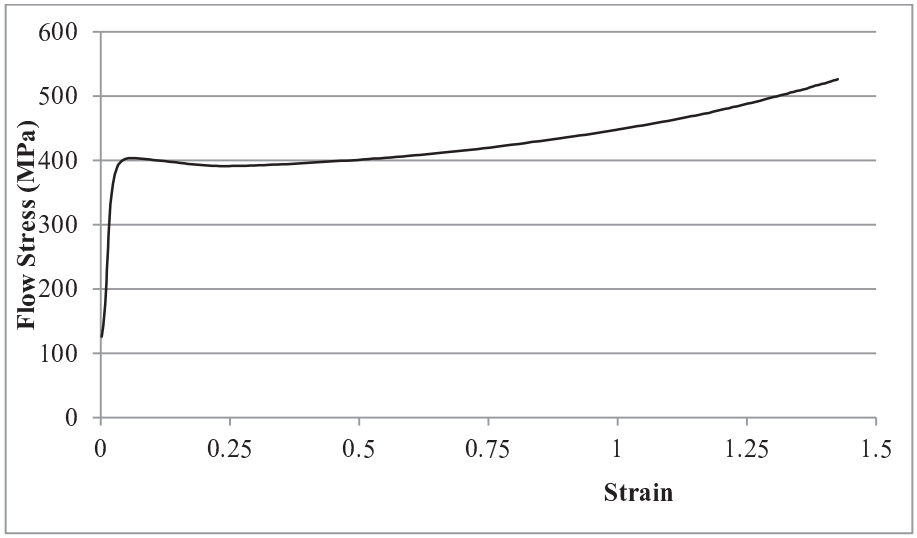


Figure 103: Stress v strain curve

## Appendix C: Depth-dependent Stress-strain Relation

The current investigation proposes a depth-dependent stress-strain relation to account for strain gradient effect during contact between a softer copper plate and a harder heat-treated tool steel material. Whereas the experiment is relatively straightforward, the simulation needs to be carefully approached in order to provide realistic results.

In the experiment, the pressure imposed between the bodies is limited only up to 200 MPa. This pressure is much lower than the yield stress of tool steel and therefore the tool steel was modelled as rigid body.

For the copper material, the ISE results of Abu Al-Rub [145] are used in the study (reinterpreted as Figure 104). The use of this DSS relation coefficient is further explained in this Appendix C.

The bulk copper material is assigned with a generic copper stress-strain relation as shown in Figure 22. However, for the region very close to the surface (a few microns deep), the deformation response is greatly influenced by the strain gradient effect.

The assignment of the material properties in the simulation is done through a so-called *pseudo-temperature* variable. The experiment itself is isothermal at room temperature with no heat given, produced or extracted from the setup. However in most simulation code, it is possible to easily create temperature dependent material property and therefore the temperature variable is used for simplicity rather than creating a new user variable.

The simulation consists of two distinct phases or steps. The first step is a purely thermal simulation while the second step is a purely mechanical simulation. In the

first step, the temperature at the surface of the copper domain was set as 0 ºC and farthest end simulated (25 µm) is assigned as 250 ºC using boundary conditions. The heat conduction within the copper domain can then be set to any positive value. The thermal simulation was then performed until a linear temperature gradient across the thickness is reached. By the end of the first simulation step, the assigned temperature is exactly 10 times the depth from the surface.

In the second step, the simulation is purely mechanical and there is no heat conduction within or between domains.

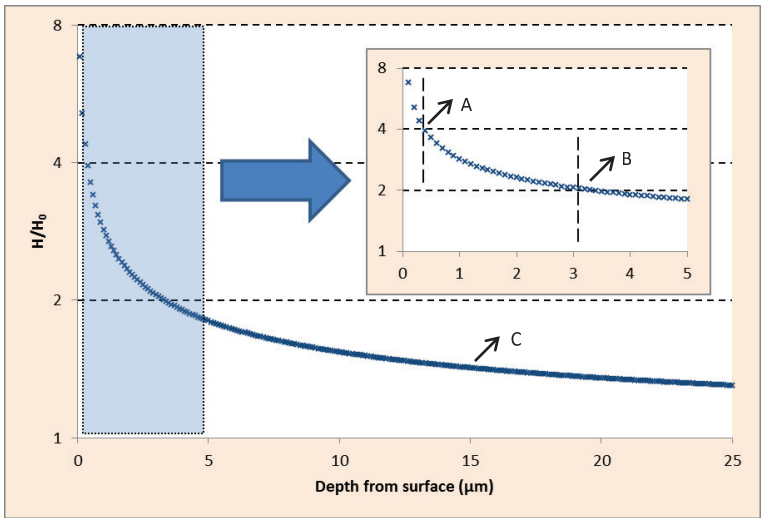


Figure 104: DSS relation coefficient (2)

In this appendix, the calculation for stress-strain relation at 0.4, 3.1 and 15 µm is given. For region 0.4 µm from the surface, the DSS relation coefficient is given as 4.0 (marked as "A" in Figure 104) and the assigned temperature is 4 ºC. Therefore, the material property at 4 ºC is assigned 4 times the value of the bulk as presented in Figure 105.

Using similar approach, the material property at 31 ºC and 150 ºC is assigned 2 and 1.5 times the value of the bulk.

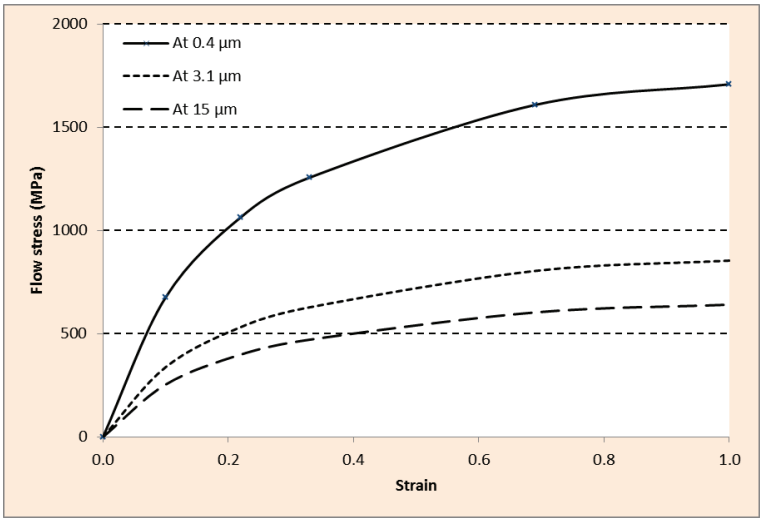


Figure 105: Flow stress at various depths